4

RESULTS

4.1 ACQUISITION OF HIGH RESOLUTION IMAGES

To generate a high-fidelity 3D+t atlas of early mouse heart development, we imaged 52 embryos using a confocal microscopy (see section 3.3). As we aim to elaborate a highly detailed geometrical description, we have opted for processing fixed and cleared embryos (section 3.2, subsection 3.2.4), thus minimizing light-scattering effects and maximizing resolution.

The acquired collection stand for nominal ages from approximately E7.75 to E8.5, representing cardiac developmental stages ranging from the early CC until heart looping. This period of development longs for 18 hours. With this, we estimate the average temporal density to be of 1 specimen every 20 minutes.

The imaged embryos carried *Mesp1*^{Cre} and *R26R*^{mTmG} and *R26R*^{Tomato} alleles, so that all the embryonic mesoderm was labelled with membrane green fluorescent protein (mGFP) and cytoplasmic Tomato protein, while the rest of the tissues were labelled only with membrane Tomato variant. The Figure 4.1 shows an optical section of a specimen, illustrating the different staining that the transgenic line induces in each tissue. In addition, we have also labeled cell nuclei with DAPI.

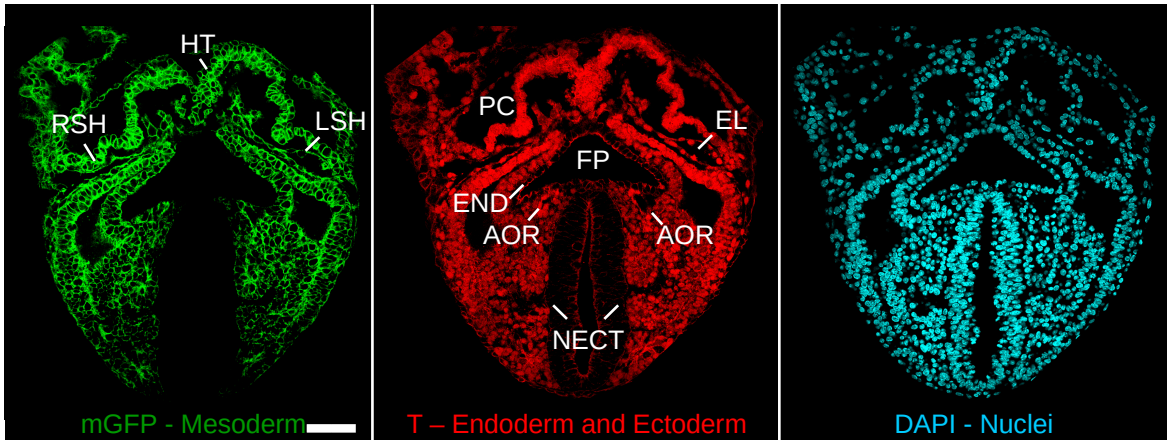

Figure 4.1 | **Transgenic line staining the tissues of interest.** Optical sections showing the different labels induced by the transgenic line (left and center). Right shows the additional DAPI staining. HT, heart tube; RSH, right sinus horn; LSH, left sinus horn; PC, pericardial cavity; EL, endocardial lumen; FP, foregut pocket; END, endoderm; AOR, aorta; NECT, Neuroectoderm. Scale bar 100μm.

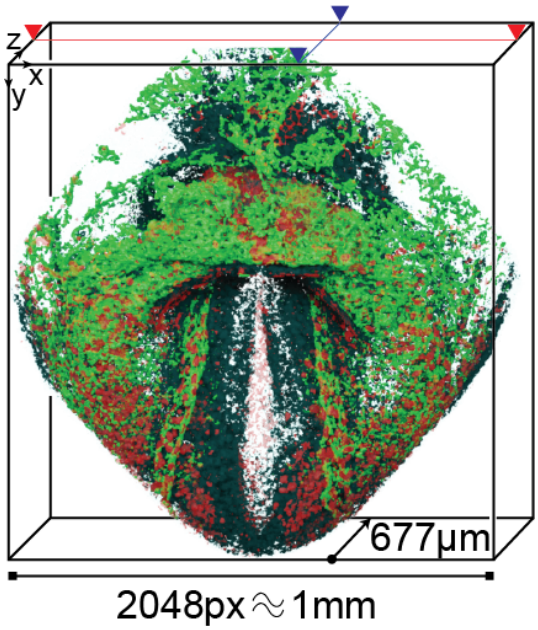

Figure 4.2 | **Raw image reconstruction.** Confocal raw image reconstruction showing the dimensions of the acquired volumes. Mesodermal tissues show the cytoplasm in red and cell membranes in green; the rest of the tissues show membranes in red. Cell nuclei appear in cyan. Red arrowheads refer to an optical section, as shown in Figure 4.1. Blue arrowheads refer to an orthogonal projection, as shown in Figure 4.3.

We have optimized the embryo preparation steps and clearing protocol in order to maximize resolution and penetration in confocal microscopy (see section 3.2). We have been able to complete whole embryo and have the specimens ready for imaging 3 days after the dissection. This time efficiency resulted in highly transparent embryos, with very well conserved fluorescence properties. In addition, we have also optimized the mounting method over the cover slip in order to reach the necessary depth to image further down the dorsal aorta. We have been able to image up to a depth of $677\mu m$ when necessary (see Figure 4.2). In most cases, the field of view of the lens was enough to cover the extension of the specimens (approximately $1mm^2$). In cases where the size of the embryo could not be covered by a single view, multi-acquisition and stitching of 2x2 or 4x4 windows was performed.

We have used a x,y-pixel size varying from $0.38\mu m$ to $0.49\mu m$. The z-step varied from $0.49\mu m$ to $2.0\mu m$. The varying ranges in resolution were adapted for optimization of acquisition time and minimization of photobleaching with the larger specimens. The relatively large range in the z-step did not introduce loss of accuracy in the segmentation at the tissue level, because the segmented tissue layers are approximately $20\mu m$ thick Figure 4.3 shows different optical sections at three different depths. It can be seen that the resolution of these images capture details at subcellular scale, which allows appreciating tissue morphology at great detail. In addition, it can be seen that the same level of detail prevails throughout the z-axis. This guarantees that tissue structure at deeper planes can also be properly resolved. On the other hand, Figure 4.3b shows an orthogonal projection of the z-stack. It can be seen that the high lateral resolution allows appreciating fine cellular and nuclear details, almost at the same level as the *xy*-plane optical sections.

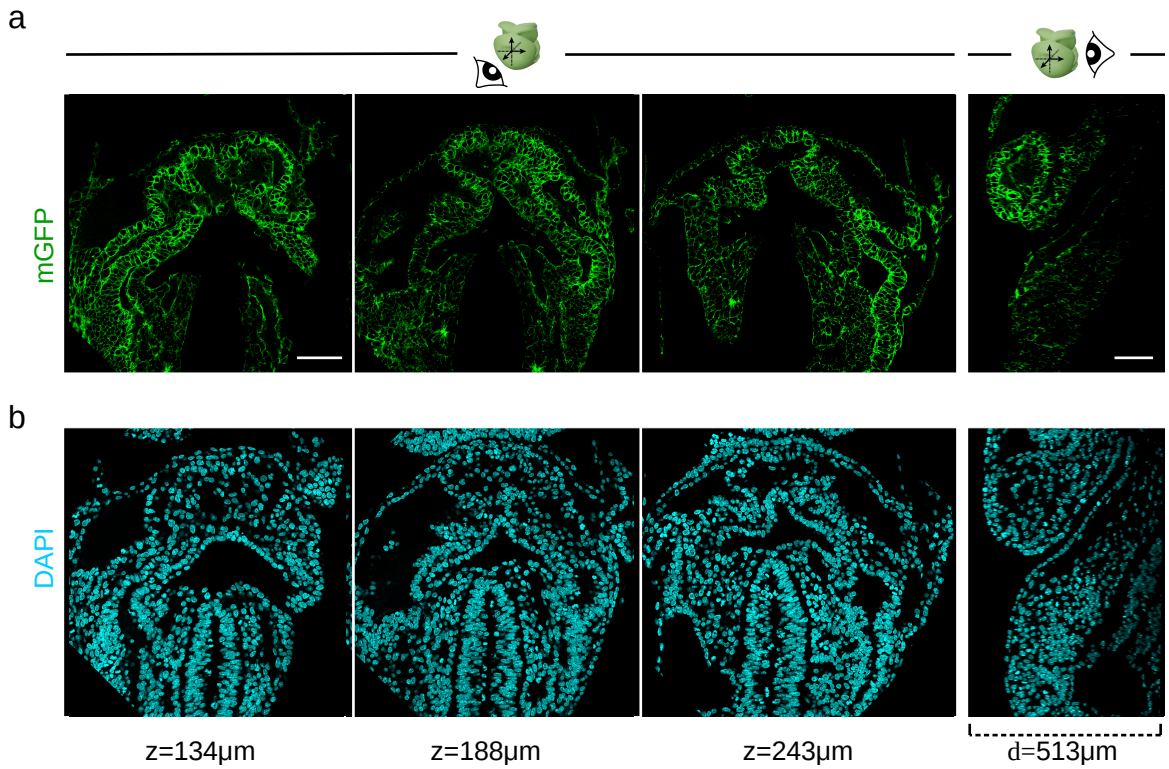

Figure 4.3 | **Embryo clarification and mounting system allows high resolution and large penetration depth. a**, Optical sections at different penetration depths. **b**, Orthogonal projection, showing a sagittal optical section. Scale bars 100μm.

4.2 SEGMENTATION

The region of interest in the embryo is highlighted in Figure 4.4a, where we show an optical section at the level of the inflow tract (IFT). The extension of this field covers the whole anterior-posterior and lateral extension of the ACC. On the other hand, Figure 4.4b shows a lateral optical cut at the level of one of the aortae. It can be seen that the region of interest extends beyond the foregut pocket (FP) and the AOR.

We have segmented the tissues forming the pericardial cavity (PC). We have done so by drawing a line of approximately 10μm thickness, that runs through the middle of the tissues. Then, we segmented the foregut endoderm (FGE) (see subsection 3.6.4). Lastly, we have segmented the incipient circulatory system (CS). For the latter, we have considered it as two different instances: the endocardial lumen (EL) and the aortic lumen (AOL). These structures have been segmented by filling the gap between the ECs forming their respective lumens (see subsection 3.6.2).

When segmenting the whole mesoderm (MES) of the forming anterior celomic cavity (ACC) (Figure 4.4c and Figure 4.4d), we started by dividing the lateral plate mesoderm (LPM) in its two layers: splanchnic mesoderm (SPL) and somatic mesoderm (SOM). To do so, we have used the images that labels the endoderm (END) and ectoderm (ECT), and re-labeled the portion of the segmented MES using contact/non-contact and

morphological criteria.

First, have identified the SPL domain by delineating the portion of the MES that is in contact with the END. Within this domain, we have also distinguished the differentiated myocardium (MYO) from the rest of the SPL (see Figure 4.4c bottom and Figure 4.4d bottom). We have done so by defining the portion of the SPL that is detached from the END and encases, or overlies, endocardial cells (ECs). Second, we identified the SOM by delineating the portion of the MES that is in contact with the ECT. Third, we have segmented the head paraxial mesoderm (HPM). This domain of the ACC is located in the dorsal side and is extended along the anterior-posterior axis. The HPM fuses the SPL and SOM. We have identified the HPM as the domain of the lateral plate mesoderm that is in contact with the paraxial mesoderm (PM) [125], located between the FGE and the ECT. The segmentation of the AOL and the EL is based on the detection of the lumen formed by the ECs. Regarding the AOL, we have not been able to cover its whole extension, as this would require a much larger field of view and penetration depth. Regarding the FGE, we have limited the segmentation on the endoderm (see Figure 4.4 top) by establishing a systematic approach for the whole collection (see subsection 3.6.4).

These segmentations, that label in every single slice the tissues and structures of interest, form what is known as segmentation images (SIs).

4.3 THREE-DIMENSIONAL REPRESENTATION OF THE DEVELOPING HEART

The aforementioned segmentation images (SIs) (see section 4.2) were then used for elaborating a 3D reconstruction of the tissues. These are based on extruding every pixel of the SI along its z-step size (i.e.: voxel), thus creating a voxel-grid. Prior to this, the SIs are filtered in order to smooth out sharp corners/details or to remove noisy voxels. In addition, a dilation filter is applied, which expands the 3D voxel-grid isotropically in every direction by a certain distance. The latter acts as a compensation for eroding effects that take place in subsequent steps of the processing pipeline. Further methodological details of this are included in section 3.7.

The three-dimensional aspect of the voxel-grid of all the tissues and structures segmented can be seen in Figure 4.5.

Although this representation is suitable for visualization purposes, is heavy, and not appropriate for the subsequent computational steps. We have therefore represented these structures by defining their outer surface, using a limited set of vertices, that form a network of interconnected triangles. This, so called *discrete surface*, or *mesh*, is a sort of representation suitable for computer graphics purposes (see Figure 1.4.1).

Thus, we have generated (see section 3.7) a mesh for the outer surface of each tissue/structure, for the 52 specimens of the collection. We have limited to 10.000 the

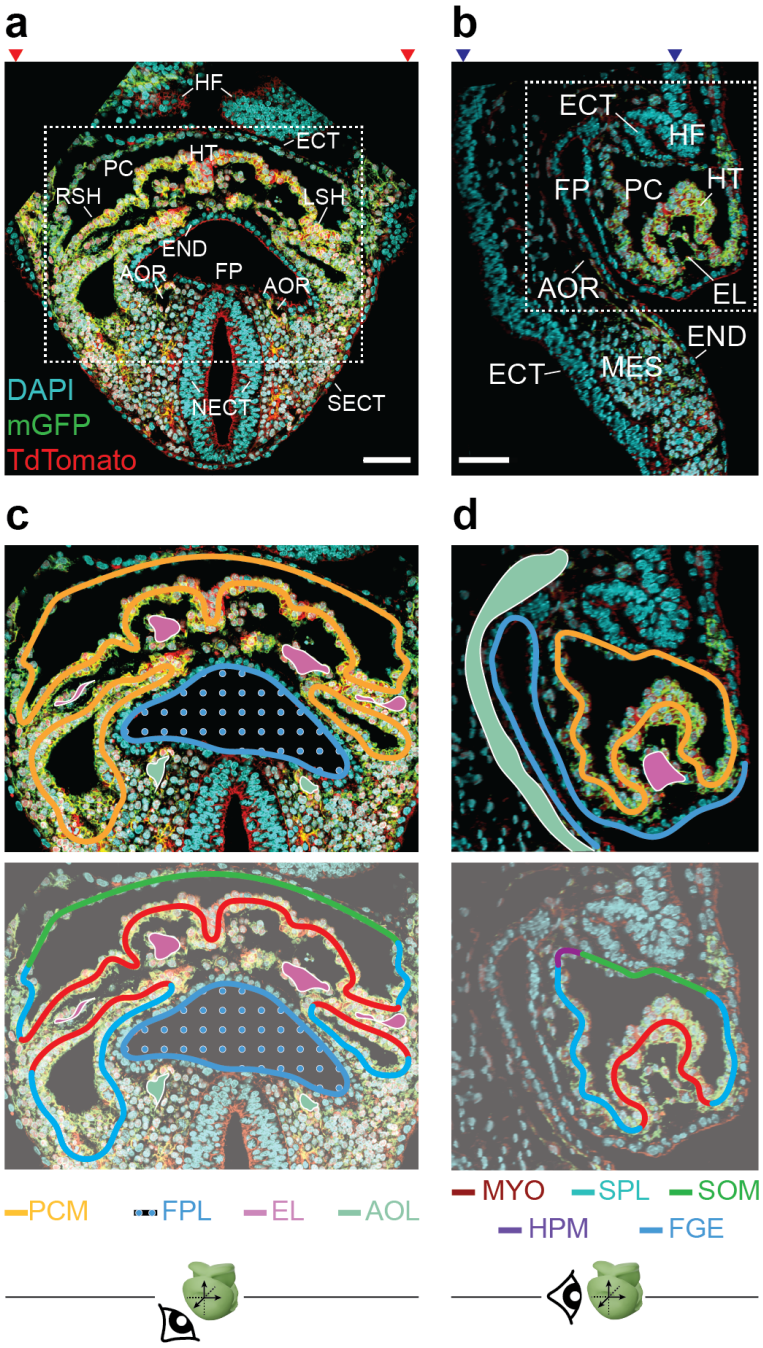

Figure 4.4 | **Segmentation of tissues and structures of interest. a**, Frontal optical section at the level of the inflow tract (IFT). Dotted-line box highlights the cardiac region. Red arrows indicate the direction of the optical cut, as represented in Figure 4.2.**b** Sagittal optical section at the level of one of the aortae. Blue arrows indicate the direction of the optical cut, as represented in Figure 4.2. **c**, (Top) The orange line shows the segmented mesoderm of the anterior celomic cavity, including the differentiating MYO. FGE is represented in blue. The FPL is represented using a blue-dot grid. EL is shown in pink, and AOL is shown in green. (Bottom) The same optical section showing the subtypes of mesoderm of the PC. MYO is in red, SPL is in blue, SOM is in green. **d**, (Top) Sames as **c** from a lateral view. (Bottom) Sames as **c** from a lateral view. Head paraxial mesoderm is in purple. HF, head folds. Scale bars $100\mu m$.

number of triangles used to define each surface. This amount provides enough precision for the right definition of the shapes and also minimizes their size. We have also made sure, or corrected otherwise, that these are closed surfaces and of genus-0 type, i.e.: spherical topology. The latter is important because, as will be shown in section 4.7, this is a mandatory topological feature needed for subsequent processing steps. Figure 4.6 shows the same structures shown in Figure 4.5 but represented as meshes.

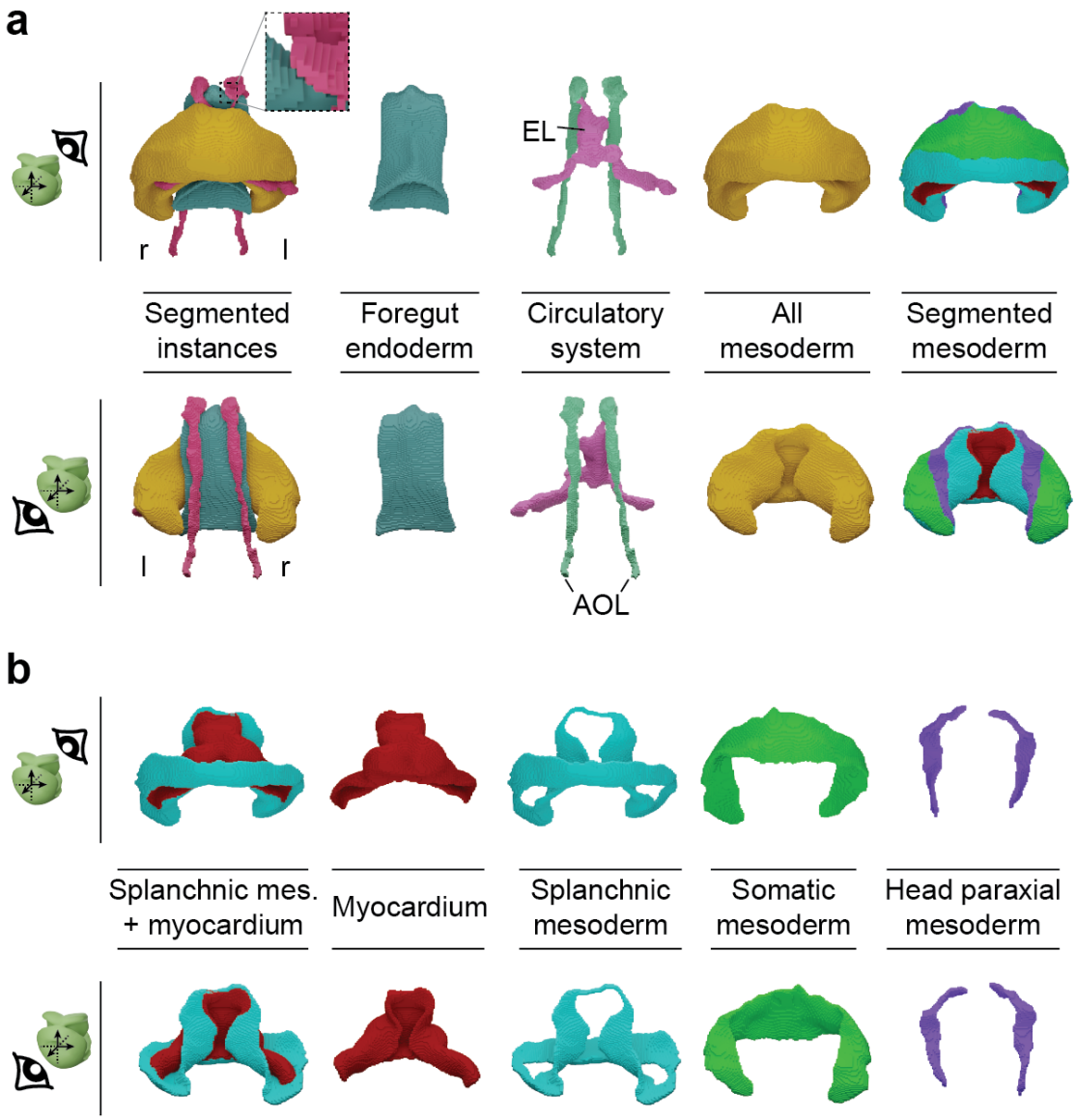

Figure 4.5 | **Voxel-grid representation of the tissues and structures of interest. a**, First column shows all the segmented instances. The dotted box shows a detail of how the voxel-grid is built. Second, third and fourth column show the segmented instances broke down in different ones. Last column shows the tissues forming the PC split in different tissues. Top row shows a ventral view, bottom row shows a dorsal view. **b**, Sub-types of the segmented mesoderm forming the ACC from ventral (top) and dorsal (bottom) view. EL, endocardial lumen; AOL, aortic lumen; l, left; r, right.

As can be noted in Figure 4.6b, the SPL shapes are not of genus-0, but genus-1 (toroid topology). We have developed an approach to convert these shapes to genus 0 (see section 3.19). The same thing happens with the morphology of the HT at stages from E8.0, as they fold and fuse dorsally, generating a toroid topology (genus 1).

4.4 OBSERVATION OF QUALITATIVE FEATURES FOR STAGING

The Figure 4.7 shows 5 selected specimens, ordered in obvious temporal sequence. The 3Ds show how the SPL folds to form the CC. The early CC extends bilaterally and subdivides

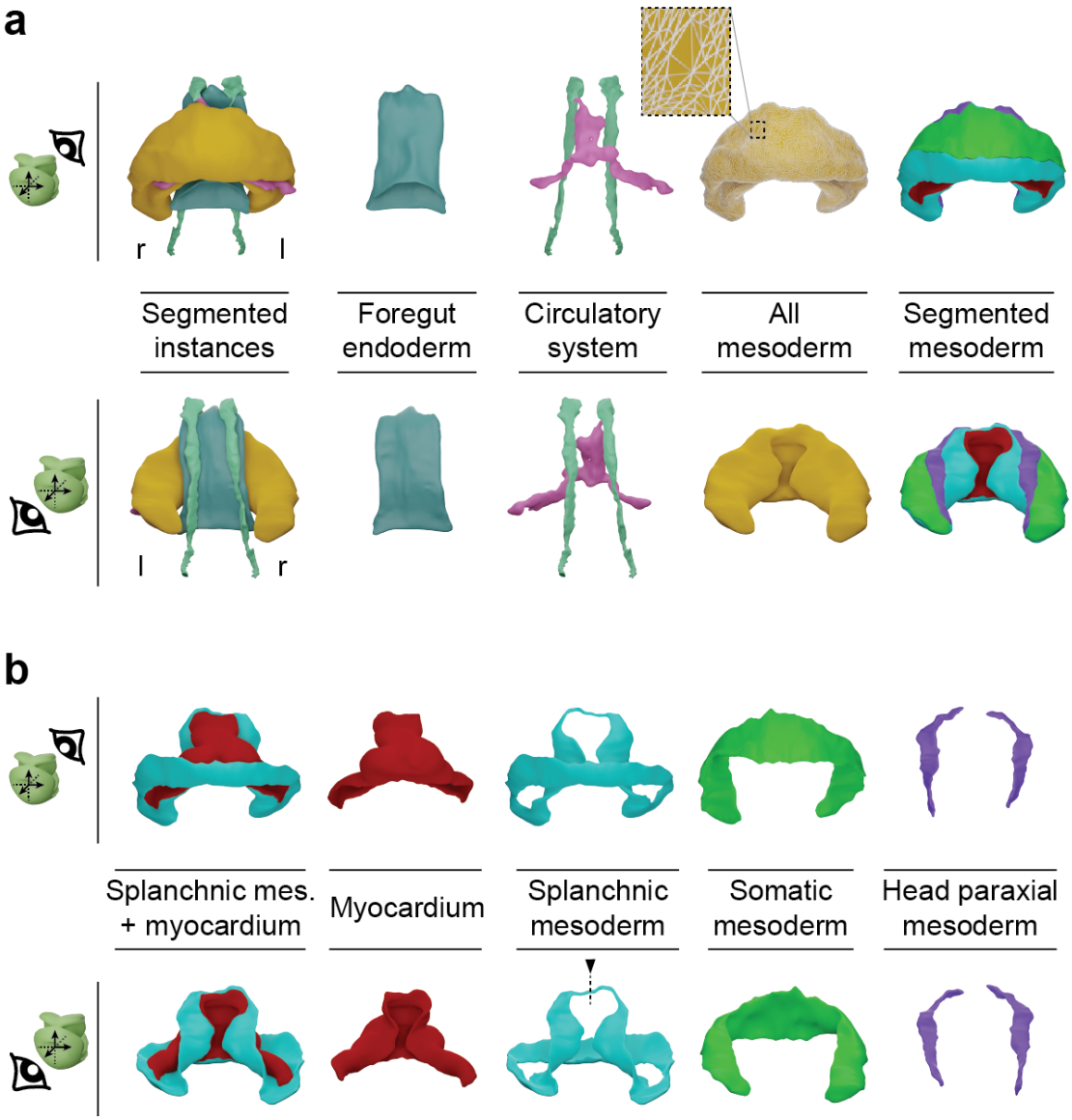

Figure 4.6 | **Meshes representing the tissues and structures of interest. a**, The panel shows the three-dimensional reconstruction of all tissues, described as meshes. The dotted box shows a detail of how the mesh is built. **b**, Sub-types of the segmented mesoderm, represented as meshes. Dotted line in the SPL shape, ventral view, represents the cut trajectory to achieve genus 0 topology (see section 3.19).

the undifferentiated SPL into medial and distal domains. The medial domain contains the second heart field (SHF) precursors, while the distal domain (named as juxta-cardiac field (JCF)) contains precursors of the epicardium and the septum transversum, and bears myocardial differentiation capacity [146].

The examination of the collection of datasets reflected high morphological heterogeneity of the developing anterior celomic cavity (ACC). This observation is appreciated within groups of embryos at an apparently similar developmental stage, as judged by somite number, HF and FP shapes. The Figure 4.8 shows the two hearts highlighted within the dotted boxes in Figure 4.7, together with a collection of hearts at an apparently similar stage.

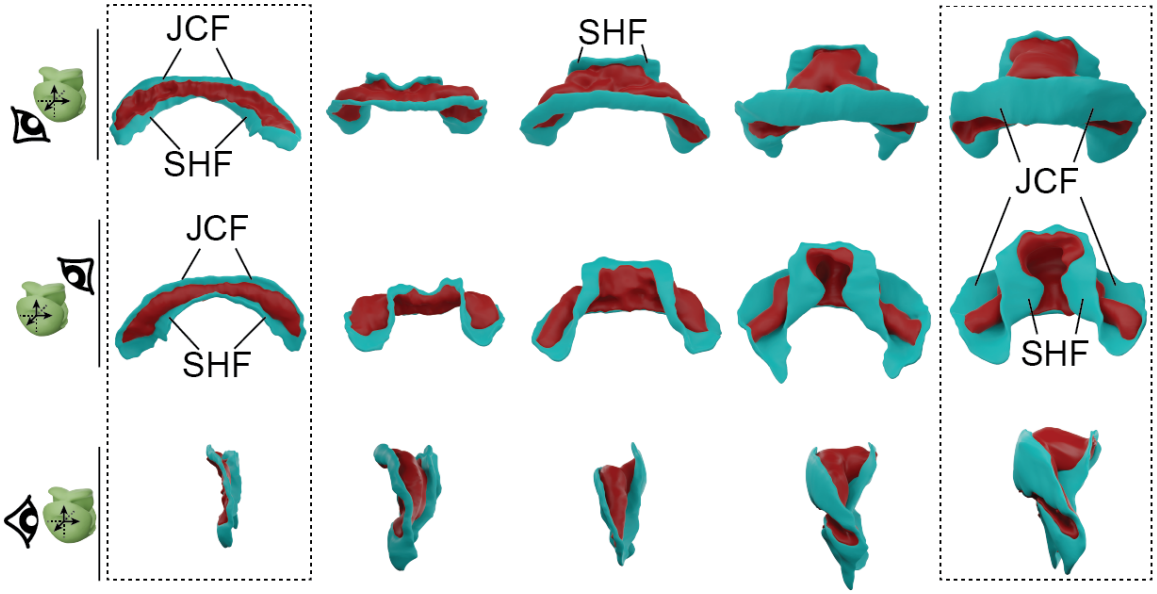

Figure 4.7 | **Observation of qualitative morphometric aspects of heart tube morphogenesis.** Ventral, dorsal and lateral views of five specimens ordered according to developmental time. SPL is represented in blue, and MYO in red. The dorsal view shows the progressive dorsal closure of the heart tube and the medial expansion of the second heart field. Dotted boxes represent specimens further analyzed in Figure 4.8. JCF, juxta-cardiac field; SHF, second heart field; SPL, splanchnic mesoderm.

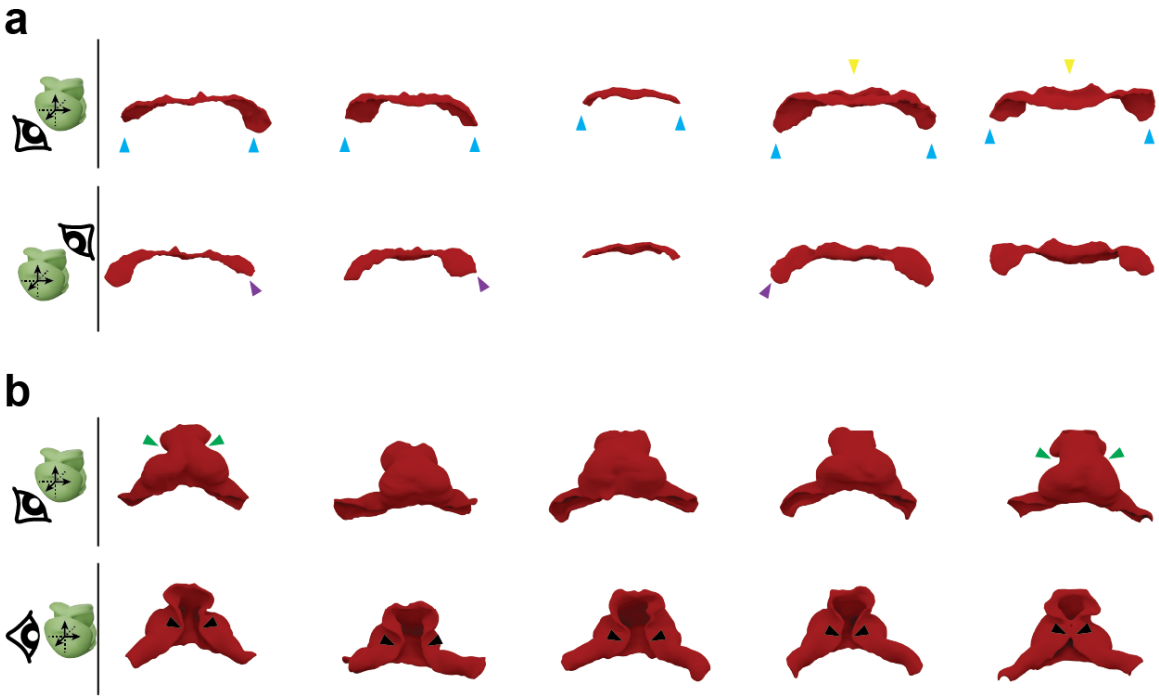

Figure 4.8 | **Groups of hearts of similar developmental stage show high morphological variability.** **a**, Group of hearts at CC stage from ventral (top row) and dorsal (bottom row) view. Purple arrows point to inflow tracts not developed symmetrically. Blue arrows highlight the lateral extension of the CCs. Yellow arrows point to the CC showing more advance state of development. **b**, Group of hearts at HT stage from ventral (top row) and dorsal (bottom row) view. Black arrows point to the dorsal closure region. Green arrows point to OFT that show more advance conformation features.

According to Figure 4.8, it can be seen that morphological variability extends to conformation features such us proportions, local morphological details and general geometrical aspects. For instance, regarding the earliest group shown (Figure 4.8a), it can be seen that lateral extension is highly variable (blue arrows), indicating discrepancies in global size. In the other hand, looking at the lateral domain of the CC, the detachment of the differentiated MYO, that builds up the right sinus horn (RSH) and left sinus horn (LSH), seems not to happen symmetrically in some specimens. In the most medial domain, some specimens show a more pronounced CC shape (yellow arrows). Regarding the latest group shown (Figure 4.8b), we observe variability in the degree of dorsal closure and also the presence of non-stereotyped bulges of different sizes at different locations. In later specimens, where the looping is more obvious, we also observe variability in the degree of looping.

Then, we looked into the shape of the FGE, AOL and EL, as their development is concomitant with the transformation of the CC. We were expecting that these structures would not be so variable in morphology during development. The 3D reconstructions (see Figure 4.9) show the formation of the EL and the AOL. It can be seen that an intermediate stage between the EL and the HT, the EL forms a continuous lumen that extends laterally, within the heart. At the same time, the AOL seems to already be forming a continuous cord, located at the dorsal face of the FP. It can also be seen that the anterior limit of the AOL reaches the FP shoulders, and bend over them. At later stages, the EL starts to develop along the anterior-posterior axis, hand by hand with the forming of the OFT. The AOL, at its most anterior tip branches in two. In parallel, the AOL become thicker. At some point the AOL enter in contact with the EL through the first branchial arc arteries, thus forming a continuous with the rest of the vasculature. It must be noted that the whole extension of the aortae is not show in the 3D, being the reason that the imaged field of view did not contain the complete aortae.

As discussed previously for the heart, we have noted that the morphology of the FP (Figure 4.9a) in embryos at an apparently similar stage differ in morphology. They do so by the level of invagination of the FGE. We have also seen that the development of the AOL is highly variable, and found specimens at the same stage with and without signs of onset of AOL formation. Finally, the EL (Figure 4.9b) creates a continuous, laterally extended sealed tube, at different stages.

We conclude from this visual analysis that subjective ordering of the heart specimens is not a reliable path, and therefore a morphometric approach should be taken.

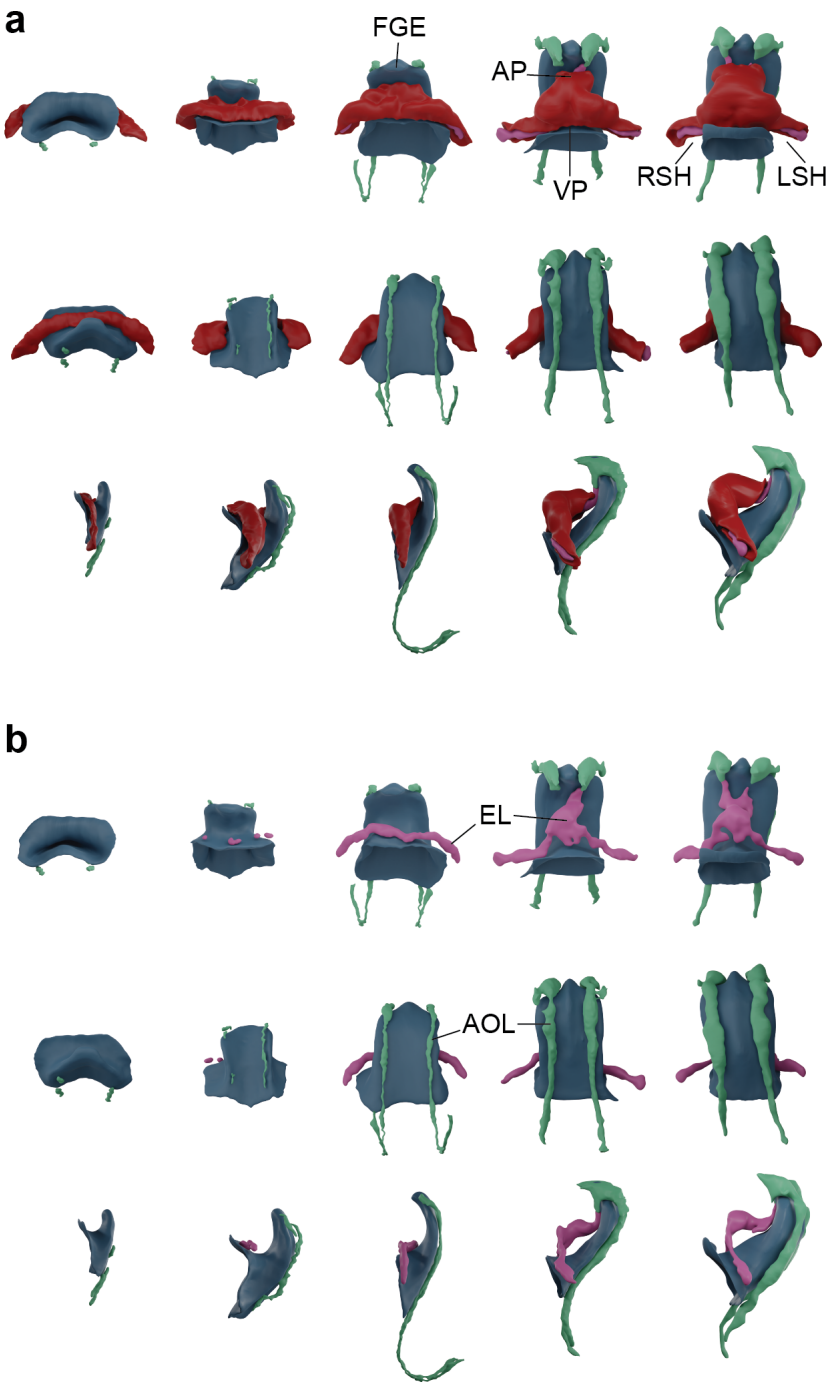

Figure 4.9 | **Structures concomitant with heart tube formation. a**, Morphology of the myocardium together with the foregut endoderm and the circulatory system lumen. The different lengths of the aortae seen in the three older specimens are due to variable imaging depth. **b**, Gradual development of the circulatory system in parallel to the foregut endoderm invagination. The ventral view shows the progressive formation of the endocardial lumen, and the lateral view shows the progressive formation of the aortic lumen along the dorsal surface of the foregut endoderm. VP, venous pole; AP, arterial pole.

4.5 MORPHOMETRIC STAGING OF HEART TUBE FORMATION

In order to tackle the problem of staging despite the variability discussed in section 4.4, we have calculated different morphometric features, using the morphologies we have generated. In order to test a wide range of morphometric measures, we have first defined a wide range of landmarks (see section 3.9) on top on every tissue (see Figure 4.10 and Figure 3.16). These represent topological places of biological relevance, that can be followed and defined in any shape at any stage (see section 3.9).

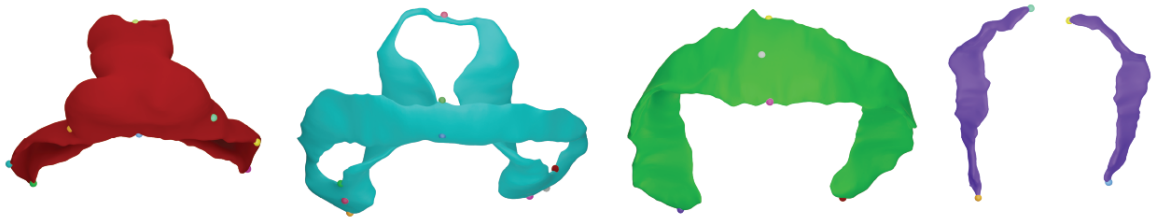

Figure 4.10 | **Definition of landmarks in the tissues forming the pericardial cavity.** Figure shows, from a ventral view, the set of different landmarks that have been defined for every tissue. See Figure 3.16 for more detailed specifications.

Next, we elaborated a simplified version of surfaces by reducing its thickness to zero (see Figure 3.17 and section 3.10).

Using the landmarks and the mid-surfaces defined above, we have drawn on each mid-surface different curves, calculated their distances, and used this information as staging markers. Finally, in order to provide non-dimensional parameters, we have associated different pairs of distances, and calculate their ratio. In this manner, not only the biological information is captured but also it is done in scale non-dependent manner.

The morphological parameters we have decided to use comes from the observation of the dataset we have elaborated. From all the possible proportions that can be calculated from the curves, we have paid special attention to the ones that give proportions that are expected to vary continuously during the studied period. For instance, given that the cardiogenic area evolves from a crescent extending from left to right to a tube extending from cranial to caudal, a general trend during the formation of the heart tube is the increase of the height (cranio-caudal size) to width (left-right size) ratio of the tissues involved.

One of the metrics we have considered comes from the fact that, as the morphogenesis process that shapes the CC into the cardiac tube happens, it can be seen that the limit formed between the JCF and the forming HT remains rather stable. This effect can be better appreciated in Figure 4.11. However, the border between the medial SPL and the forming HT undergo a drastic deformation. Indeed, this deformation, that is essential for the generation of the outflow tract (OFT) and allows the dorsal closure, transforms the CC into the primitive HT. This transformation is concomitant with the development of the FP. The unbroken contact between the medial SPL and the dorsal region of the heart with the FGE, shows an interplay between the formation of both organs.

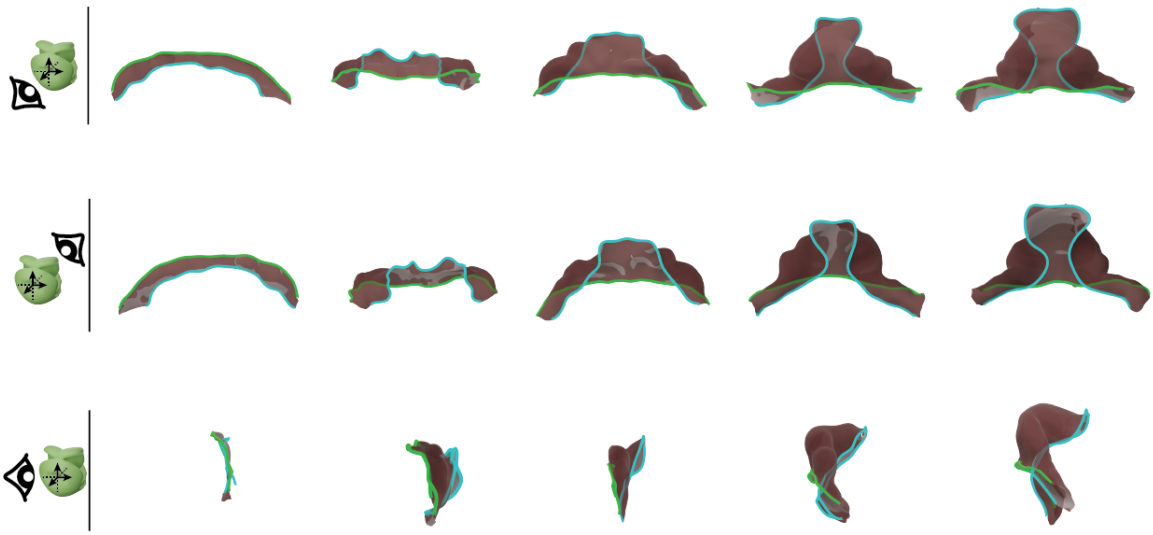

Figure 4.11 | **Curves defining the limit between differentiated myocardium and other mesodermal domains.** Figure shows a ventral, dorsal and lateral view of a set of mid-surfaces of myocardium shapes, highlighting the border with other mesodermal domains. The green lines shows the limit between MYO and JCF and the blue line shows the limit between MYO and SHF.

As described in the former paragraph, we have thus considered the distance of each one of those curves (d_1 and d_2), and calculated their ratio as d_1/d_2. Figure 4.12a illustrates the approach taken to calculate such parameter, that we have named staging parameter 1 (SP1). Figure 4.12b shows other examples of staging parameters explored, that relate height-to-width ratio variations.

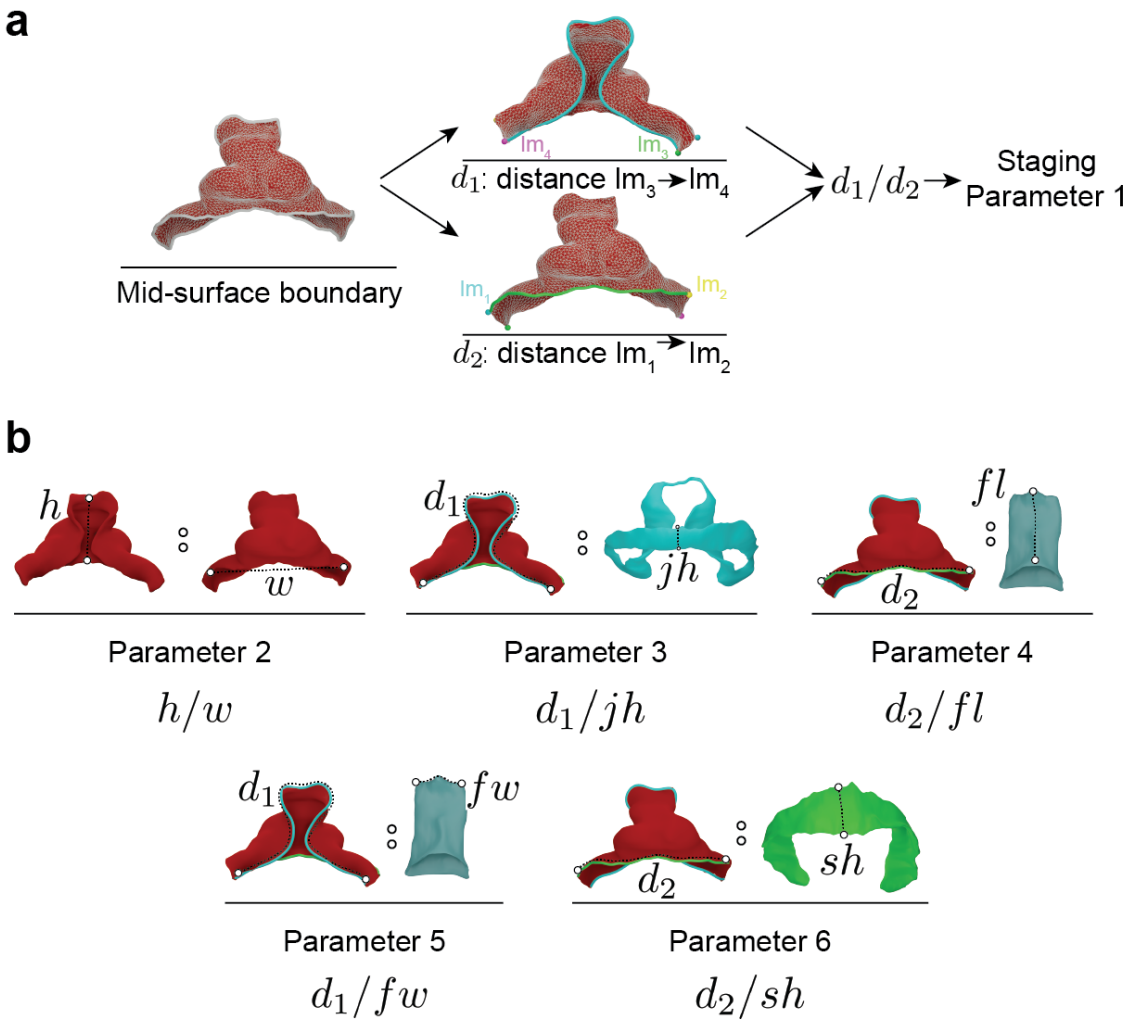

Figure 4.12 | **Geometrical parameters explored for staging. a**, The panel shows the details of the calculation of staging parameter 1. **b**, The panel shows some others parameters suggested for staging. h, myocardium height; w, myocardium width; jh, juxta-cardiac field height; fl, foregut pocket length; fw, foregut pocket width; sh, somatic height.

We have also explored the parameters shown in Figure 4.13. However, as it will be shown later, we will restrain the analysis to the ones shown in the Figure 4.12, as they are the best performing ones.

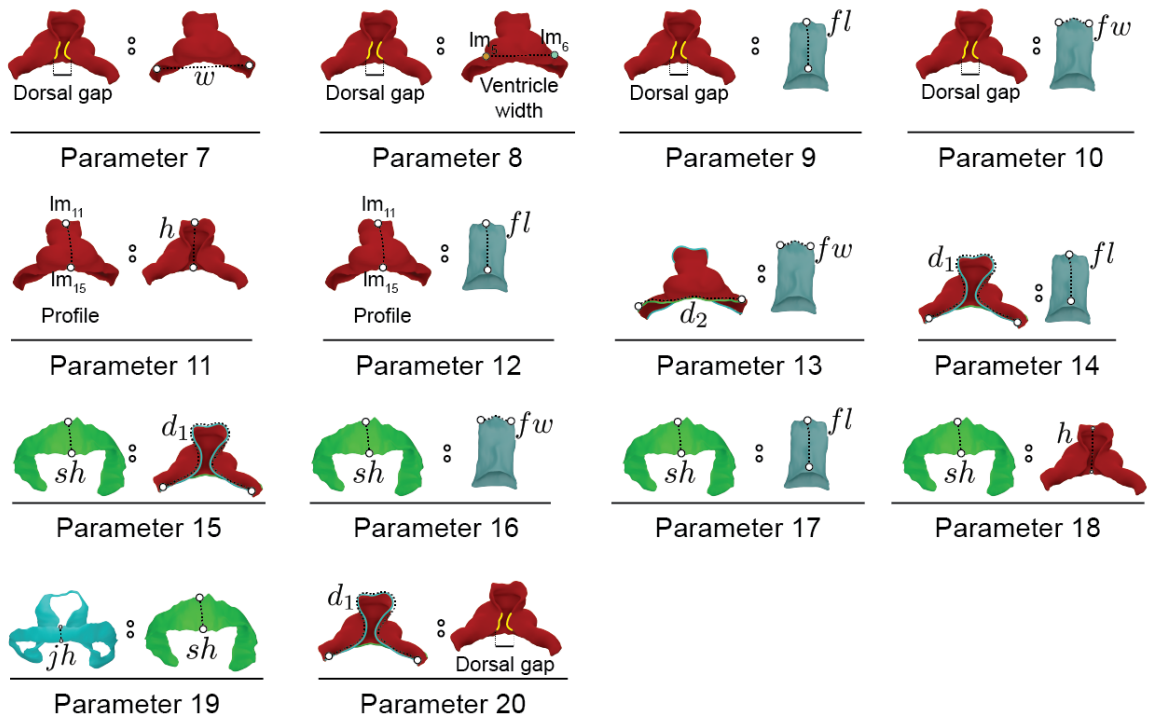

Figure 4.13 | **Additional staging parameters explored.** Schematic representation of additional parameters explored for the staging system.

In order to determine the staging parameter that best classifies the collection, we calculated the values of the parameters shown in Figure 4.12 and also tested several others (see Figure 4.13). We then applied a classification algorithm, based on *k-means* clustering [147] (see section 3.21). First, we selected the specific staging parameter under which to organize the collection. Second, we set as input the desired number of groups (k). As an output we obtained, for every specimen, a target cluster and a metric that measures how good its resulting classification is, s. Next, we took all the s values and calculated the average silhouette coefficient ($\bar{s}$), which measures the goodness of the classification of the whole collection. This process is schematized in Figure 4.14 (see section 4.5).

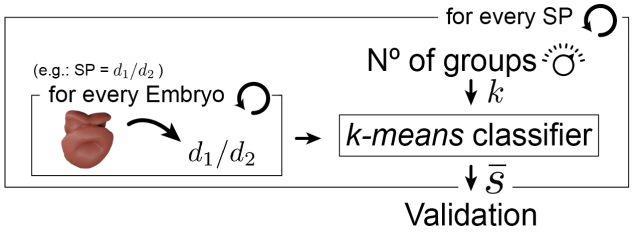

Figure 4.14 | **Pipeline for testing and validation of staging parameter.** Pipeline followed to classify the collection according to every staging parameter. For every staging parameter, we have tested a different number of groups and calculated a validation metric. SP, staging parameter.

Figure 4.15 shows the validation results after testing different staging parameters and different number of clusters. We can see that, as we increase k, the best performing classification was obtained for the d1-to-d2 ratio (d_1/d_2) proportion (red line), d1 being the length of the border between the MYO and JCF, and d2 between the MYO and SHF. The maximum $\bar{s}$ was obtained for a k-means classification into 10 groups. For k>10, although not shown in the graph, we could see a sudden decrease in the validation mark.

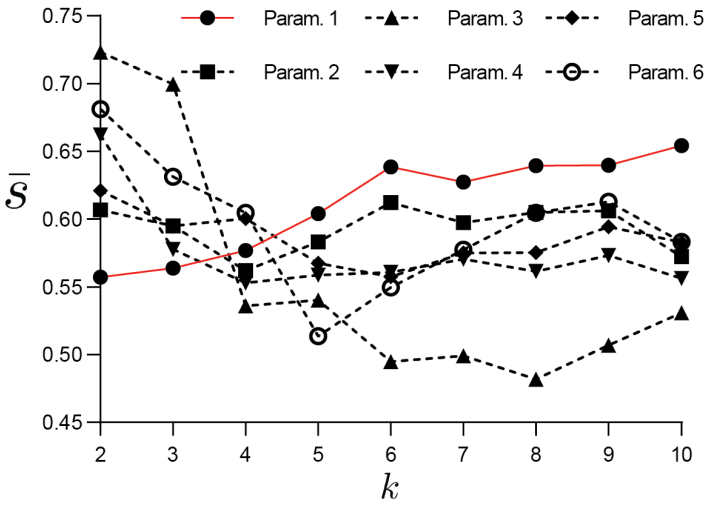

Figure 4.15 | **Validation of different staging parameters.** Plot shows the value of the validation metric for different staging parameters and varying number of groups.

We obtained the highest value of $\bar{s}$ for the six staging parameters shown in Figure 4.12. Figure 4.16 shows the obtained values of s for every specimen, when setting $k = 10$, and using these parameters.

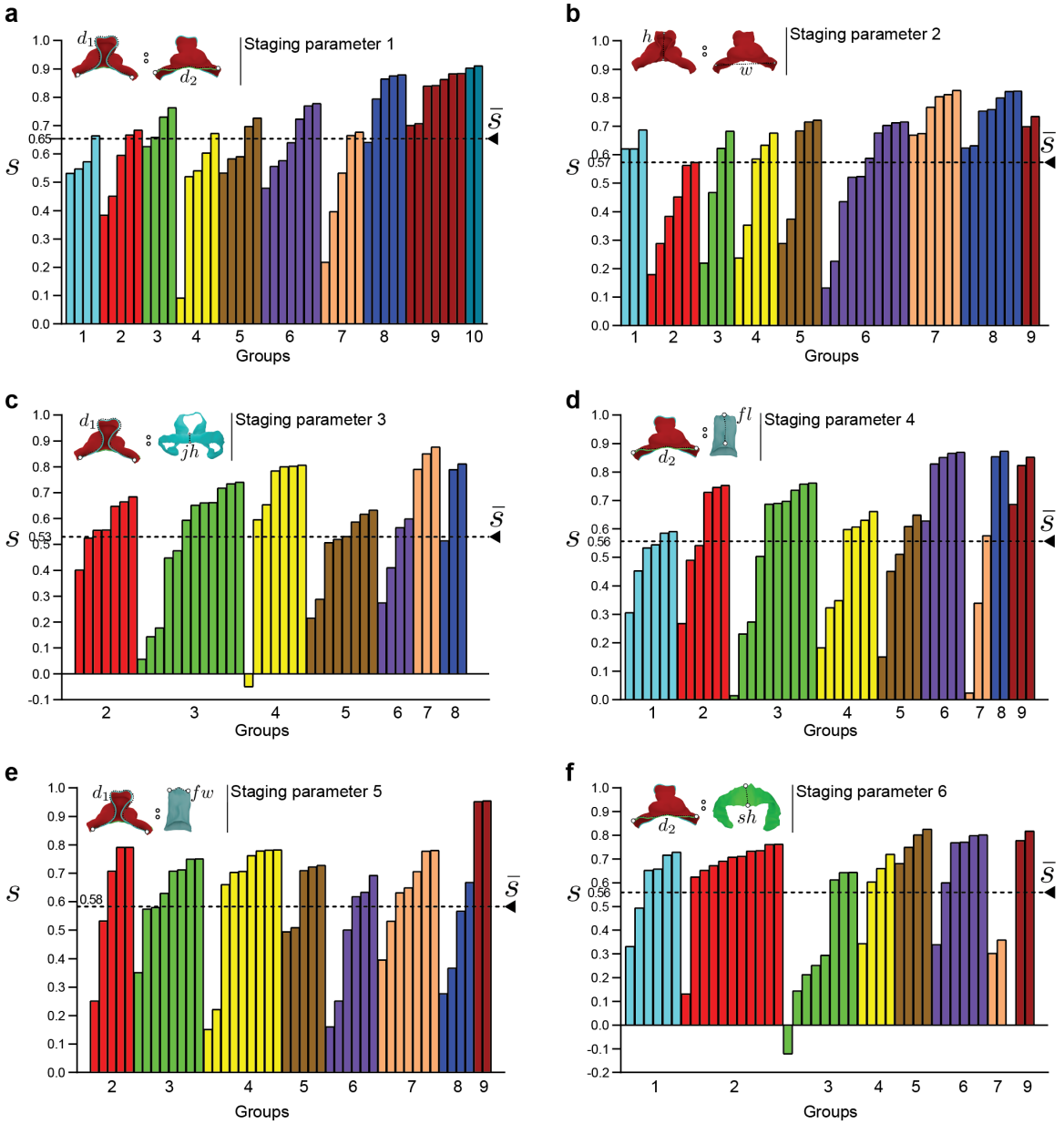

Figure 4.16 | **Silhouette coefficient plot for the different staging parameters explored, classified using k-means and number of groups equal to 10. a-f**, Bar graphs showing the silhouette coefficient value (s) for each embryo in the collection classified into 10 groups, according to the different staging parameters. The graphs also show the average value $\bar{s}$, which is maximal for parameter 1. Bars are color-coded according the group.

We therefore concluded that d_1/d_2 was the best single parameter for classifying the collection and established these 10 groups as a reference for study (Figure 4.17). While the establishment of groups is useful to understand the morphological evolution of the heart, the d_1/d_2 parameter is a continuous variable and allows the allocation of single specimens along the heart tube developmental trajectory, independently of grouping.

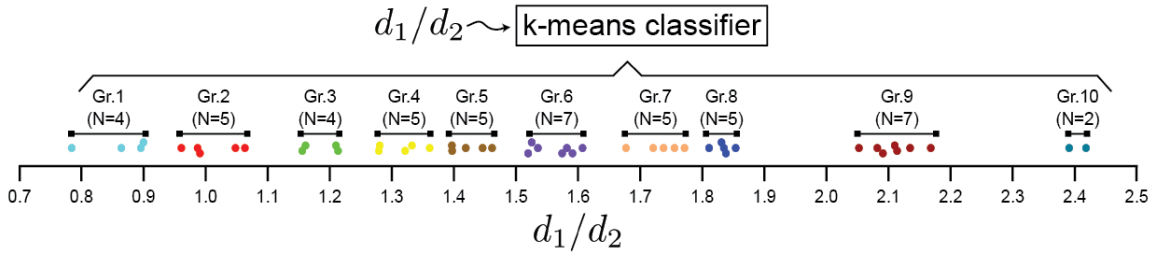

Figure 4.17 | **Distribution of the specimens in the d_1/d_2 spectrum.** The plot shows how the specimens of the collection are distributed according to their d_1/d_2 value. The color of the dots indicate specific cluster identities. N, number of specimens.

4.6 ANALYSIS OF THE STAGING GROUPS

In order to have a vision of how good the different classification methods are with respect to d_1/d_2, we have studied its correlation with the rest of the parameters. The best correlate to d_1/d_2 was the height-to-width ratio (h/w), which showed a high linear correlation, as shown in Figure 4.18.

This high correlation between d_1/d_2 and h/w suggests a more accessible and user-friendly approach to stage a specimen. Measuring both parameters can be performed on unsegmented raw data images or even histological sections, where the points that measure such dimensions can be set (see section 4.10).

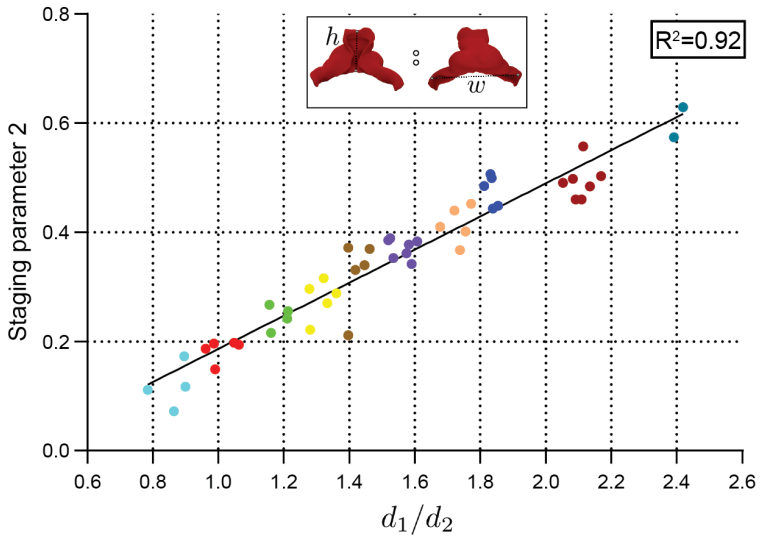

Figure 4.18 | **Correlation between staging parameters d_1/d_2 and h/w.** The plot shows the high correlation existing between both staging parameters.

By contrast, other parameters showed a poor correlation. Such is the case that relates d_1/d_2 with d_1 to juxta-cardiac field height (jh) (see Figure 4.19a) and also with d_1 to foregut pocket width (fw). However, we found a tight, non-linear correlation relating staging parameter 4 (d_2/fl) as shown in Figure 4.19b. This is also the case for staging parameter 6 (Figure 4.19d). These last two points indicate that staging parameters relating measures from different tissues and/or structures can have different staging potential, depending on the time of the analysis.

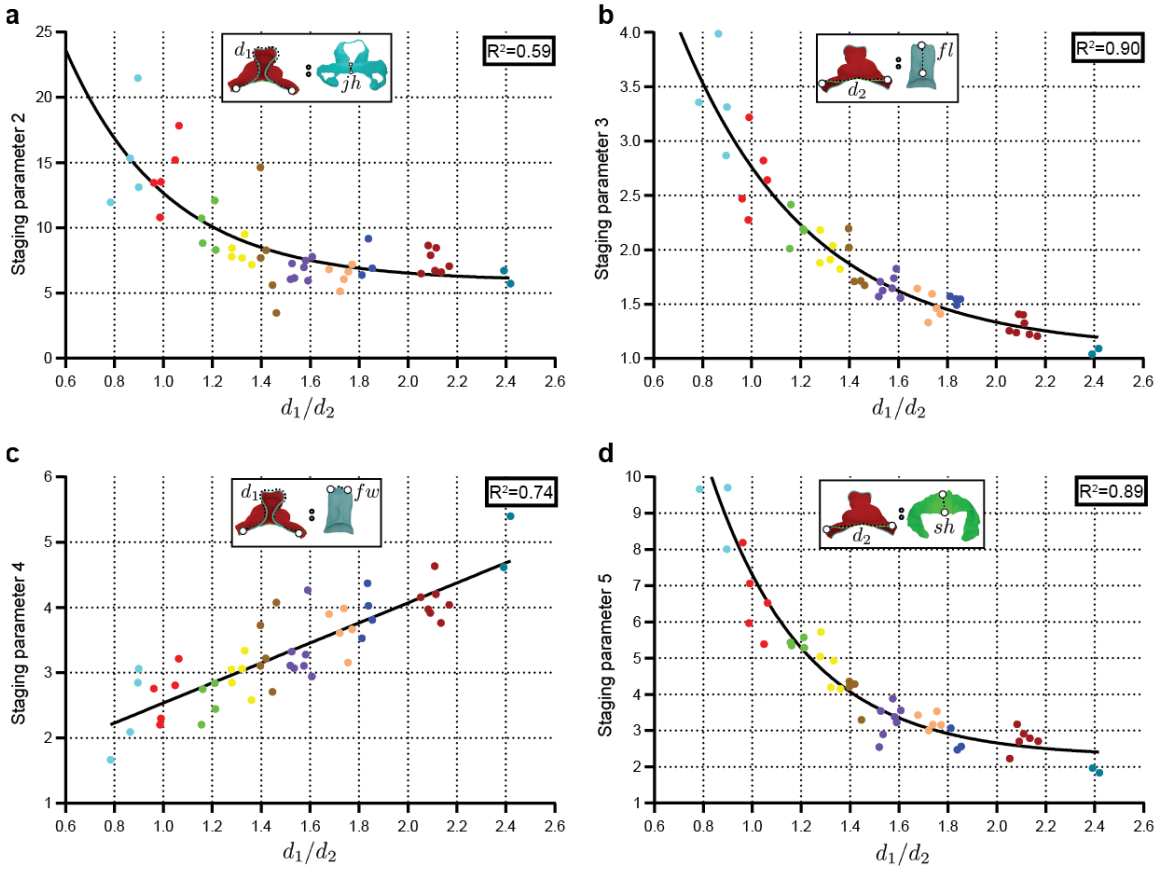

Figure 4.19 | **Correlation between staging parameters d_1/d_2 and h/w.** The plot shows the high correlation existing between both staging parameters.

We have also validated the parameter d_1/d_2 as the best staging parameter by considering the distribution of the number of specimens in each group. As it can be seen in Figure 4.20, this parameter forms the most homogeneous distribution, creating groups with an average of 5 members, one group with the minimum equal 2, and two groups with the maximum equal 7.

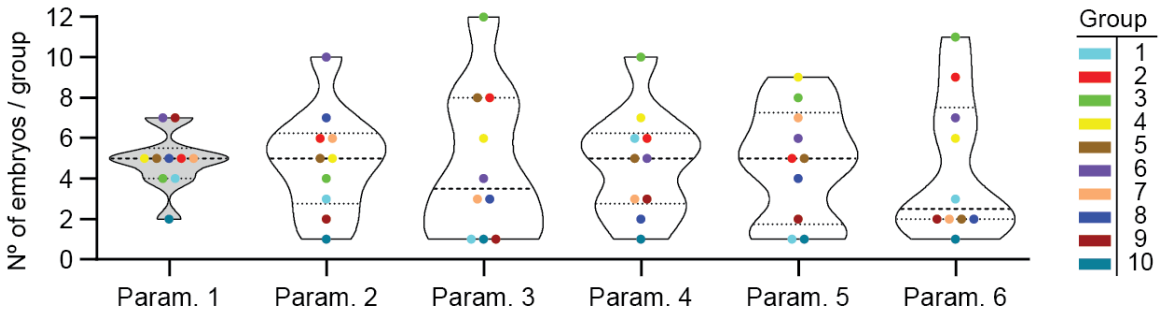

Figure 4.20 | **Distribution of number of specimens by staging parameter.** The violin plots show the distribution of the number of specimens in each group, according to different staging parameters.

We have observed that, strikingly, the absolute width of the forming cardiac tube, which approximately coincides with the width of the pericardial cavity, not only does not increase during development but also shows a mild trend to reduction as development progresses

(Figure 4.21). This aspect indicates that, despite overall embryo growth, the lateral expansion of the pericardial cavity seems restricted. By contrast, the dorsal–ventral and cranio–caudal dimensions of the pericardial cavity and all associated tissues, including the forming heart tube, strongly increase during this period. This aspect correlates well with the extensive deformation that the curve d1 undergoes, which is associated with MYO and SPL remodeling, in contrast with d2, which mostly remains stable.

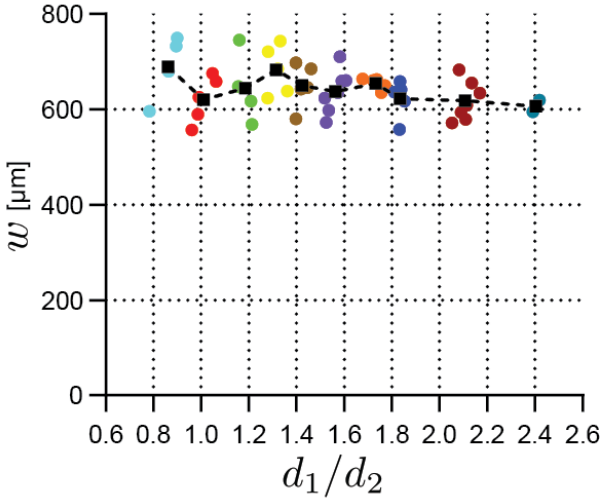

Figure 4.21 | **Heart width as function of d_1/d_2.** This plots shows the correlation between the staging value d_1/d_2 and the width of every heart. The color related to the identity of every group, as indicated in the sable of Figure 4.20.

The geometries of all the tissues segmented for every specimen classified by stage are shown from Figure A.1 to Figure A.7. Groups 1 to 4 represents different stages of CC development, while groups 5 to 8 can be assigned to linear HT stages and groups 9 and 10 to heart looping stages.

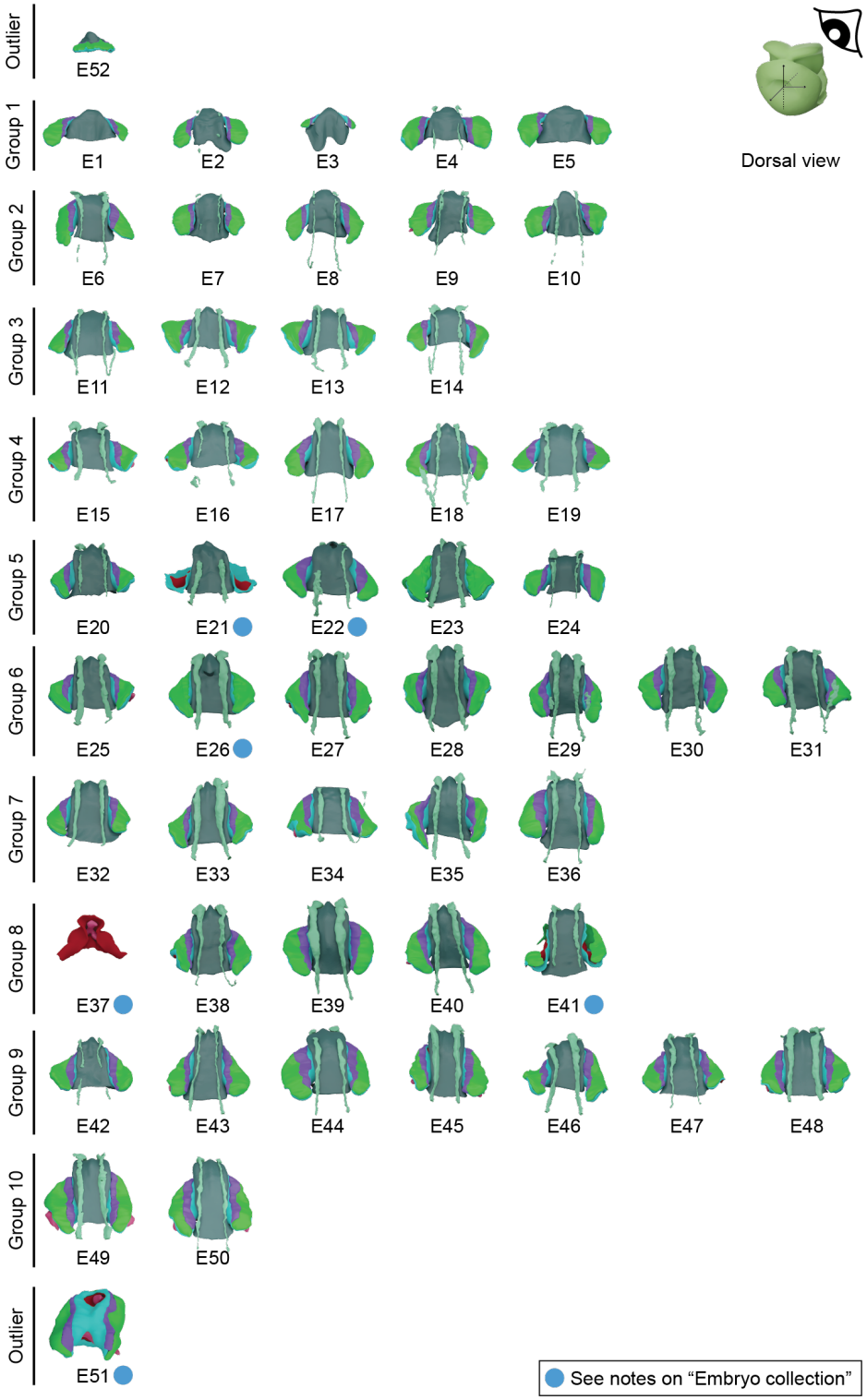

Figure 4.22 | **Embryo collection classified by staging groups, showing a dorsal view of all tissues.** Dorsal view of all the specimens in the collection with representation of the processed surfaces 27 of the complete set of tissues and shapes as described in Figure 4.6. Specimens E51 and E52 are outliers, left out of the stage classification.

We also studied the occurrence of developmental events, such as dorsal closure and looping, which are known to progress continuously in live-imaged single specimens [5, 36]. Heart tube rotation and looping, as described in [36], is appreciable in all specimens of group 10 and most specimens of group 9 (except E42 and E46) without signs of looping in specimens of other groups (Figure A.2 – Figure A.5).

We also measured the dorsal mesocardial gap (DMG) as a read out of dorsal closure progression (section 3.12, Figure 4.23). This gap is initially wide open in the CC and progressively narrows until disappearing concomitantly with dorsal mesocardium establishment and linear HT formation. While dorsal closure appeared predominantly associated with looping and, therefore, was seen in all specimens in group 10+ and most specimens in group 9, we also found some hearts already closed in group 8 (E41) and group 6 (E29), while some specimens at stage 9 were clearly advanced in looping but quite delayed in dorsal closure (E44 and E48; Figure A.2 minus Figure A.5). In agreement with these observations, DMG correlation with d_1/d_2 was quite noisy (Figure 4.23), indicating that the degree of dorsal closure is not a reliable parameter for staging. This can be seen in the linear fitting accompanying Figure 4.23, together with a relatively low goodness of fit.

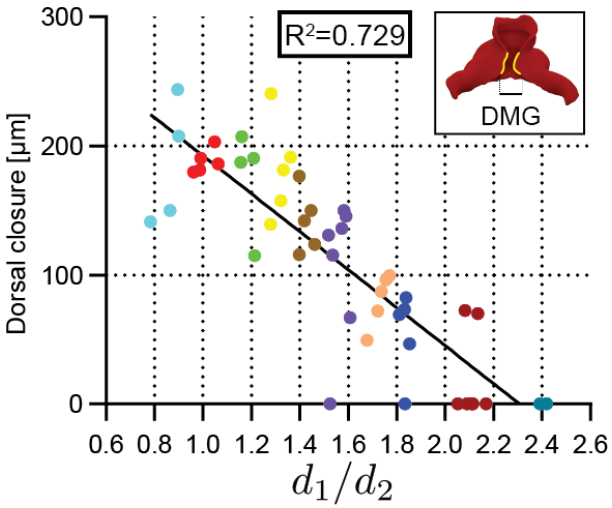

Figure 4.23 | **Dorsal mesocardial gap doesn't correlate well with d_1/d_2.** Scatter plots showing dorsal gap as a function of d_1/d_2. DMG, dorsal mesocardial gap. The black continuous line shows the calculated linear fitting.

4.7 THREE-DIMENSIONAL ATLAS OF HEART TUBE FORMATION WITH LOCAL SHAPE VARIABILITY

Given the variability found between specimens in the same staging groups (Figure 4.22 and Figure A.1 - Figure A.7), we next aimed to quantify and spatially map the shape variability of the differentiated MYO within each of the 10 groups established and to define a consensus geometry for each group (Figure 4.24).

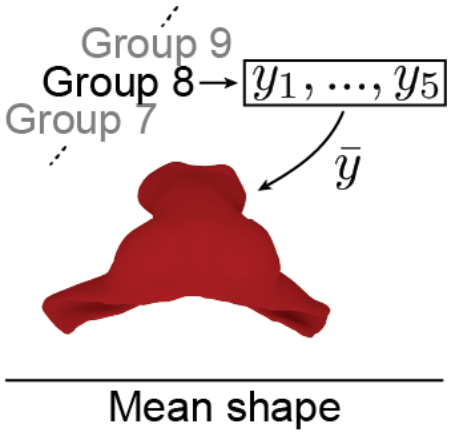

Figure 4.24 | **Consensus geometry for group 8.** Illustration of the concept of mean shape for staging group 8.

For each group, we chose a *reference* specimen whose d_1/d_2 was closest to the average d_1/d_2 of the group (Figure 4.25a, y_1 specimen). We then used surface map computations [103]. This approach uses a set of landmark points to establish a vertex-to-vertex correspondence between two shapes. By doing this, the mesh defining a reference shape is distorted into the form of a *target* shape. Therefore, we established this correspondence between the reference specimen and all shapes of the group (Figure 4.25b, Figure 3.16 and section 3.9). This generated, for every vertex in the reference mesh (blue dot in Figure 4.25c), a set of equivalent vertices corresponding to the other shapes in the group (red dots in Figure 4.25c). Next, we found the average position of each set of equivalent vertices and constructed a mean shape for each group (MSG) (Figure 4.25c).

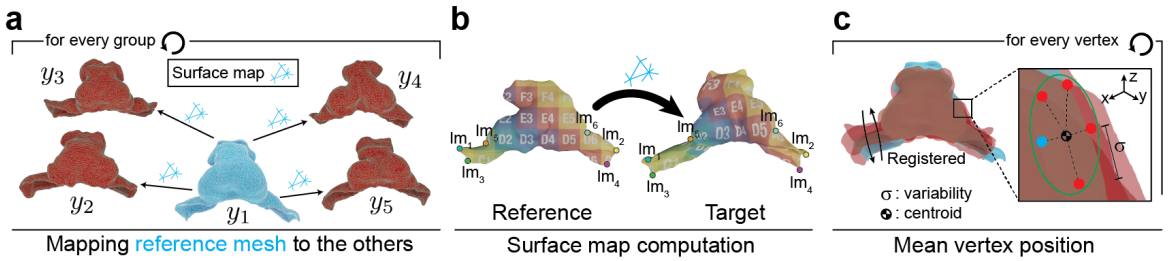

Figure 4.25 | **Workflow for calculating mean shapes. a**, Process of surface map computation. The blue shape is the reference mesh of the group. The arrows represent the transfer of the mesh from the reference mesh to all other in the staging group. **b**, Working principle of the surface map computation. The landmark (lm) identify corresponding locations in the reference and target mesh. The colored matrix drawn of top the target shape represents the deformation that the mesh from the reference mesh undergoes. **c**, Every vertex of the reference mesh (blue dot) has a corresponding point on the other shapes (red dots).

This generated a collection of 10 MSGs that represents the average evolution of MYO shape during the formation of the primitive HT and initiation of looping (Figure 4.26).

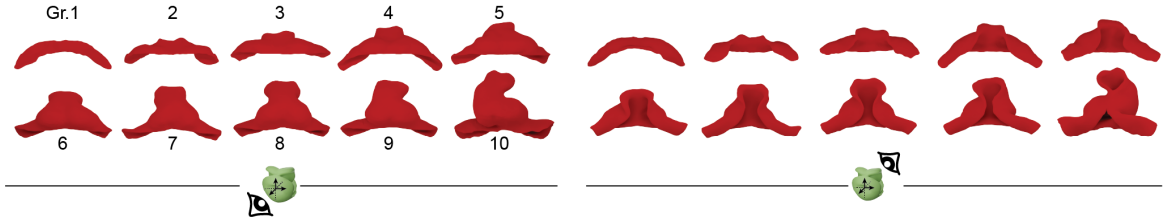

Figure 4.26 | **Mean MYO shapes and morphological variability for each staging group.** Calculated MYO mean shapes for every staging group. Each side show the mean shapes from ventral (left) and dorsal (right) views. The numbers indicate the number of group.

We then computed the per vertex variability among the specimens of each staging group and plotted it on the MSG collection (Figure 4.26c). In this way, we were able to identify hot spots of variability within each of the 10 different groups (Figure 4.27). In most groups, we found that high variability appeared in the OFT, inflow tract (IFT) and dorsal lips of the MYO. During primitive ventricular chamber formation, we found that variability concentrated first at the bilateral bulges that start to form the chamber and later at the midline, possibly in relation to the variability in the degree of merging of the two initially bilateral bulges into one. Finally, in group 9, high variability was observed in all structures involved in the looping process. Variability was not measured in group 10, given that this group is composed of only two specimens. This collection of MSGs provides information on the standard shapes of different stages of primitive HT formation and the local variability of the process.

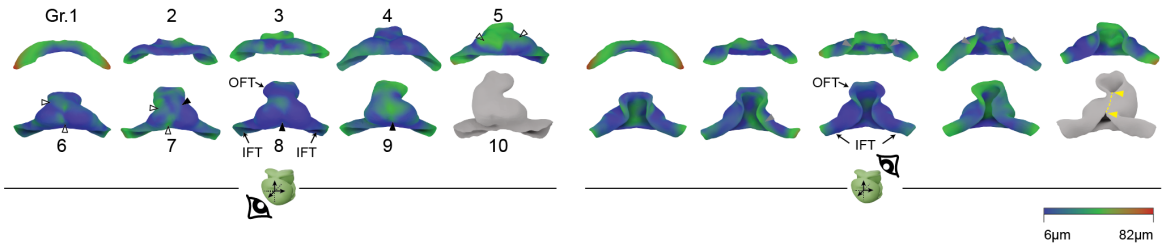

Figure 4.27 | **Mean MYO shapes and morphological variability for each staging group.** Mean shapes color coded according to the morphological variability calculated for each vertex. The shape in gray indicates that the low number of specimens at this stage precludes variability calculation. The yellow dotted line and arrows represent the cut trajectory to achieve genus 0 topology in dorsally closed hearts (see section 3.19). Arrowheads indicate the regions of higher variability in medial ventricular regions (solid) and lateral ventricular regions (open).

We also wanted to identify the specimen whose MYO best represents its stage group, as this would give us access to representative geometries of the other tissues as well. For this, we identified the medoid shape for each group, that is, the geometry with the smallest accumulated difference with respect to all others in the group (section 3.17). In this way, we identified a concrete specimen as Representative Shape for each Group (RSG) representative shape for each group (see Figure 4.28a). Using the RSG for each group, we also took their accompanying tissues forming the complete ACC, thus having a complete description of all the tissues involved (see Figure 4.28b).

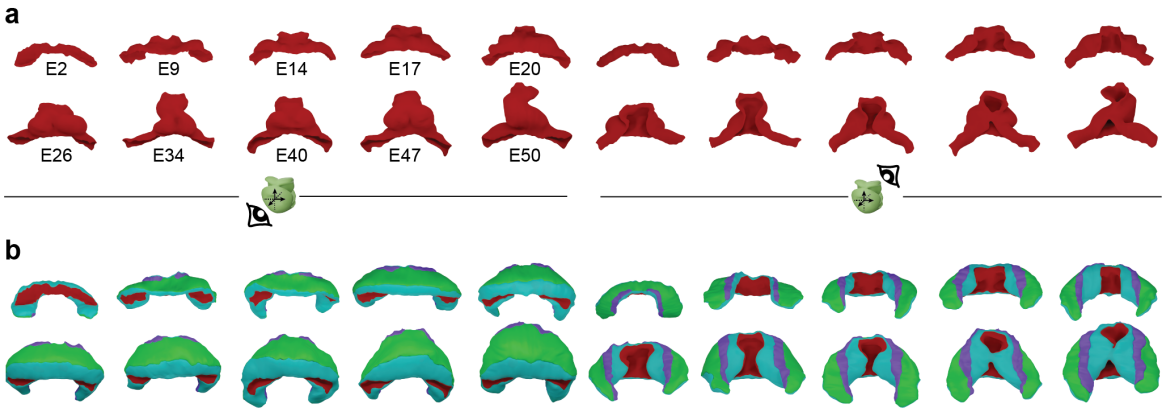

Figure 4.28 | **Representative specimens of each staging group. a**, Ventral and dorsal view of the representative MYO shapes. **b**, Ventral and dorsal views of the tissues forming the PC of the representative embryos.

4.8 EARLY LEFT–RIGHT ASYMMETRY OF THE CARDIAC INFLOW TRACTS

Heart tube looping is considered the earliest morphogenetic expression of left–right asymmetry in a mammalian developing organ. Here, we identified obvious signs of heart looping in stages 9 and 10; however, we wanted to explore systematically whether less obvious asymmetries might be present before the looping stage.

Studying both the whole specimen collection and the collection of MSGs, we detected a possible recurrent difference in the angle of insertion of the IFTs. To study this

aspect in more detail, we defined the direction of insertion of the IFTs via polar coordinates in a local system of orthogonal axes in which the xy plane is transversal to the embryo, and the z axis is aligned with the embryo anterior-posterior axis (Figure 4.29 and Figure 3.21 for further details). The direction of insertion of the IFTs is then defined by two angles: the θ angle and the φ angle (Figure 4.29).

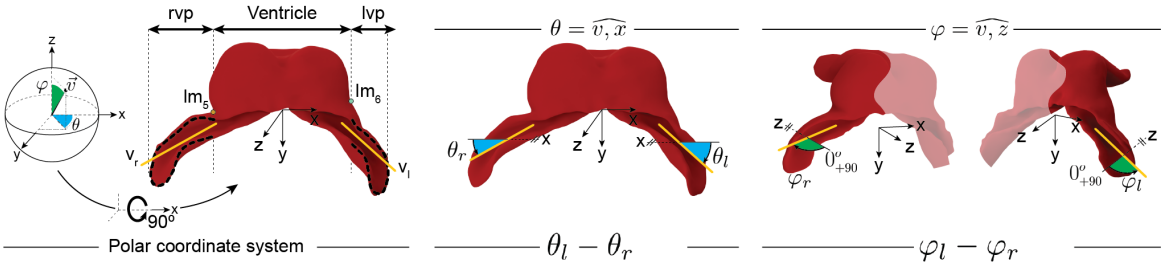

Figure 4.29 | **Representative specimens of each staging group.** Schemes show the calculated principal directions of the IFT (orange lines) and the polar coordinates system with θ and φ angles.

When studying the evolution of these angles, we sought for asymmetric difference in the angle values (i.e.: $\theta_l - \theta_r \neq 0$) between both sides in correlation to the staging parameter d_1/d_2. We found that the θ angle progressively diverged between the left and right sides (Figure 4.30a, 'Atlas'), while the φ angle, on average, remained symmetric (Figure 4.30c, 'Atlas'). The θ angle significantly deviated from symmetry starting at $d_1/d_2 \approx$ 1.55 (Figure 4.30b), which corresponds to group 6 (Figure 4.17). The asymmetry of the θ angle further increased during the looping stages $d_1/d_2 \geq 2$ until reaching a 20° difference (Figure 4.30a, 'Atlas'). On the other hand, it can be seen (Figure 4.30d) that the difference in the φ angle does not reach a significant value, although a slight change of tendency can be appreciated from $d_1/d_2 \approx$ 2.2 (Figure 4.30c).

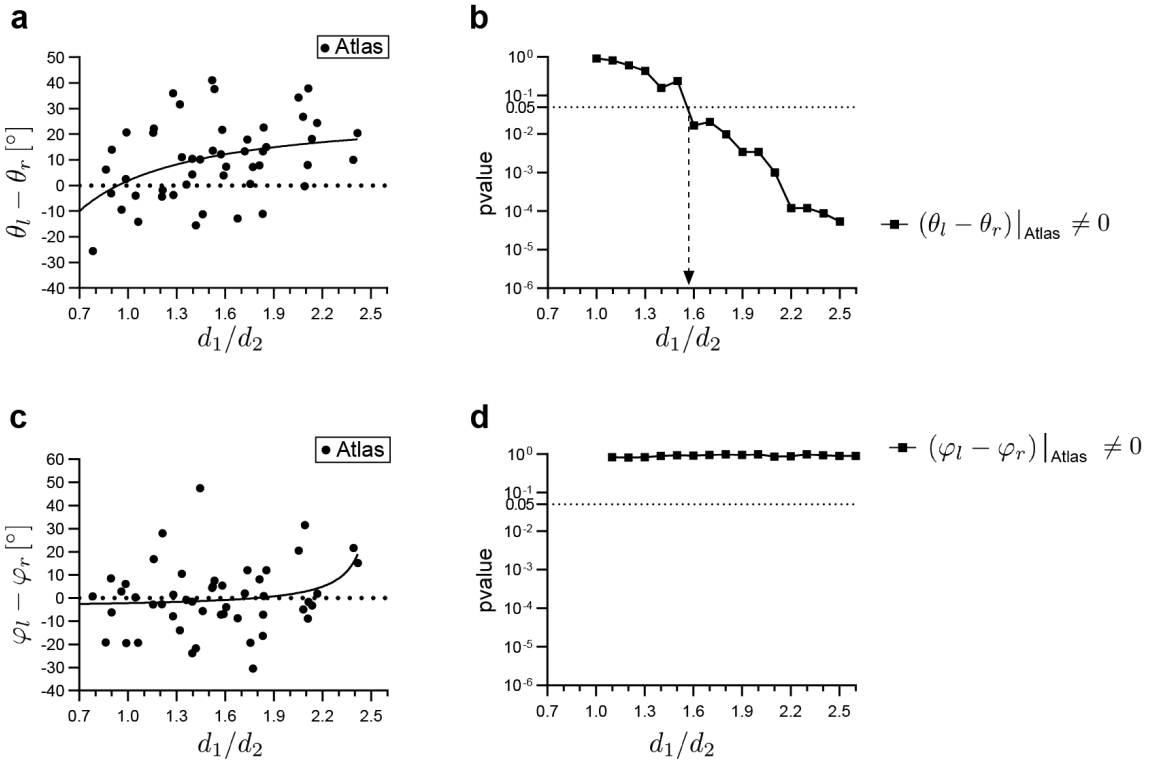

Figure 4.30 | **Onset of left–right morphological asymmetry before heart looping. a**, Plot showing the evolution of the θ angles depending on the d_1/d_2 value. Curves represent Padé approximant of all the points. **b**, Evolution of p-values as a function of d_1/d_2 for the deviation of the θ angle from left–right symmetry and for the comparisons between experimental groups, as indicated. A mixed linear model was applied to estimate the asymmetry between both sides at different stages (fixed effects) adjusting by the angle with two-sided P value calculation and applying Sidak's correction for multiple tests. **c**, Equivalent to panel **a**, for φ angle. **d**, Equivalent to panel **b**, for φ angle.

Related to the different angle of insertion of the IFTs, we frequently observed that the insertion of the right IFT into the ventricular region forms an acute angle, whereas the similar position on the left side is characterized by a much smoother transition, often even accompanied by a small bulge connecting the IFT to the ventricle (Figure 4.31). In hearts at the looping stage, these asymmetric connections seem to favor the typical rightward ventricular displacement during looping (see the group 9 representative in Figure 4.31), as the right-side acute angle may act as a hinge, favoring rotation toward the right side, while the bulge on the left side may oppose a similar rotation toward the left side.

We concluded that before heart looping is obvious, and starting at linear HT stages, left–right morphological asymmetry builds up in the IFT region, manifested in the different angles of insertion of the IFTs.

4.9 NODAL CONTROLS EARLY CARDIAC LEFT–RIGHT ASYMMETRY

To study whether early IFT asymmetry is under the control of the genetic pathway that controls left–right specification in the mammalian embryo, we studied this feature in *Nodal* mutants, which show randomized looping direction [118, 148]. For this, we studied

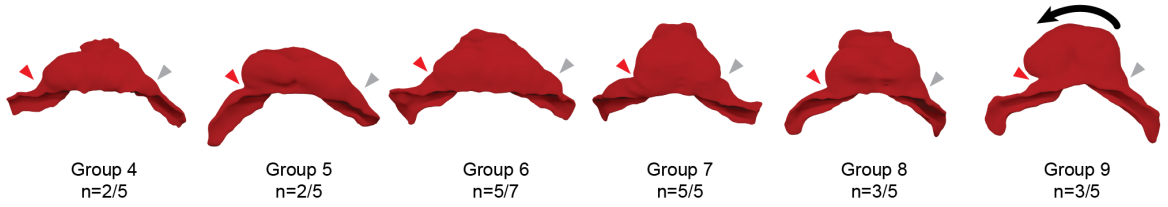

Figure 4.31 | **Acute angle versus smooth transition in the IFT insertion angle.** Specific wild-type hearts from different groups, highlighting the acute angle between the right IFT insertion and the ventricle (red arrow) and the smooth transition on the opposite side (gray arrow), often characterized by a small bulge. The black arrow illustrates the direction of looping. n, number of specimens showing this feature over the total number of specimens in each staging group.

a collection of 3D images from *Nodal* mutants and their control siblings acquired in the laboratory of a collaborator: Sigolène M. Meilhac (IMAGINE Institute, Paris) (see Figure 4.32 and section 3.4). Then, we segmented and reconstructed in 3D all the shapes. After this, we calculated d_1/d_2 for each of the specimens.

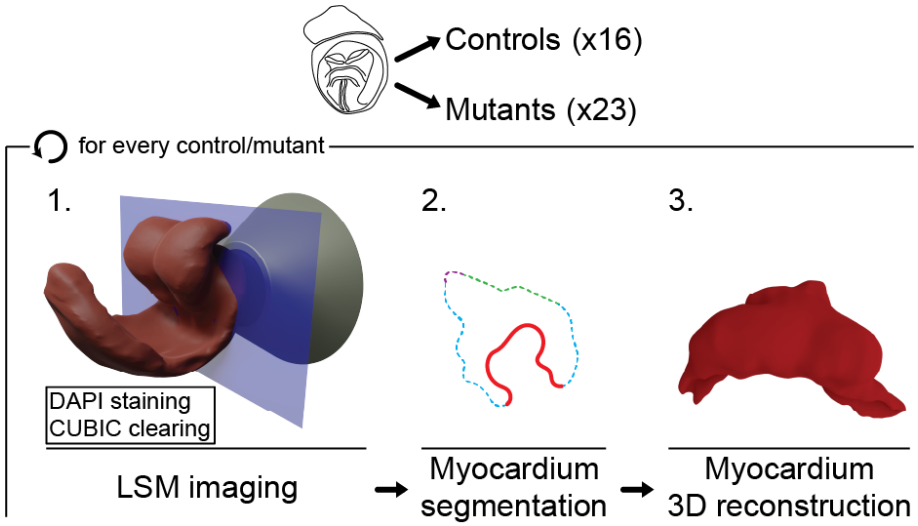

Figure 4.32 | ***Nodal* control and mutants acquired in SMM's lab.** Nodal specimens (16 controls and 23 mutants), labelled with DAPI, have been imaged using LSM (step 1). After this, embryos have been segmented and reconstructred in 3D in MT's lab (steps 1 and 2).

First, we determined that the staging systems described here were transferable between labs, despite the different imaging methods and genetic backgrounds (see section 4.10 for more details). With this, using the d_1/d_2, we could distribute the specimens along the developmental spectrum measured by such parameter (Figure 4.33).

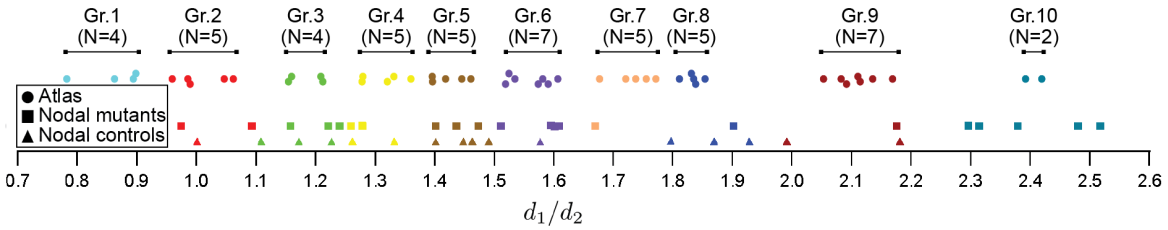

Figure 4.33 | **Mapping of the d_1/d_2 values measured in SMM's control specimen collection.** The *Nodal* controls are distributed quite uniformly between d_1/d_2 ϵ $[1.0 - 2.8]$. and mutants are distributed along values d_1/d_2 ϵ $[0.98 - 2.52]$.

We next calculated the θ and φ angles of the *Nodal* control and mutant collection (see Figure 3.21). Regarding the θ angle, we found progressive asymmetry similar to that observed in the original collection (Figure 4.34a, green dots and curve). Regarding the φ angle, we found the same symmetric behavior (Figure 4.34c), green dots and curve). We also checked that the difference in θ and φ angle between the *Atlas* and *Nodal* control collections was not significant, thus confirming the same natural tendency in both cases (Figure 4.34b, Figure 4.34d and blue lines).

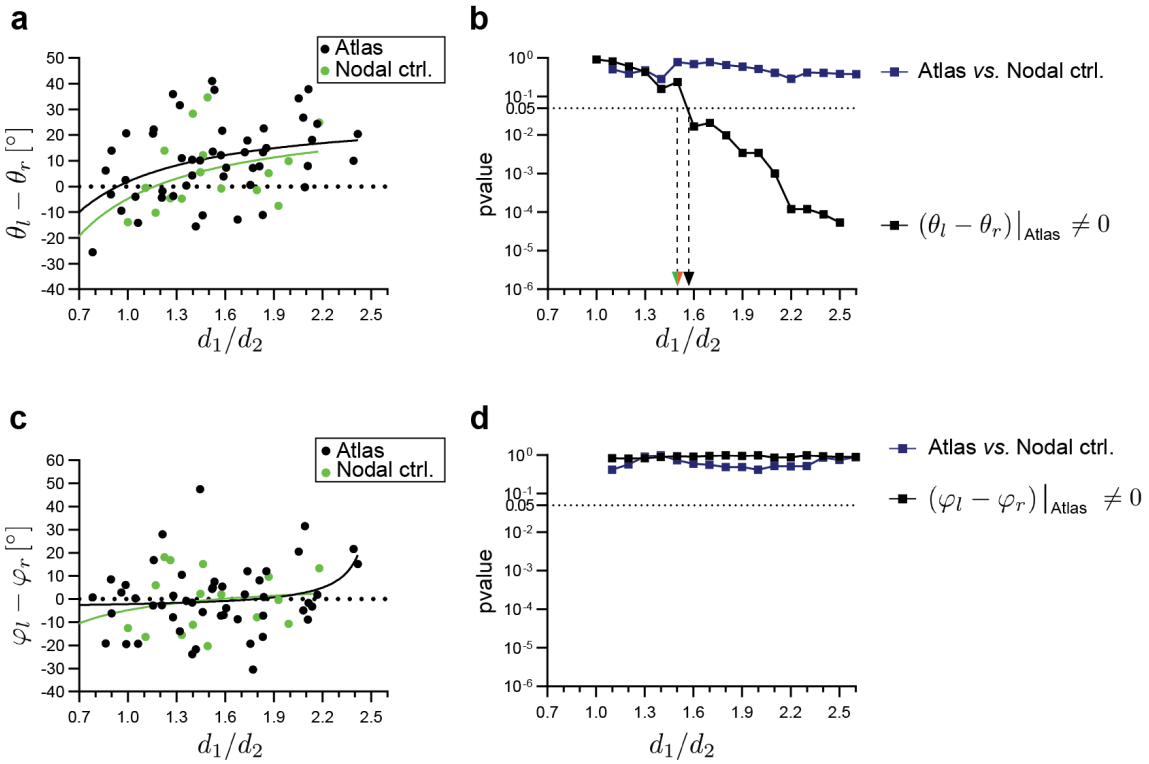

Figure 4.34 | **Left-right asymmetry including *Nodal* controls. a**, Green curve shows the evolution of θ angle adjusted by Padé approximants. **b**, Blue curve refers to the difference on θ when comparing *Atlas* and *Nodal* controls specimens. **c**, Equivalent to panel **a**, for φ angle. **d**, Equivalent to panel **b**, for φ angle.

Examining the independent evolution of the left and right θ angles in both control embryo collections showed that both tend to diminish with time (Figure 4.30a), but the right one does it at a higher pace than the left one, which produces the progressive asymmetry (Figure 4.30b).

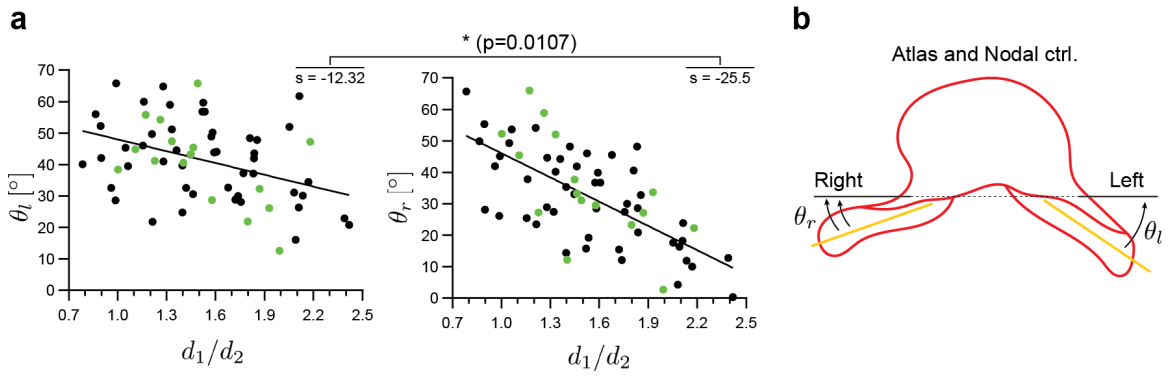

Figure 4.35 | **IFT angles for *Atlas* and *Nodal* collection. a**, Separated values of θ_l and θ_r for the two groups of control specimens. Analysis of covariance has been applied to test whether slopes are significantly different calculating two-tailed P values. **b**, Separated values of θ_l and θ_r for the *Nodal* mutant specimens. **b**, Schematic representation of the different evolution of θ_l and θ_r angles in wild-type embryos. s, slope.

We then studied conditional *Nodal* mutants (*Hoxb1*$^{Cre/+}$; *Nodal*$^{flox/Nul}$) using similar procedures. *Hoxb1*^{Cre} introduces the Nodal mutation specifically in the cardiac precursor cells of the IFTs and surrounding paraxial mesoderm (PM) [118]. *Nodal* mutants also showed IFT θ angle-specific progressive asymmetry; however, the direction of the asymmetry was reversed with respect to that in control groups (Figure 4.36a). While in controls, the left–right θ angle evolves from zero toward positive values, in *Nodal* mutants, the values evolve from zero toward negative values.

Regarding the θ angle, Figure 4.36b shows that the evolution of this angle for the *Atlas* and the *Nodal* mutants becomes significantly different from a given value of d_1/d_2 (green curve). The same occurs when comparing *Nodal* controls and *Nodal* mutants (orange curve). Both these events take place at $d_1/d_2 \approx 1.55$. Regarding the φ angle, we found no significant difference in all the aforementioned comparissons.

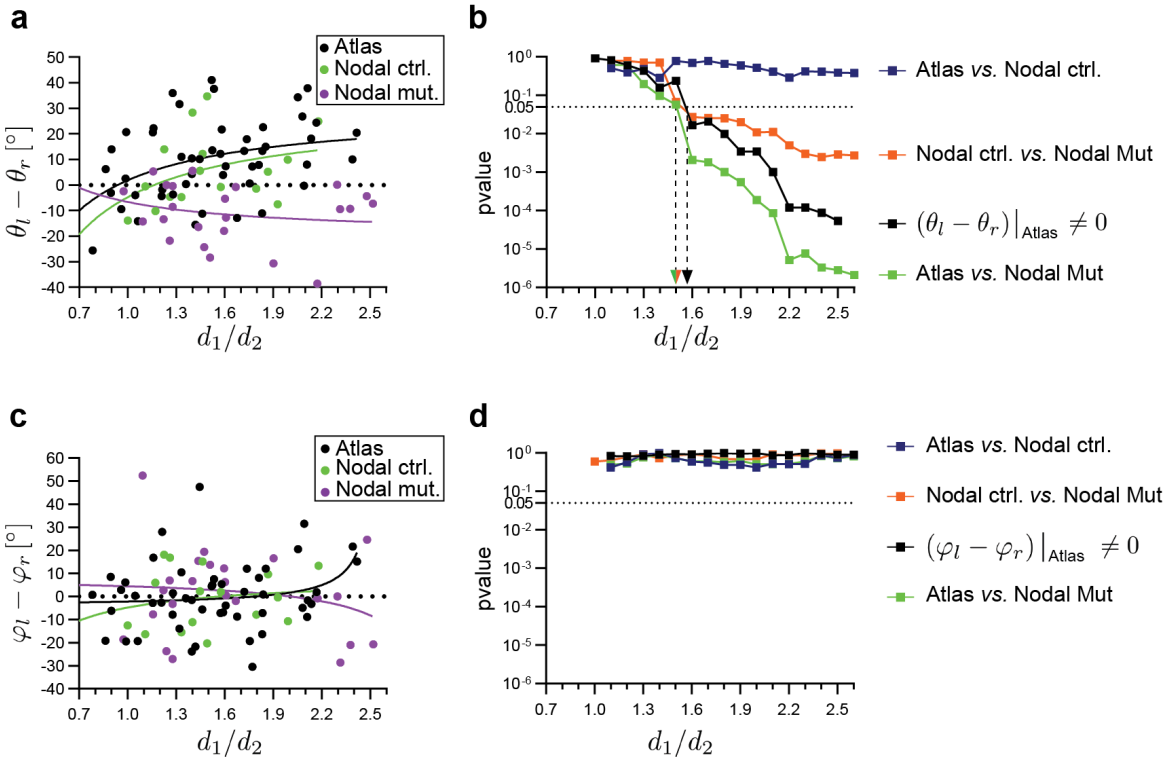

Figure 4.36 | **Left-right asymmetry including *Nodal* mutants. a**, Purple curve shows the evolution of θ angle adjusted by Padé approximants. **b**, Green curve refers to the difference on θ when comparing *Atlas* and *Nodal* mutant specimens. Orange curve refers to the difference on θ when comparing *Nodal* control and *Nodal* mutant specimens. **c**, Equivalent to panel **a**, for φ angle. **d**, Equivalent to panel **b**, for φ angle.

When looking at the separate values of the θ angles, we observeb no faster reduction of the θ right angle compared to the left one, but rather a non-significant tendency of the left θ angle to reduce at a higher pace than on the right θ in the mutants (Figure 4.37b).

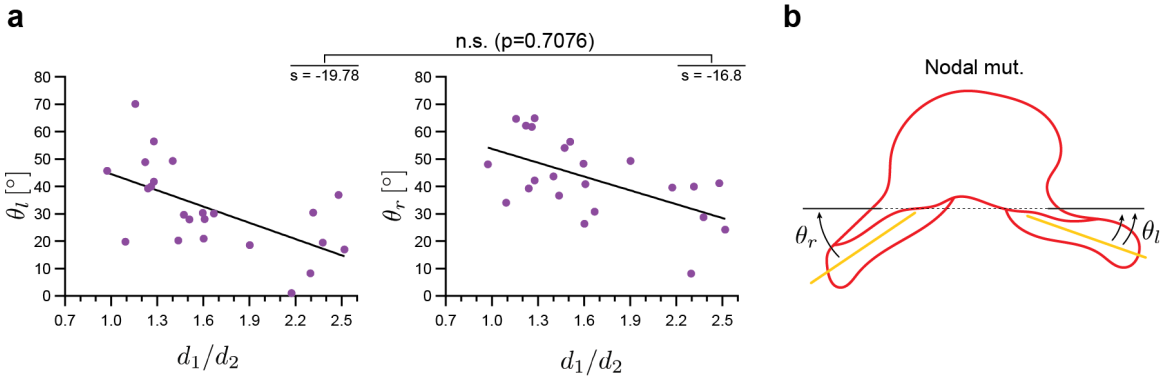

Figure 4.37 | IFT **angles for *Atlas* and *Nodal* collection. a**, Separated values of θ_l and θ_r for the two groups of control specimens. Analysis of covariance has been applied to test whether slopes are significantly different calculating two-tailed P values. **b**, Separated values of θ_l and θ_r for the *Nodal* mutant specimens. **b**, Schematic representation of the different evolution of θ_l and θ_r angles in wild-type embryos.

Our results show that early IFT asymmetry is related to heart looping, both in normal development and in mutants, affecting left–right specification.

In order to study the applicability of the proposed staging system across different labs, we correlated the values obtained for the h/w parameter. Although our best performing staging parameters was d_1/d_2 (Figure 4.16), we decided to use h/w because it is easier to measure, and it is necessary to only label the embryos with DAPI. Besides, we found a very high correlation between both of them (Figure 4.18), thus making them perfectly interchangeable for staging purposes.

To do so, we analyzed the relation between the measures obtained in Sigolène M. Meilhac's lab (SMM) and ours. We obtained a high correlation, indicating that different our observations lead to similar measurements from differently treated images (Figure 4.38). Therefore, we could assign SMM's specimens to a staging group with confidence (Figure 4.33).

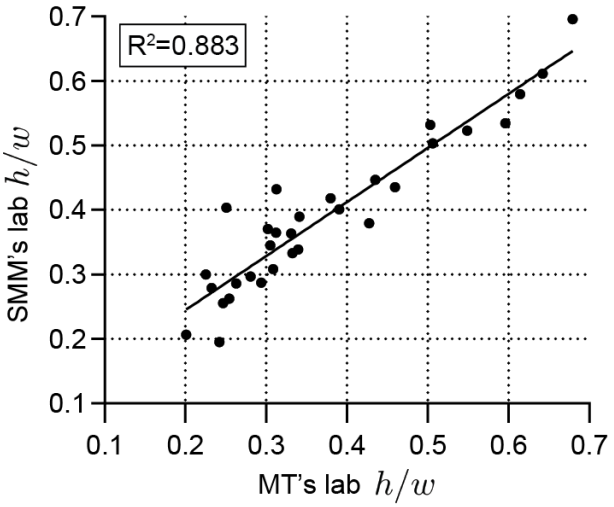

Figure 4.38 | **High staging correlation using the same parameter in two different labs.** Plot shows the values of the h/w values measured for different *Nodal* specimens (controls and mutants) at SMM and MT's labs. A total of 31 specimens from the collection were chosen randonmly.

In addition, we validated the stages estimated for the SMM embryos. We were able to prove that h/w, although a simple parameter, performs as well as using direct morphological comparisons for staging, i.e.: assigning a staging group to a SMM specimen by looking for its closest into the atlas.

In order to do this, we first calculated d_1/d_2 (results are in Figure 4.33) for each of the *Nodal* control specimens (x_l shape in Figure 4.39, part 1). We called this the *measured* d_1/d_2 value ($(d_1/d_2)'$, Figure 4.39a, part 1 and x-axis in Figure 4.39b). Then, we took the MSG which d_1/d_2 value was closest to d_1/d_2', plus the two earlier and later MSGs in the temporal sequence and computed surface maps from x_l to them (Figure 4.39a, part 2). We used the latter to calculate the morphological distance, (D, more detailes in section 3.17) between x_l and the others. The representation of the inverse of these distances (dependent variable) as function of the d_1/d_2 values of the MSGs (independent variable) were fitted to a gaussian curve (Figure 4.39a, part 2). The d_1/d_2 value corresponding to the peak of the bell (red dot in Figure 4.39a, part 2) is identified as the *predicted* d_1/d_2 value $(d_1/d_2)^\star$, for the x_l specimen (y-axis in Figure 4.39b).

In this way, we compared for each specimen of the control SMM collection the directly measured d_1/d_2 parameter (Figure 4.39a, part 1) to the d_1/d_2 parameter estimated from the matching of the specimen morphology along the MSG sequence. This comparison resulted in a very high linear correlation between the measured (Figure 4.39a, part 1), and the predicted d_1/d_2 values: (Figure 4.39b, part 2). This shows that the d_1/d_2 parameter and its close surrogate h/w can be used to stage collections of embryos of different genetic backgrounds and imaged/measured by different methods and laboratories. We didn't include the *Nodal* mutants in this study because heart morphology is altered, and therefore this validation, based on morpholigical similarity, would lead to wrong conclusions.

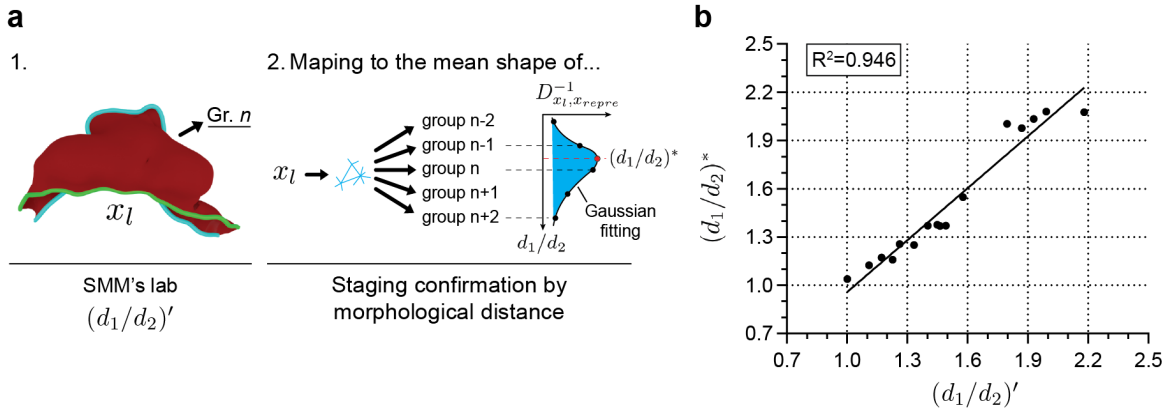

Figure 4.39 | **Validation of staging system using morphological criteria. a**, Procedure for the morphological mapping of the SMM's control specimen collection to the atlas MSG collection. **b**, Correlation between the measured d_1/d_2: $(d_1/d_2)'$ parameter, and the predicted d_1/d_2: $(d_1/d_2)^\star$, obtained from the morphological mapping of the SMM's control specimen collection to the atlas MSG collection.

4.11 EARLY LEFT–RIGHT ASYMMETRY AFFECTS PERICARDIAL TISSUES

To investigate whether and how the left–right asymmetries detected in the heart tube affect the pericardial tissues, we extended our study to the pericardial mesoderm (PMes) and the endoderm (END). To perform this study, we first defined the shape of the PMes by subtracting the MYO shape from the PC shape (see Figure 4.40a). Then, we estimated the mid–sagittal plane of the embryo (see Figure 4.40b and section 3.13). We used this to cut the PM in two halves and then flipping one onto the other and doing a rigid registration (see Figure 4.40c). With this, we performed a surface map between both halves, and used this to quantify the local deformation required for a perfect match of the geometries, thus determining the morphological asymmetry between both sides (this deformation is color-coded on top of the shapes shown in Figure 4.40b).

This study identified asymmetry of the lateral–posterior extensions of the pericardial cavity in which the IFTs are encased. A visualization of the fitting between the right side of the pericardial mesoderm and the flipped left side in the RSG collection

suggested a systematic positioning of the left side closer to the midline plane in groups 6+ (Figure 4.40c). This was confirmed in a morphometric analysis of the whole specimen collection (Figure 4.40d). This left–right deviation coincides with the direction of the progressive asymmetry of the θ angle detected in the IFTs.

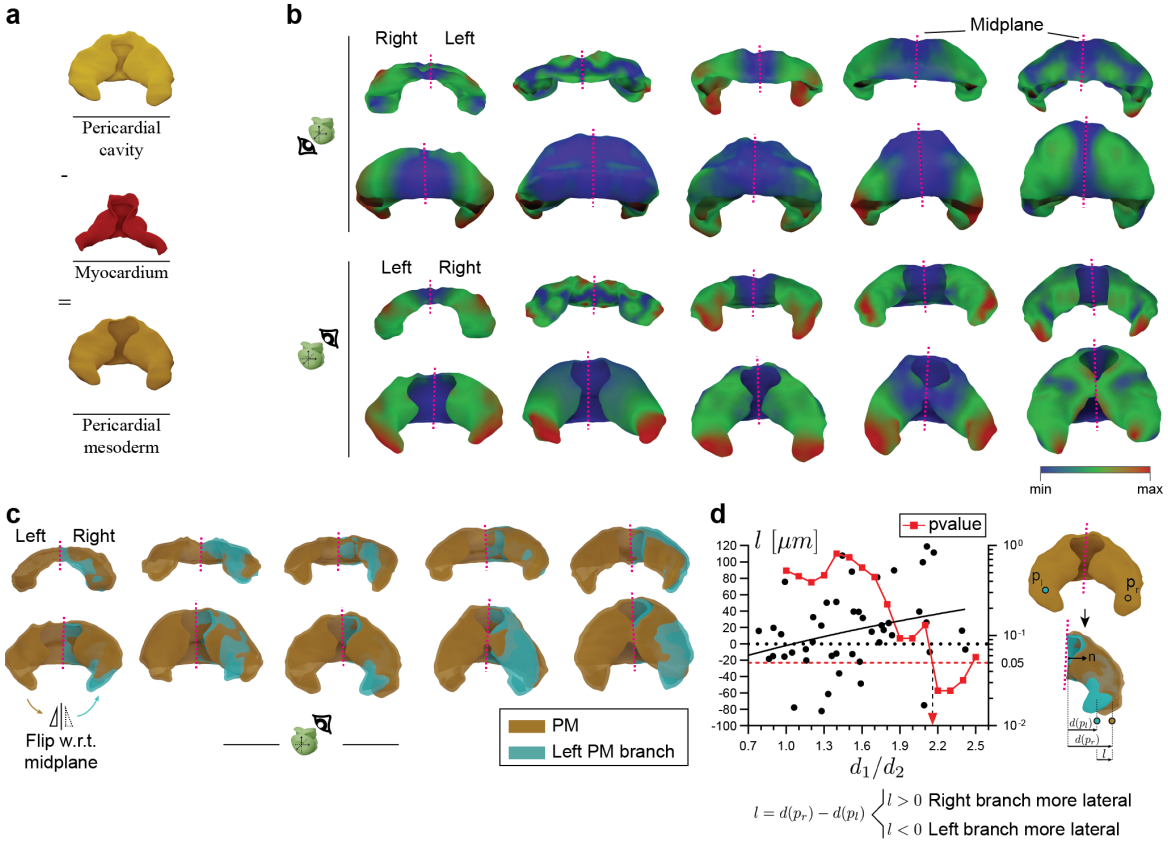

Figure 4.40 | **Signs of early asymmetry in the pericardial mesoderm. a**, Reconstruction of the pericardial mesoderm. **b**, Maps of local deformation distribution resulting from mapping left and right sides of the pericardial mesoderm to each other. Specimens shown are the RSGs from ventral and dorsal views. Dotted magenta line indicates the midplane intersection. The color coding corresponds to the relative levels of morphological variation within each specimen. **c**, Ventral view of the pericardial mesoderm of RSGs (orange), including the view of the left side flipped with respect to the midplane onto the right side. **d**, Plot shows the characterization of the misalignment between the two sides of the pericardial mesoderm. A mixed linear model was applied to estimate the asymmetry between both sides at different stages (fixed effects) adjusted by the l distance with two-sided p-value calculation. Black curves represent Padé approximant of all the points. The schemes on the right show how the l distance was determined.

In the END, we observed a deformation of the ventral FGE in correlation with the displacement of the SPL layer during dorsal closure (Figure 4.41a). In early specimens, this deformation has the form of two bilateral ridges that coalesce into one, as the two SPL sides reach the midline (Figure 4.41b). From RSG7+, this ridge shows a deviation from the midline such that its anterior side displaces rightward, and its posterior side displaces leftward. This displacement is concomitant with a similar tilting of the closing borders of the splanchnic mesoderm, which produces an asymmetric mesocardium, as previously described [149]. The observations are compatible with the deformation of the endoderm due to the movement of the splanchnic mesoderm over its ventral surface.

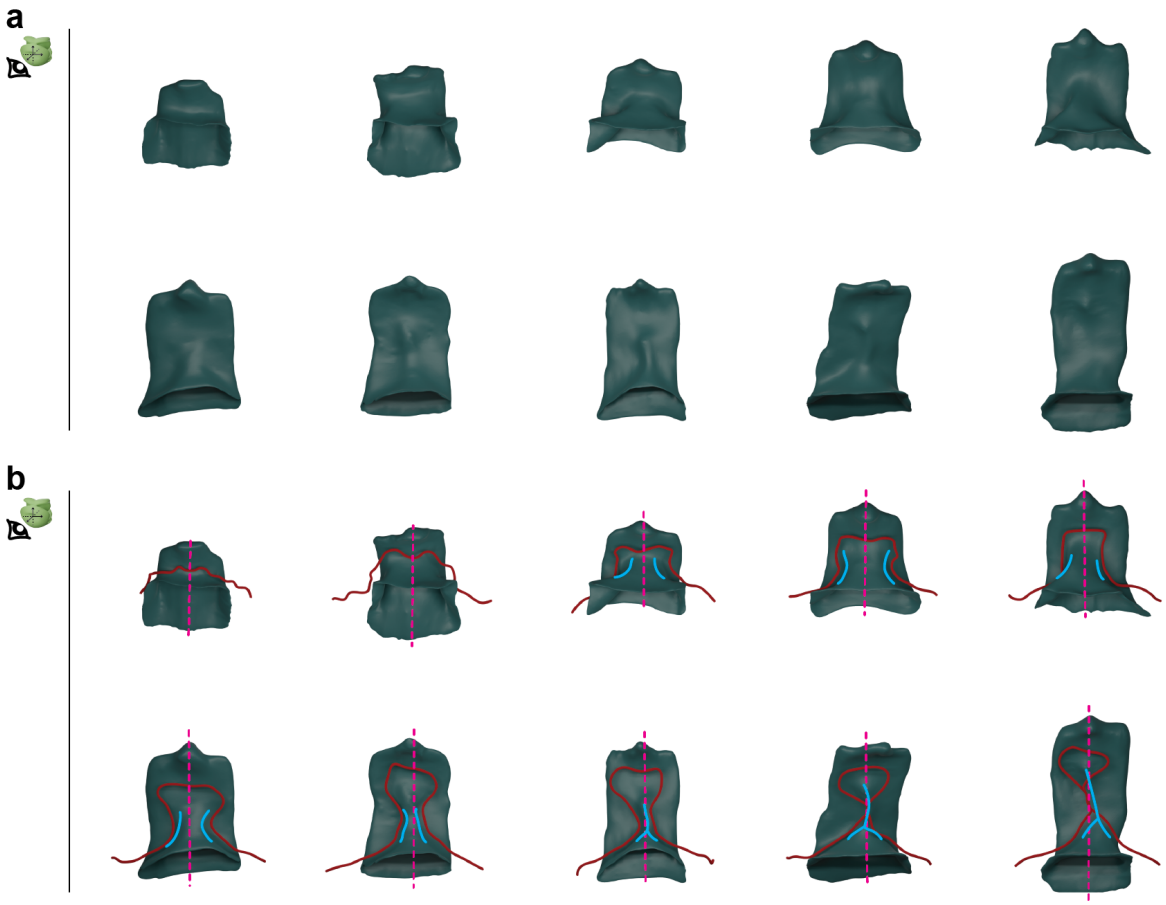

Figure 4.41 | **Early asymmetry in the foregut pocket endoderm. a**, Ventral view of the foregut pocket endoderm in the RSGs. **b**, A similar representation of the foreguts in **a**, indicating the midplane intersection (pink dotted lines), the ridges detected, first bilateral and later fused medially (blue), and the d1 line, at the border between the MYO and the SPL (red).

4.12 A DYNAMIC ATLAS OF EMBRYONIC HEART

To simulate temporal evolution through the stages characterized, we used the 10 MSG shapes generated plus specimen 51 (Figure 4.26 and Figure A.4) and the method described in [103] to generate a smooth temporal transformation between stages (Figure 4.42). To achieve this, we propagated a common mesh connectivity, identifying equivalent vertices from the first to the last shape (section 3.18).

Once the same mesh connectivity is set on all the MSGs, they were rigidly aligned to the first mesh (t_1). In addition, in order to provide a more accurate alignment, a second alignment step was taken using the landmarks to register equivalent regions across stages. We then applied an interpolation technique (section 3.18) to estimate the positions of each vertex between consecutive MSG so that transitions between positions take place smoothly (Figure 4.42c) and inserted 30 interpolated shapes between each MSG.

This approach generated a dense temporal sequence of 3D meshes of heart tube morphogenesis (Supplementary Video 1 in [17]). The model generated does not represent

the evolution of a concrete specimen, but a most probable trajectory of the morphology of the forming heart tube based on averaging the shapes of several hearts at each developmental time.

This approach did not allow us to include the models of the rest of tissues associated with the forming heart tube because mismatches are generated at the limits between the MSGs of the different tissues. To generate a dynamic model that includes all the tissues, we then used the collection of 10 RSGs (Figure 4.42b and Supplementary Videos 2–7 in [17]). Given that these are specific specimens, their matching to the surrounding tissues is improved. This model represents a possible evolution of the morphology of the heart tube and its associated tissues based on different specimens that represent consecutive stages of heart development. Examples of the interpolated tissues are provided in Figure 4.42b.

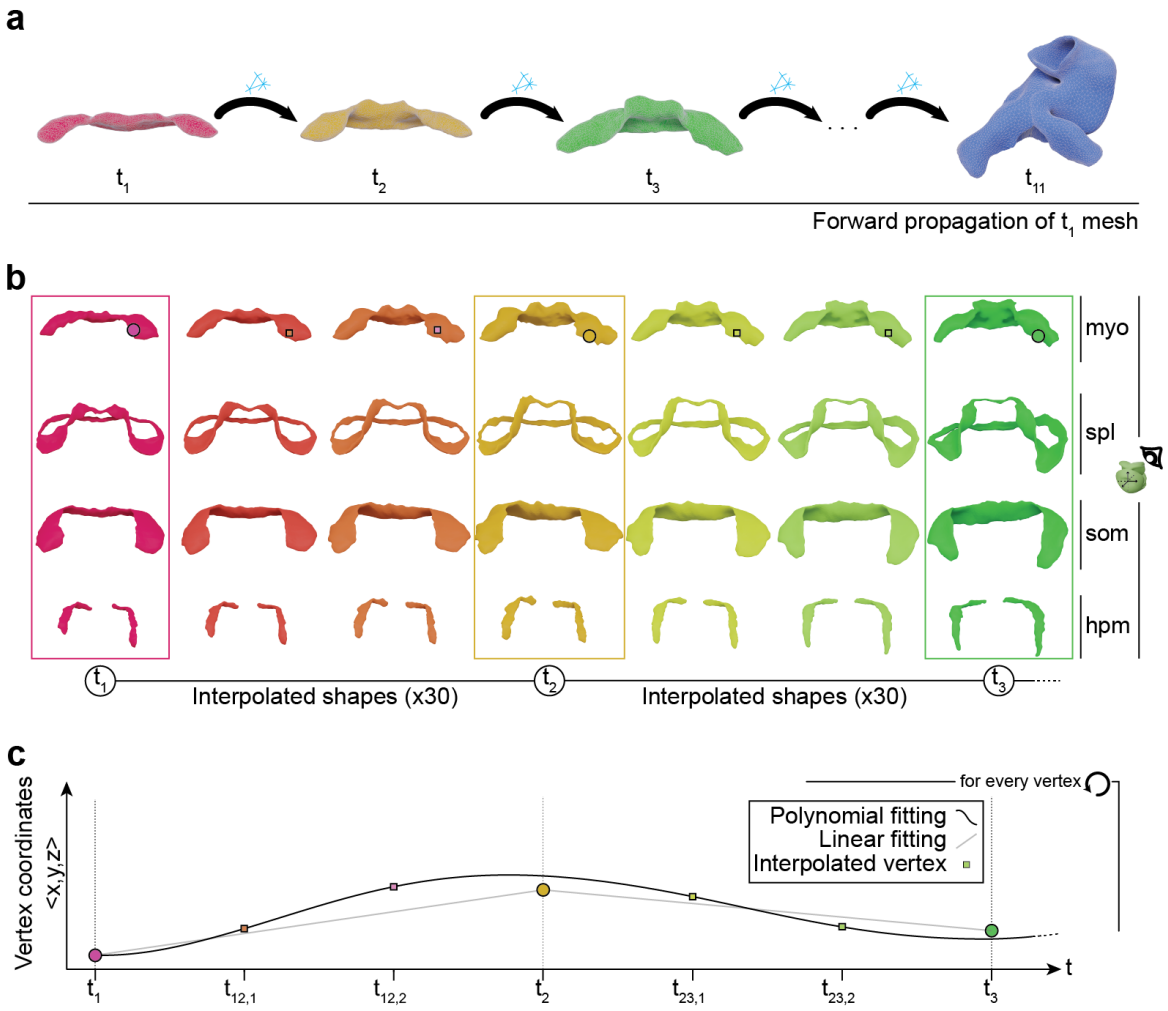

Figure 4.42 | **Dynamic meshes defining the full spatio-temporal domain of heart tube morphogenesis. a**, Elaboration of a continuous sequence using the MSG shapes. The process starts by mapping the mesh connectivity from the first time point to the next shape. This process is repeated until the connectivity of the first mesh is propagated until the final mesh at t10. This process can also be applied using the RSG shapes. **b**, Concept of shape interpolation applied to the three first time points of the RSG shapes. Each row shows the result for the different tissues forming the pericardial cavity. The dots depicted on top of the myocardium shape illustrate the position of a single vertex traveling through the shapes as morphogenesis progresses. **c**, The plot illustrates the estimated trajectory of the vertex highlighted in **b**. Rounded points represent the actual position of the same vertex in every timepoint. Square symbols represent the dynamic position of the vertex at intermediate points, resulting from the non-lineaer interpolation. MYO, myocardium; SPL, splanchnic mesoderm; SOM, somatic mesoderm; HPM, head paraxial mesoderm.

Finally, we correlated previously described stages of heart tube development and several morphological and functional landmarks of cardiac development to the evolution of d_1/d_2 (Figure 4.43) and incorporated this information to the videos of the four-dimensional models (Supplementary Videos 2–7 in [17]).

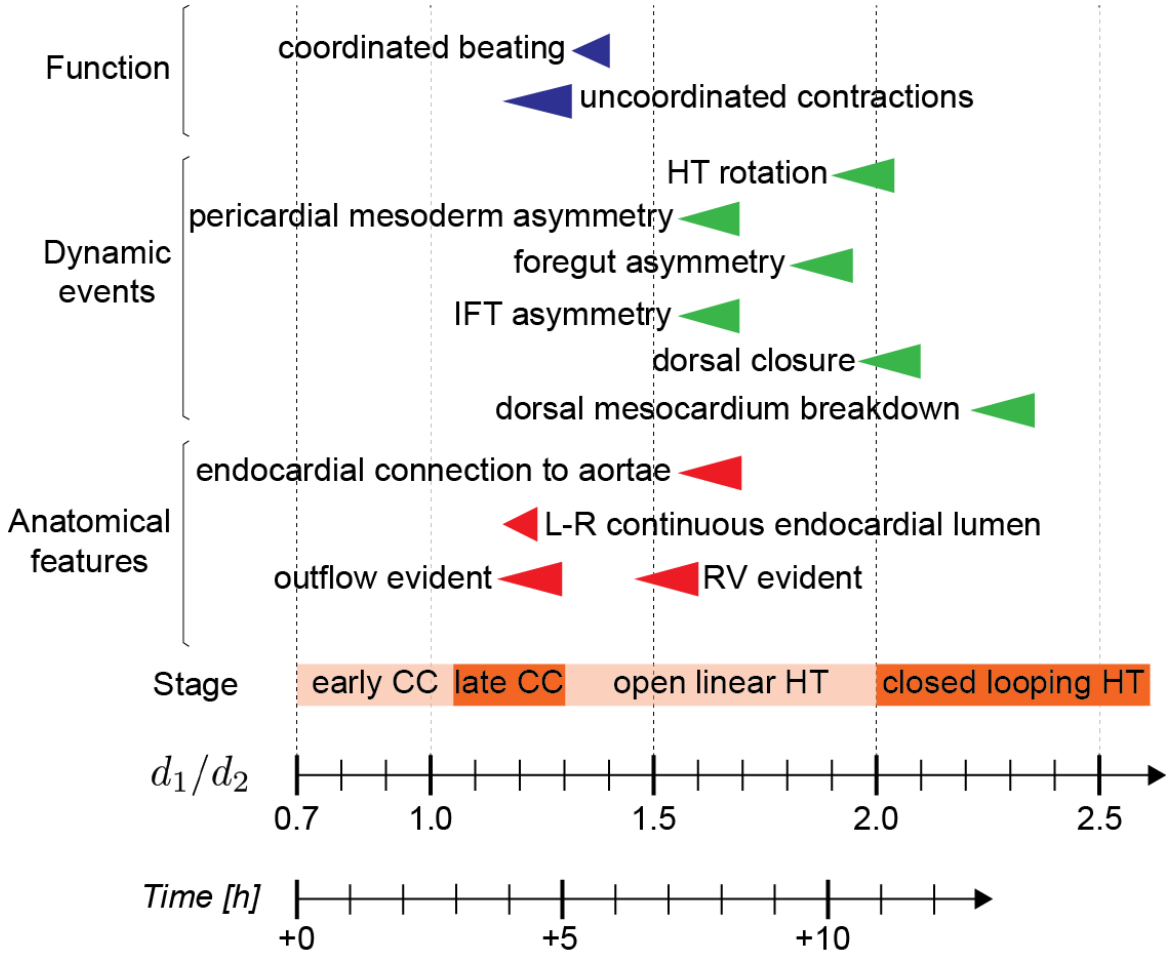

Figure 4.43 | **Major dynamic events.** Temporal reference for morphological and physiological events during heart tube formation. Data on the onset of contraction/beating and real-time scale were obtained from in vitro live-imaging videos [5]; HT, heart tube; RV, right ventricle.

5

DISCUSSION

In this thesis, we have generated a comprehensive, dynamic and realistic representation of cardiac tissues during primitive heart tube formation in the mammalian embryo. We have elaborated a dataset[1] of confocal images that we have used to segment tissue-scale morphological aspects. These images, at subcellular resolution, show clearly distinguishable membrane and nuclei morphology. This opens the door to explore cellular aspects during heart morphogenesis such as proliferation, anisotropy or orientation. These properties could be represented in the atlas of this thesis and used for classification purposes in order to distinguish new cellular groups during heart development. Besides, features such as cell size, shape, number and position are affected by mechanical forces during development [150]. This opens the door to investigate mechanical aspects that could help to elucidate the forces that shape the heart. This analysis can be enriched by addition of external data from different labs.

In the process of generating a unified dynamic model using information from a collection of specimens, we faced the problem of morphological variability during early cardiogenesis, which represented limitations to describing 'normal' development. We thus developed strategies to describe 'most likely' geometries for each developmental stage. To achieve this, we first developed a morphometric staging method independent of subjective appreciation of specimens, thereby improving the current state of the art in the field [5, 146, 149]. Unsupervised clustering and assessment of parameters that measure the quality of classifications identified a simple ratio d_1/d_2 as the best staging parameter. While we used this parameter to group specimens in relation to their developmental progression, and this was essential to map variability and generation of the 3D+t model, the great advantage of using d_1/d_2 is that it allows for the assignment of specimens along a continuum of heart tube morphogenesis. We think this staging method will be of utility in the precise definition of cardiac developmental timing when comparing 3D data between different laboratories. Furthermore, we identified simpler measurements, like the height-to-width ratio (h/w), as very highly correlated with d_1/d_2 and accessible to all labs and 2D–3D imaging approaches.

Ten groups were established according to the variation of d_1/d_2, which allowed for the statistical analysis of morphology within groups. The use of a recently developed method [103] for computing surface maps allowed the definition of mean shapes and the application of statistical analyses to each vertex, thereby generating maps of local variability. We propose that this approach is of high value when describing mammalian organogenesis because it simultaneously provides information about the 'average' geometry

1 https://doi.org/10.17867/10000174

of a developing organ and about the regions that are more likely to vary from specimen to specimen.

Within the context of the shape analysis performed in this thesis, we initially used solid spherical harmonic (SSH) [151] as a shape descriptor for our heart morphologies (see Figure A.8). This approach converts a shape into a finite number of coefficients (up to some degree of detail, see Figure A.8c), which are an abstract representation of the shape. With this, we tackled the problem of inferring the intermediate shapes that transform a shape into another. We did this by linearly interpolating the coefficients between both shapes, and used them to reconstruct intermediate forms. However, we found that this approach was not valid for heart tube morphogenesis. This is so because the interpretation of the coincident morphological phenomena (growth, folding and deformation) transforming the early heart, have non-trivial interpretation in the coefficient space. Therefore, linear interpolation leads to unrealistic intermediate shapes, lacking continuity and crammed of artifacts.

In [152], the authors have applied this approach to create a continuous atlas for limb development (from E10 to E12.5). However, the adequate intermediate reconstructions may be explained by that fact that the limb represents a very amenable subject for this approach: it has a rather simple shape, and its development can be mainly characterized by growth along one single direction (radial), with minor or null folding and/or deformation events. Therefore, linear interpolation of SSH coefficients can manage better under such circumstances. However, the authors showed in the same work the application of the same approach to mouse embryonic hearts (from 10 to 29 somites), aiming to describe the external surface, excluding inner details. They obtained a continuous representation of heart development in which, although general growth is good captured, transitions between shapes do not depict the process well. Therefore, throughout the development of this thesis we have learned that SSH, when applied to this problem, must be considered with caution. For this reason, we opted for methodologies that have an actual *notion* of the surface of the shapes [103], which guarantees smooth and continuous transformations.

Failures in early steps of cardiac development can lead to misalignment of the chambers and great vessels or to different types to left–right cardiac mispatterning. In particular, we identified strong variability at the dorsal borders of the myocardium. These dorsal borders, initially placed laterally, end up fusing at the midline, forming the dorsal mesocardium, which later disappears during looping. Important mechanical roles have been proposed for the mesocardium during looping [149], and the mesocardial myocardium later localizes to the inner curvature of the looping heart, which plays essential roles in the alignment of the cardiac chambers and the great arteries (reviewed in [153]). The finding of high variability in this region, therefore, could be related to the onset of malformations associated with the mesocardial/inner curvature morphogenesis. Other regions of high variability were the IFTs, which correlate with the highly dynamic and transient nature of

these structures. Finally, apical regions of the future left ventricle also show high variability, possibly associated with asynchrony of the ballooning process [154] between specimens.

Our approach also allowed us to study the left–right symmetry of the forming heart tube. Heart tube looping is considered as the earliest morphological evidence of organ left–right patterning in the embryo. In particular, cardiac left–right patterning defects are commonly associated with impairing congenital heart disease, also in humans. Here, we describe an aspect of left–right asymmetry in the forming heart affecting IFTs and preceding heart looping. The influence of the IFT region in heart looping has been previously proposed, mainly through the exertion of asymmetric forces from the left and right sides of the venous pole, provoked by differences in cytoskeletal contraction, cell migration and/or proliferation [155–157]. We therefore identified the earliest signs of morphological asymmetry in the mouse embryo localized to the IFTs of the forming heart. This asymmetry precedes looping and is likely to affect this process, as any active or reactive force exerted by/on structures oriented in different angles is predicted to produce asymmetric forces. In agreement with this view, Nodal mutants, which show a high incidence of heart looping defects, show reversed asymmetry of the IFT insertion angles. Nonetheless, there is no strict relationship between IFT insertion angles and the looping direction; only 50% of Nodal mutants show reversed direction of looping [118, 148] while some WT specimens show negative left–right θ angles during normal looping. We therefore propose that left–right bias in the orientation of the IFTs depends on the general left–right patterning mechanisms of the embryo and imposes an architectural bias to the forces that determine heart looping direction in interaction with additional determinants. Interestingly, we also found left–right alteration of the pericardial cavity and endoderm, suggesting that the process of heart looping involves a wider asymmetry also affecting the peripheral tissues. Our observations on the relationship between splanchnic mesoderm movements and ventral foregut deformation strongly suggest that the splanchnic mesoderm has an active role in generating left–right asymmetries in the pericardial cavity. In this respect, the described transient expression of Nodal in the left splanchnic mesoderm and its influence on cell proliferation and matrix remodeling [118] might represent an important factor in the generation of left–right asymmetry in the pericardial cavity.

The dynamic models generated here represent a highly detailed atlas of the different tissues involved in primitive cardiac tube formation. This atlas will be useful for the combination of relevant biological information produced from different experiments or labs into a unique spatial representation. This opens the door for establishing a common space where scientists can share analyses on quantitative aspects representable in the spatio-temporal domain, for example, gene expression patterns. Furthermore, the atlas generated is embedded in a statistical framework that accounts for natural variability, which can be used as a reference for analysis of mutant embryos, either at global or local scales.

Deep understanding of morphogenesis involves identification of the sources and the temporal and spatial distribution of forces that shape developing tissues. Predictive modeling is ultimately required to fully acquire this knowledge [118, 158]; however, it critically relies on access to realistic dynamic models of the geometry of the tissues/organs under study [32]. The dynamic model developed here will be useful for the development of finite-element studies that explain the forces that drive cardiac tube formation, one of the most complex morphogenetic processes in the mammalian embryo, which underlies the high incidence of cardiac malformation in newborns.

6

CONCLUSIONS

1 We have elaborated a high-resolution dataset of 52 E7.5-E8.5 mouse specimens at sub-cellular resolution, that cover the whole cardiogenic area.

2 We have precisely segmented the forming heart, and all the tissues forming the anterior celomic cavity.

3 We have segmented the morphology of the forming circulatory system (aortic lumen and endocardial lumen) and the shape of the foregut endoderm.

4 We have elaborated a novel staging system based on morphometry for the early mouse embryo (E7.5-E8.5), and we have proven that it is widely applicable by different labs.

5 We have tackled the morphological variability inherent to the process of heart tube formation and defined the regions that present highest levels of variability.

6 We have created a continuous, 3D+t, atlas of the "most likely" tissue morphogenesis process forming the heart tube, by integrating the information from the whole dataset.

7 From the heart tube continuous atlas, we have found specific specimens of the collection that best recapitulate each stage group defined, and used this to define a 3D+t description of all the tissues forming the anterior celomic cavity.

8 We have found a new, and the earliest so far described, left-right asymmetry in heart development.

BIBLIOGRAPHY

[1] S. M. Meilhac and M. E. Buckingham, "The deployment of cell lineages that form the mammalian heart", *Nature Reviews Cardiology*, vol. 15, no. 11, pp. 705–724, 2018. DOI: 10.1038/s41569-018-0086-9.

[2] K. D. Prummel, S. Nieuwenhuize, and C. Mosimann, "The lateral plate mesoderm", *Development*, vol. 147, no. 12, dev175059, 2020. DOI: 10.1242/dev.175059.

[3] W. P. Devine, J. D. Wythe, M. George, K. Koshiba-Takeuchi, and B. G. Bruneau, "Early patterning and specification of cardiac progenitors in gastrulating mesoderm", *eLife*, vol. 3, M. E. Bronner, Ed., e03848, 2014, ISSN: 2050-084X. DOI: 10.7554/eLife.03848.

[4] F. Lescroart *et al.*, "Early lineage restriction in temporally distinct populations of mesp1 progenitors during mammalian heart development", *Nature Cell Biology*, vol. 16, pp. 829–840, 9 Sep. 2014, ISSN: 1465-7392. DOI: 10.1038/ncb3024.

[5] K. Ivanovitch, S. Temiño, and M. Torres, "Live imaging of heart tube development in mouse reveals alternating phases of cardiac differentiation and morphogenesis", *eLife*, vol. 6, pp. 1–30, 2017, ISSN: 2050084X. DOI: 10.7554/eLife.30668.

[6] R. C. Tyser, A. M. Miranda, C.-m. Chen, S. M. Davidson, S. Srinivas, and P. R. Riley, "Calcium handling precedes cardiac differentiation to initiate the first heartbeat", *eLife*, vol. 5, M. Buckingham, Ed., e17113, 2016, ISSN: 2050-084X. DOI: 10.7554/eLife.17113.

[7] B. A. de Boer, G. van den Berg, P. A. de Boer, A. F. Moorman, and J. M. Ruijter, "Growth of the developing mouse heart: An interactive qualitative and quantitative 3d atlas", *Developmental Biology*, vol. 368, no. 2, pp. 203–213, 2012, ISSN: 0012-1606. DOI: 10.1016/j.ydbio.2012.05.001.

[8] A. Sizarov, J. Ya, B. A. de Boer, W. H. Lamers, V. M. Christoffels, and A. F. Moorman, "Formation of the building plan of the human heart: Morphogenesis, growth, and differentiation", *Circulation*, vol. 123, no. 10, pp. 1125–1135, 2011. DOI: 10.1161/CIRCULATIONAHA.110.980607.

[9] G. van den Berg, R. Abu-Issa, B. A. de Boer, M. R. Hutson, P. A. de Boer, A. T. Soufan, J. M. Ruijter, M. L. Kirby, M. J. van den Hoff, and A. F. Moorman, "A caudal proliferating growth center contributes to both poles of the forming heart tube", *Circulation research*, vol. 104, no. 2, pp. 179–188, 2009. DOI: 10.1161/CIRCRESAHA.108.185843.

[10] M. Buckingham, S. Meilhac, and S. Zaffran, "Building the mammalian heart from two sources of myocardial cells", *Nature Reviews Genetics*, vol. 6, no. 11, pp. 826–835, 2005. DOI: 10.1038/nrg1710.

[11] C.-L. Cai, X. Liang, Y. Shi, P.-H. Chu, S. L. Pfaff, J. Chen, and S. Evans, "Isl1 identifies a cardiac progenitor population that proliferates prior to differentiation and contributes a majority of cells to the heart", *Developmental cell*, vol. 5, no. 6, pp. 877–889, 2003. DOI: 10.1016/s1534-5807(03)00363-0.

[12] D. Galli, J. N. Domínguez, S. Zaffran, A. Munk, N. A. Brown, and M. E. Buckingham, "Atrial myocardium derives from the posterior region of the second heart field, which acquires left-right identity as pitx2c is expressed", vol. 135, no. 6, 1157–1167, 2008. DOI: 10.1242/dev.014563.

[13] J. L. de La Pompa, L. A. Timmerman, H. Takimoto, H. Yoshida, A. J. Elia, E. Samper, J. Potter, A. Wakeham, L. Marengere, B. L. Langille, *et al.*, "Role of the nf-atc transcription factor in morphogenesis of cardiac valves and septum", *Nature*, vol. 392, no. 6672, pp. 182–186, 1998. DOI: 10.1038/32419.

[14] C. J. Drake and P. A. Fleming, "Vasculogenesis in the day 6.5 to 9.5 mouse embryo", *Blood, The Journal of the American Society of Hematology*, vol. 95, no. 5, pp. 1671–1679, 2000. DOI: 10.1182/blood.V95.5.1671.005k39_1671_1679.

[15] C. J. Derrick and E. S. Noël, "The ecm as a driver of heart development and repair", *Development*, vol. 148, no. 5, dev191320, 2021. DOI: 10.1242/dev.191320.

[16] G. del Monte-Nieto, M. Ramialison, A. A. Adam, B. Wu, A. Aharonov, G. D'uva, L. M. Bourke, M. E. Pitulescu, H. Chen, J. L. de la Pompa, *et al.*, "Control of cardiac jelly dynamics by notch1 and nrg1 defines the building plan for trabeculation", *Nature*, vol. 557, no. 7705, pp. 439–445, 2018. DOI: 10.1038/s41586-018-0110-6.

[17] I. Esteban, P. Schmidt, A. Desgrange, M. Raiola, S. Temiño, S. M. Meilhac, L. Kobbelt, and M. Torres, "Pseudodynamic analysis of heart tube formation in the mouse reveals strong regional variability and early left–right asymmetry", *Nature Cardiovascular Research*, vol. 1, pp. 504–517, 5 May 2022, ISSN: 2731-0590. DOI: 10.1038/s44161-022-00065-1.

[18] M. Sendra, J. Domínguez, M. Torres, and O. Ocaña, "Dissecting the complexity of early heart progenitor cells", *Journal of Cardiovascular Development and Disease*, vol. 9, p. 5, 1 Dec. 2021, ISSN: 2308-3425. DOI: 10.3390/jcdd9010005.

[19] S. Hultin *et al.*, "Amotl2 links ve-cadherin to contractile actin fibres necessary for aortic lumen expansion", *Nature Communications*, vol. 5, p. 3743, 1 Sep. 2014, ISSN: 2041-1723. DOI: 10.1038/ncomms4743.

[20] B. Strilić, T. Kučera, J. Eglinger, M. R. Hughes, K. M. McNagny, S. Tsukita, E. Dejana, N. Ferrara, and E. Lammert, "The molecular basis of vascular lumen formation in the developing mouse aorta", *Developmental Cell*, vol. 17, pp. 505–515, 4 Oct. 2009, ISSN: 15345807. DOI: 10.1016/j.devcel.2009.08.011.

[21] V. Gebala, R. Collins, I. Geudens, L.-K. Phng, and H. Gerhardt, "Blood flow drives lumen formation by inverse membrane blebbing during angiogenesis in vivo", *Nature cell biology*, vol. 18, no. 4, pp. 443–450, 2016. DOI: 10.1038/ncb3320.

[22] M. Zeeb, B. Strilic, and E. Lammert, "Resolving cell–cell junctions: Lumen formation in blood vessels", *Current Opinion in Cell Biology*, vol. 22, pp. 626–632, 5 Oct. 2010, ISSN: 09550674. DOI: 10.1016/j.ceb.2010.07.003.

[23] M. G. Lampugnani, F. Orsenigo, N. Rudini, L. Maddaluno, G. Boulday, F. Chapon, and E. Dejana, "Ccm1 regulates vascular-lumen organization by inducing endothelial polarity", *Journal of Cell Science*, vol. 123, pp. 1073–1080, 7 Apr. 2010, ISSN: 1477-9137. DOI: 10.1242/jcs.059329.

[24] V. Caolo, H. M. Peacock, B. Kasaai, G. Swennen, E. Gordon, L. Claesson-Welsh, M. J. Post, P. Verhamme, and E. A. Jones, "Shear stress and ve-cadherin: The molecular mechanism of vascular fusion", *Arteriosclerosis, thrombosis, and vascular biology*, vol. 38, no. 9, pp. 2174–2183, 2018. DOI: 10.1161/ATVBAHA.118.310823.

[25] S. Zaffran, R. G. Kelly, S. M. Meilhac, M. E. Buckingham, and N. A. Brown, "Right ventricular myocardium derives from the anterior heart field", *Circulation Research*, vol. 95, pp. 261–268, 3 Aug. 2004, ISSN: 0009-7330. DOI: 10.1161/01.RES.0000136815.73623.BE.

[26] G. C. Rosenquist, "Location and movements of cardiogenic cells in the chick embryo: The heart-forming portion of the primitive streak", *Developmental Biology*, vol. 22, no. 3, pp. 461–475, 1970, ISSN: 0012-1606. DOI: 10.1016/0012-1606(70)90163-6.

[27] K. Ivanovitch, I. Esteban, and M. Torres, "Growth and morphogenesis during early heart development in amniotes", *Journal of Cardiovascular Development and Disease*, vol. 4, p. 20, 4 2017, ISSN: 2308-3425. DOI: 10.3390/jcdd4040020.

[28] B. S. de Bakker, K. H. de Jong, J. Hagoort, K. de Bree, C. T. Besselink, F. E. de Kanter, T. Veldhuis, B. Bais, R. Schildmeijer, J. M. Ruijter, *et al.*, "An interactive three-dimensional digital atlas and quantitative database of human development", *Science*, vol. 354, no. 6315, aag0053, 2016. DOI: 10.1126/science.aag0053.

[29] B. A. de Boer, G. van den Berg, P. A. de Boer, A. F. Moorman, and J. M. Ruijter, "Growth of the developing mouse heart: An interactive qualitative and quantitative 3d atlas", *Developmental biology*, vol. 368, no. 2, pp. 203–213, 2012. DOI: 10.1016/j.ydbio.2012.05.001.

[30] J. W. Faber, J. Hagoort, A. F. Moorman, V. M. Christoffels, and B. Jensen, "Quantified growth of the human embryonic heart", *Biology open*, vol. 10, no. 2, bio057059, 2021. DOI: 10.1242/bio.057059.

[31] A. T. Soufan, G. van den Berg, J. M. Ruijter, P. A. de Boer, M. J. van den Hoff, and A. F. Moorman, "Regionalized sequence of myocardial cell growth and proliferation characterizes early chamber formation", *Circulation research*, vol. 99, no. 5, pp. 545–552, 2006. DOI: 10.1161/01.RES.0000239407.45137.97.

[32] N. Kawahira, D. Ohtsuka, N. Kida, K.-i. Hironaka, and Y. Morishita, "Quantitative analysis of 3d tissue deformation reveals key cellular mechanism associated with initial heart looping", *Cell reports*, vol. 30, no. 11, pp. 3889–3903, 2020. DOI: 10.1016/j.celrep.2020.02.071.

[33] T. J. Mohun and R. H. Anderson, "3d anatomy of the developing heart: Understanding ventricular septation", *Cold Spring Harbor Perspectives in Biology*, vol. 12, no. 11, a037465, 2020. DOI: 10.1101/cshperspect.a037465.

[34] A. L. Lopez, S. Wang, and I. V. Larina, "Embryonic mouse cardiodynamic oct imaging", *Journal of Cardiovascular Development and Disease*, vol. 7, no. 4, p. 42, 2020. DOI: 10.3390/jcdd7040042.

[35] Y. Yue, W. Zong, X. Li, J. Li, Y. Zhang, R. Wu, Y. Liu, J. Cui, Q. Wang, Y. Bian, *et al.*, "Long-term, in toto live imaging of cardiomyocyte behaviour during mouse ventricle chamber formation at single-cell resolution", *Nature cell biology*, vol. 22, no. 3, pp. 332–340, 2020. DOI: 10.1038/s41556-020-0475-2.

[36] J.-F. Le Garrec, J. N. Domínguez, A. Desgrange, K. D. Ivanovitch, E. Raphaël, J. A. Bangham, M. Torres, E. Coen, T. J. Mohun, and S. M. Meilhac, "A predictive model of asymmetric morphogenesis from 3d reconstructions of mouse heart looping dynamics", *Elife*, vol. 6, e28951, 2017. DOI: 10.7554/eLife.28951.

[37] K. McDole, L. Guignard, F. Amat, A. Berger, G. Malandain, L. A. Royer, S. C. Turaga, K. Branson, and P. J. Keller, "In toto imaging and reconstruction of post-implantation mouse development at the single-cell level", *Cell*, vol. 175, no. 3, pp. 859–876, 2018. DOI: 10.1016/j.cell.2018.09.031.

[38] Y. Wan, K. McDole, and P. J. Keller, "Light-sheet microscopy and its potential for understanding developmental processes", *Annual review of cell and developmental biology*, vol. 35, pp. 655–681, 2019. DOI: 10.1146/annurev-cellbio-100818-125311.

[39] M. Minsky, "Microscopy apparatus", U.S. Patent No. 3013467, December 19, 1961.

[40] A. C. Bovik, *Handbook of image and video processing*. Academic press, 2010. DOI: 10.1016/B978-0-12-119792-6.X5062-1.

[41] A. D. Elliott, "Confocal microscopy: Principles and modern practices", *Current Protocols in Cytometry*, vol. 92, 1 Mar. 2020, ISSN: 1934-9297. DOI: 10.1002/cpcy.68.

[42] E. A. Susaki, K. Tainaka, D. Perrin, H. Yukinaga, A. Kuno, and H. R. Ueda, "Advanced cubic protocols for whole-brain and whole-body clearing and imaging", *Nature Protocols*, vol. 10, pp. 1709–1727, 11 2015, ISSN: 17502799. DOI: 10.1038/nprot.2015.085.

[43] S. Hildebrand, A. Schueth, K. v. Wangenheim, C. Mattheyer, F. Pampaloni, H. Bratzke, A. F. Roebroeck, and R. A. Galuske, "Hfruit: An optimized agent for optical clearing of dii-stained adult human brain tissue", *Scientific reports*, vol. 10, no. 1, pp. 1–10, 2020. DOI: 10.1038/s41598-020-66999-3.

[44] F. Helmchen and W. Denk, "Deep tissue two-photon microscopy", *Nature methods*, vol. 2, no. 12, pp. 932–940, 2005. DOI: 10.1038/nmeth818.

[45] W. Denk, J. H. Strickler, and W. W. Webb, "Two-photon laser scanning fluorescence microscopy", *Science*, vol. 248, no. 4951, pp. 73–76, 1990. DOI: 10.1126/science.2321027.

[46] M. Göppert-Mayer, "Über elementarakte mit zwei quantensprüngen", *Annalen der Physik*, vol. 401, no. 3, pp. 273–294, 1931. DOI: 10.1002/andp.19314010303.

[47] G. Peleg, A. Lewis, M. Linial, and L. M. Loew, "Nonlinear optical measurement of membrane potential around single molecules at selected cellular sites", *Proceedings of the National Academy of Sciences*, vol. 96, no. 12, pp. 6700–6704, 1999. DOI: 10.1073/pnas.96.12.6700.

[48] M. Calvo-Rodriguez, E. K. Kharitonova, and B. J. Bacskai, "In vivo brain imaging of mitochondrial ca2+ in neurodegenerative diseases with multiphoton microscopy", *Biochimica et Biophysica Acta (BBA)-Molecular Cell Research*, vol. 1868, no. 6, p. 118 998, 2021. DOI: 10.1016/j.bbamcr.2021.118998.

[49] H. Liu, X. Deng, S. Tong, C. He, H. Cheng, Z. Zhuang, M. Gan, J. Li, W. Xie, P. Qiu, *et al.*, "In vivo deep-brain structural and hemodynamic multiphoton microscopy enabled by quantum dots", *Nano letters*, vol. 19, no. 8, pp. 5260–5265, 2019. DOI: 10.1021/acs.nanolett.9b01708.

[50] E. E. Hoover and J. A. Squier, "Advances in multiphoton microscopy technology", *Nature Photonics*, vol. 7, pp. 93–101, 2 Feb. 2013, ISSN: 1749-4885. DOI: 10.1038/nphoton.2012.361.

[51] I.-H. Chen, S.-W. Chu, C.-K. Sun, P.-C. Cheng, and B.-L. Lin, "Wavelength dependent damage in biological multi-photon confocal microscopy: A micro-spectroscopic comparison between femtosecond ti: Sapphire and cr: Forsterite laser sources", *Optical and Quantum electronics*, vol. 34, no. 12, pp. 1251–1266, 2002. DOI: 10.1023/A:1021303426482.

[52] P. Theer and W. Denk, "On the fundamental imaging-depth limit in two-photon microscopy", *JOSA A*, vol. 23, no. 12, pp. 3139–3149, 2006. DOI: 10.1364/josaa.23.003139.

[53] S. Wang, I. V. Larina, and K. V. Larin, "Label-free optical imaging in developmental biology", *Biomedical Optics Express*, vol. 11, no. 4, pp. 2017–2040, 2020. DOI: 10.1364/BOE.381359.

[54] T. Wang and C. Xu, "Three-photon neuronal imaging in deep mouse brain", *Optica*, vol. 7, no. 8, pp. 947–960, 2020. DOI: 10.1364/OPTICA.395825.

[55] D. Kobat, M. E. Durst, N. Nishimura, A. W. Wong, C. B. Schaffer, and C. Xu, "Deep tissue multiphoton microscopy using longer wavelength excitation", *Optics express*, vol. 17, no. 16, pp. 13 354–13 364, 2009. DOI: 10.1364/OE.17.013354.

[56] D. Kobat, N. G. Horton, and C. Xu, "In vivo two-photon microscopy to 1.6-mm depth in mouse cortex", *Journal of biomedical optics*, vol. 16, no. 10, p. 106 014, 2011. DOI: 10.1117/1.3646209.

[57] N. G. Horton, K. Wang, D. Kobat, C. G. Clark, F. W. Wise, C. B. Schaffer, and C. Xu, "In vivo three-photon microscopy of subcortical structures within an intact mouse brain", *Nature photonics*, vol. 7, no. 3, pp. 205–209, 2013. DOI: 10.1038/nphoton.2012.336.

[58] J. Huisken, J. Swoger, F. Del Bene, J. Wittbrodt, and E. H. Stelzer, "Optical sectioning deep inside live embryos by selective plane illumination microscopy", *Science*, vol. 305, no. 5686, pp. 1007–1009, 2004. DOI: 10.1126/science.1100035.

[59] P. J. Keller and E. H. Stelzer, "Quantitative in vivo imaging of entire embryos with digital scanned laser light sheet fluorescence microscopy", *Current opinion in neurobiology*, vol. 18, no. 6, pp. 624–632, 2008. DOI: 10.1016/j.conb.2009.03.008.

[60] A. Rohrbach, "Artifacts resulting from imaging in scattering media: A theoretical prediction", *Optics letters*, vol. 34, no. 19, pp. 3041–3043, 2009. DOI: 10.1364/OL.34.003041.

[61] F. O. Fahrbach, P. Simon, and A. Rohrbach, "Microscopy with self-reconstructing beams", *Nature photonics*, vol. 4, no. 11, pp. 780–785, 2010. DOI: 10.1038/nphoton.2010.204.

[62] P. J. Keller, A. D. Schmidt, J. Wittbrodt, and E. H. Stelzer, "Reconstruction of zebrafish early embryonic development by scanned light sheet microscopy", *science*, vol. 322, no. 5904, pp. 1065–1069, 2008. DOI: 10.1126/science.1162493.

[63] T. Breuninger, K. Greger, and E. H. Stelzer, "Lateral modulation boosts image quality in single plane illumination fluorescence microscopy", *Optics letters*, vol. 32, no. 13, pp. 1938–1940, 2007. DOI: 10.1364/ol.32.001938.

[64] P. J. Keller, A. D. Schmidt, A. Santella, K. Khairy, Z. Bao, J. Wittbrodt, and E. H. Stelzer, "Fast, high-contrast imaging of animal development with scanned light sheet–based structured-illumination microscopy", *Nature methods*, vol. 7, no. 8, pp. 637–642, 2010. DOI: 10.1038/nmeth.1476.

[65] T. V. Truong, W. Supatto, D. S. Koos, J. M. Choi, and S. E. Fraser, "Deep and fast live imaging with two-photon scanned light-sheet microscopy", *Nature methods*, vol. 8, no. 9, pp. 757–760, 2011. DOI: 10.1038/nmeth.1652.

[66] P. Mahou, J. Vermot, E. Beaurepaire, and W. Supatto, "Multicolor two-photon light-sheet microscopy", *Nature methods*, vol. 11, no. 6, pp. 600–601, 2014. DOI: 10.1038/nmeth.2963.

[67] R. Tomer, K. Khairy, F. Amat, and P. J. Keller, "Quantitative high-speed imaging of entire developing embryos with simultaneous multiview light-sheet microscopy", *Nature methods*, vol. 9, no. 7, pp. 755–763, 2012. DOI: 10.1038/nmeth.2062.

[68] U. Krzic, S. Gunther, T. E. Saunders, S. J. Streichan, and L. Hufnagel, "Multiview light-sheet microscope for rapid in toto imaging", *Nature methods*, vol. 9, no. 7, pp. 730–733, 2012. DOI: 10.1038/nmeth.2064.

[69] Y. Wu, P. Wawrzusin, J. Senseney, R. S. Fischer, R. Christensen, A. Santella, A. G. York, P. W. Winter, C. M. Waterman, Z. Bao, *et al.*, "Spatially isotropic four-dimensional imaging with dual-view plane illumination microscopy", *Nature biotechnology*, vol. 31, no. 11, pp. 1032–1038, 2013. DOI: 10.1038/nbt.2713.

[70] R. K. Chhetri, F. Amat, Y. Wan, B. Höckendorf, W. C. Lemon, and P. J. Keller, "Whole-animal functional and developmental imaging with isotropic spatial resolution", *Nature methods*, vol. 12, no. 12, pp. 1171–1178, 2015. DOI: 10.1038/nmeth.3632.

[71] L. A. Royer, W. C. Lemon, R. K. Chhetri, Y. Wan, M. Coleman, E. W. Myers, and P. J. Keller, "Adaptive light-sheet microscopy for long-term, high-resolution imaging in living organisms", *Nature biotechnology*, vol. 34, no. 12, pp. 1267–1278, 2016. DOI: 10.1038/nbt.3708.

[72] A.-K. Gustavsson, P. N. Petrov, M. Y. Lee, Y. Shechtman, and W. Moerner, "3d single-molecule super-resolution microscopy with a tilted light sheet", *Nature communications*, vol. 9, no. 1, pp. 1–8, 2018. DOI: 10.1038/s41467-017-02563-4.

[73] A. M. Valm, S. Cohen, W. R. Legant, J. Melunis, U. Hershberg, E. Wait, A. R. Cohen, M. W. Davidson, E. Betzig, and J. Lippincott-Schwartz, "Applying systems-level spectral imaging and analysis to reveal the organelle interactome", *Nature*, vol. 546, no. 7656, pp. 162–167, 2017. DOI: 10.1038/nature22369.

[74] T.-L. Liu, S. Upadhyayula, D. E. Milkie, V. Singh, K. Wang, I. A. Swinburne, K. R. Mosaliganti, Z. M. Collins, T. W. Hiscock, J. Shea, *et al.*, "Observing the cell in its native state: Imaging subcellular dynamics in multicellular organisms", *Science*, vol. 360, no. 6386, eaaq1392, 2018. DOI: 10.1126/science.aaq1392.

[75] J. Reichmann, B. Nijmeijer, M. J. Hossain, M. Eguren, I. Schneider, A. Z. Politi, M. J. Roberti, L. Hufnagel, T. Hiiragi, and J. Ellenberg, "Dual-spindle formation in zygotes keeps parental genomes apart in early mammalian embryos", *Science*, vol. 361, no. 6398, pp. 189–193, 2018. DOI: 10.1126/science.aar7462.

[76] C. Wolff, J.-Y. Tinevez, T. Pietzsch, E. Stamataki, B. Harich, L. Guignard, S. Preibisch, S. Shorte, P. J. Keller, P. Tomancak, *et al.*, "Multi-view light-sheet imaging and tracking with the mamut software reveals the cell lineage of a direct developing arthropod limb", *Elife*, vol. 7, e34410, 2018. DOI: 10.7554/eLife.34410.

[77] V. Hamburger and H. L. Hamilton, "A series of normal stages in the development of the chick embryo", *Developmental dynamics*, vol. 195, no. 4, pp. 231–272, 1992. DOI: 10.1002/aja.1001950404.

[78] A. A. Pearson, "The development of the eyelids. part i. external features.", *Journal of anatomy*, vol. 130, no. Pt 1, p. 33, 1980. [Online]. Available: https://www.ncbi.nlm.nih.gov/pmc/articles/PMC1233106/.

[79] J. P. Shah and P. H. Montero, "New ajcc/uicc staging system for head and neck, and thyroid cancer", *Revista Médica Clínica Las Condes*, vol. 29, no. 4, pp. 397–404, 2018. DOI: 10.1016/j.rmclc.2018.07.002.

[80] S. L. Walsh, A. U. Wells, N. Sverzellati, G. J. Keir, L. Calandriello, K. M. Antoniou, S. J. Copley, A. Devaraj, T. M. Maher, E. Renzoni, *et al.*, "An integrated clinicoradiological staging system for pulmonary sarcoidosis: A case-cohort study", *The Lancet Respiratory Medicine*, vol. 2, no. 2, pp. 123–130, 2014. DOI: 10.1016/S2213-2600(13)70276-5.

[81] B. Boehm, M. Rautschka, L. Quintana, J. Raspopovic, Ž. Jan, and J. Sharpe, "A landmark-free morphometric staging system for the mouse limb bud", *Development*, vol. 138, no. 6, pp. 1227–1234, 2011. DOI: 10.1242/dev.057547.

[82] M. Musy, K. Flaherty, J. Raspopovic, A. Robert-Moreno, J. T. Richtsmeier, and J. Sharpe, "A quantitative method for staging mouse embryos based on limb morphometry", *Development*, vol. 145, no. 7, dev154856, 2018. DOI: 10.1242/dev.154856.

[83] N Wanek, K Muneoka, G Holler-Dinsmore, R Burton, and S. Bryant, "A staging system for mouse limb development", *Journal of Experimental Zoology*, vol. 249, no. 1, pp. 41–49, 1989. DOI: 10.1002/jez.1402490109.

[84] M. D. Wong, M. C. van Eede, S. Spring, S. Jevtic, J. C. Boughner, J. P. Lerch, and R. M. Henkelman, "4d atlas of the mouse embryo for precise morphological staging", *Development*, vol. 142, no. 20, pp. 3583–3591, 2015. DOI: 10.1242/dev.125872.

[85] S. H. Geyer, L. Reissig, J. Rose, R. Wilson, F. Prin, D. Szumska, R. Ramirez-Solis, C. Tudor, J. White, T. J. Mohun, *et al.*, "A staging system for correct phenotype interpretation of mouse embryos harvested on embryonic day 14 (e14. 5)", *Journal of anatomy*, vol. 230, no. 5, pp. 710–719, 2017. DOI: 10.1111/joa.12590.

[86] P. Kakanj, S. A. Eming, L. Partridge, and M. Leptin, "Long-term in vivo imaging of drosophila larvae", *Nature Protocols*, vol. 15, no. 3, pp. 1158–1187, 2020. DOI: 10.1038/s41596-019-0282-z.

[87] L. Cong, Z. Wang, Y. Chai, W. Hang, C. Shang, W. Yang, L. Bai, J. Du, K. Wang, and Q. Wen, "Rapid whole brain imaging of neural activity in freely behaving larval zebrafish (danio rerio)", *Elife*, vol. 6, 2017. DOI: 10.7554/eLife.28158.

[88] L. Breimann, F. Preusser, and S. Preibisch, "Light-microscopy methods in c. elegans research", *Current Opinion in Systems Biology*, vol. 13, pp. 82–92, 2019. DOI: 10.1016/j.coisb.2018.11.004.

[89] C. K. Phoon and D. H. Turnbull, "Ultrasound biomicroscopy-doppler in mouse cardiovascular development", *Physiological genomics*, vol. 14, no. 1, pp. 3–15, 2003. DOI: 10.1152/physiolgenomics.00008.2003.

[90] P. Parasoglou, C. A. Berrios-Otero, B. J. Nieman, and D. H. Turnbull, "High-resolution mri of early-stage mouse embryos", *NMR in Biomedicine*, vol. 26, no. 2, pp. 224–231, 2013. DOI: 10.1002/nbm.2843.

[91] B. Hogers, D. Gross, V. Lehmann, K. Zick, H. J. De Groot, A. C. Gittenberger-De Groot, and R. E. Poelmann, "Magnetic resonance microscopy of mouse embryos in utero", *The Anatomical Record: An Official Publication of the American Association of Anatomists*, vol. 260, no. 4, pp. 373–377, 2000. DOI: 10.1002/1097-0185(20001201)260:4<373::AID-AR60>3.0.CO;2-Q.

[92] E. L. Ritman, "Micro-computed tomography—current status and developments", *Annu. Rev. Biomed. Eng.*, vol. 6, pp. 185–208, 2004. DOI: 10.1146/annurev.bioeng.6.040803.140130.

[93] D. Wu, L. J. Richards, Z. Zhao, Z. Cao, W. Luo, W. Shao, S.-H. Shi, M. I. Miller, S. Mori, S. Blackshaw, *et al.*, "A diffusion mri-based spatiotemporal continuum of the embryonic mouse brain for probing gene–neuroanatomy connections", *Proceedings of the National Academy of Sciences*, vol. 119, no. 7, e2111869119, 2022. DOI: 10.1073/pnas.2111869119.

[94] Y. Morishita, K.-i. Hironaka, S.-W. Lee, T. Jin, and D. Ohtsuka, "Reconstructing 3d deformation dynamics for curved epithelial sheet morphogenesis from positional data of sparsely-labeled cells", *Nature communications*, vol. 8, no. 1, pp. 1–15, 2017. DOI: 10.1038/s41467-017-00023-7.

[95] J. J. Perez, R. A. Perez, and A. Perez, "Computational modeling as a tool to investigate ppi: From drug design to tissue engineering", *Frontiers in Molecular Biosciences*, vol. 8, p. 451, 2021. DOI: 10.3389/fmolb.2021.681617.

[96] P. J. Albert and U. S. Schwarz, "Dynamics of cell ensembles on adhesive micropatterns: Bridging the gap between single cell spreading and collective cell migration", *PLoS computational biology*, vol. 12, no. 4, e1004863, 2016. DOI: 10.1371/journal.pcbi.1004863.

[97] M. A. Wyczalkowski, Z. Chen, B. A. Filas, V. D. Varner, and L. A. Taber, "Computational models for mechanics of morphogenesis", *Birth defects research part C: Embryo today: Reviews*, vol. 96, no. 2, pp. 132–152, 2012. DOI: 10.1002/bdrc.21013.

[98] D. Pearce, S. Fischer, F. Huda, and A. Vahdati, "Applications of computer modeling and simulation in cartilage tissue engineering", *Tissue engineering and regenerative medicine*, vol. 17, no. 1, pp. 1–13, 2020. [Online]. Available: 10.1007/s13770-019-00216-9.

[99] R. Mittal, J. H. Seo, V. Vedula, Y. J. Choi, H. Liu, H. H. Huang, S. Jain, L. Younes, T. Abraham, and R. T. George, "Computational modeling of cardiac hemodynamics: Current status and future outlook", *Journal of Computational Physics*, vol. 305, pp. 1065–1082, 2016, ISSN: 0021-9991. DOI: 10.1016/j.jcp.2015.11.022.

[100] R. Alert and X. Trepat, "Physical models of collective cell migration", *Annual Review of Condensed Matter Physics*, vol. 11, pp. 77–101, 2020. DOI: 10.1146/annurev-conmatphys-031218-013516.

[101] A. Nealen, M. Müller, R. Keiser, E. Boxerman, and M. Carlson, "Physically based deformable models in computer graphics", *Computer Graphics Forum*, vol. 25, no. 4, pp. 809–836, 2006. DOI: 10.1111/j.1467-8659.2006.01000.x.

[102] H. Gao, E. Bozkir, L. Hasenbein, J.-U. Hahn, R. Göllner, and E. Kasneci, "Digital transformations of classrooms in virtual reality", in *Proceedings of the 2021 CHI Conference on Human Factors in Computing Systems*, 2021, pp. 1–10. DOI: 10.1145/3411764.3445596.

[103] P. Schmidt, M. Campen, J. Born, and L. Kobbelt, "Inter-surface maps via constant-curvature metrics", *ACM Transactions on Graphics*, vol. 39, 4 Aug. 2020, ISSN: 0730-0301. DOI: 10.1145/3386569.3392399.

[104] P. Schmidt, J. Born, M. Campen, and L. Kobbelt, "Distortion-minimizing injective maps between surfaces", *ACM Trans. Graph.*, vol. 38, no. 6, 2019, ISSN: 0730-0301. DOI: 10.1145/3355089.3356519.

[105] Z. Deng, J. Bednařík, M. Salzmann, and P. Fua, "Better patch stitching for parametric surface reconstruction", in *2020 International Conference on 3D Vision (3DV)*, IEEE, 2020, pp. 593–602. DOI: 10.48550/arXiv.2010.07021.

[106] M. Campen, R. Capouellez, H. Shen, L. Zhu, D. Panozzo, and D. Zorin, "Efficient and robust discrete conformal equivalence with boundary", *ACM Transactions on Graphics (TOG)*, vol. 40, no. 6, pp. 1–16, 2021. DOI: 10.48550/arXiv.2104.04614.

[107] C. Yu, C. Brakensiek, H. Schumacher, and K. Crane, "Repulsive surfaces", *ACM Trans. Graph.*, vol. 40, no. 6, 2021, ISSN: 0730-0301. DOI: 10.1145/3478513.3480521.

[108] J. M. Phillip, K.-S. Han, W.-C. Chen, D. Wirtz, and P.-H. Wu, "A robust unsupervised machine-learning method to quantify the morphological heterogeneity of cells and nuclei", *Nature protocols*, vol. 16, no. 2, pp. 754–774, 2021. DOI: 10.1038/s41596-020-00432-x.

[109] N. Chenouard, I. Smal, F. De Chaumont, M. Maška, I. F. Sbalzarini, Y. Gong, J. Cardinale, C. Carthel, S. Coraluppi, M. Winter, *et al.*, "Objective comparison of particle tracking methods", *Nature methods*, vol. 11, no. 3, pp. 281–289, 2014. DOI: 10.1038/nmeth.2808.

[110] D. Ershov, M.-S. Phan, J. W. Pylvänäinen, S. U. Rigaud, L. Le Blanc, A. Charles-Orszag, J. R. Conway, R. F. Laine, N. H. Roy, D. Bonazzi, *et al.*, "Trackmate 7: Integrating state-of-the-art segmentation algorithms into tracking pipelines", *Nature Methods*, pp. 1–4, 2022. DOI: 10.1038/s41592-022-01507-1.

[111] G. Blin, D. Sadurska, R. Portero Migueles, N. Chen, J. A. Watson, and S. Lowell, "Nessys: A new set of tools for the automated detection of nuclei within intact tissues and dense 3d cultures", *PLoS biology*, vol. 17, no. 8, e3000388, 2019. DOI: 10.1371/journal.pbio.3000388.

[112] E. Moen, D. Bannon, T. Kudo, W. Graf, M. Covert, and D. Van Valen, "Deep learning for cellular image analysis", *Nature methods*, vol. 16, no. 12, pp. 1233–1246, 2019. DOI: 10.1038/s41592-019-0403-1.

[113] C. Stringer, T. Wang, M. Michaelos, and M. Pachitariu, "Cellpose: A generalist algorithm for cellular segmentation", *Nature methods*, vol. 18, no. 1, pp. 100–106, 2021. DOI: 10.1038/s41592-020-01018-x.

[114] C. Shorten and T. M. Khoshgoftaar, "A survey on image data augmentation for deep learning", *Journal of big data*, vol. 6, no. 1, pp. 1–48, 2019. DOI: 10.1186/s40537-019-0197-0.

[115] Y. Saga, S. Miyagawa-Tomita, A. Takagi, S. Kitajima, J. Miyazaki, and T. Inoue, "Mesp1 is expressed in the heart precursor cells and required for the formation of a single heart tube", *Development*, vol. 126, pp. 3437–3447, 15 Aug. 1999, ISSN: 1477-9129. DOI: 10.1242/dev.126.15.3437.

[116] M. D. Muzumdar, B. Tasic, K. Miyamichi, L. Li, and L. Luo, "A global double-fluorescent cre reporter mouse", *genesis*, vol. 45, pp. 593–605, 9 Sep. 2007, ISSN: 1526954X. DOI: 10.1002/dvg.20335.

[117] C. C. Lu and E. J. Robertson, "Multiple roles for nodal in the epiblast of the mouse embryo in the establishment of anterior-posterior patterning", *Developmental Biology*, vol. 273, pp. 149–159, 1 Sep. 2004, ISSN: 00121606. DOI: 10.1016/j.ydbio.2004.06.004.

[118] A. Desgrange, J.-F. L. Garrec, S. Bernheim, T. H. Bønnelykke, and S. M. Meilhac, "Transient nodal signaling in left precursors coordinates opposed asymmetries shaping the heart loop", *Developmental Cell*, vol. 55, 413–431.e6, 4 Nov. 2020, ISSN: 15345807. DOI: 10.1016/j.devcel.2020.10.008.

[119] B. R. Arenkiel, G. O. Gaufo, and M. R. Capecchi, "Hoxb1 neural crest preferentially form glia of the pns", *Developmental Dynamics*, vol. 227, pp. 379–386, 3 Jul. 2003, ISSN: 1058-8388. DOI: 10.1002/dvdy.10323.

[120] E. A. Susaki, K. Tainaka, D. Perrin, F. Kishino, T. Tawara, T. M. Watanabe, C. Yokoyama, H. Onoe, M. Eguchi, S. Yamaguchi, *et al.*, "Whole-brain imaging with single-cell resolution using chemical cocktails and computational analysis", *Cell*, vol. 157, no. 3, pp. 726–739, 2014. DOI: 10.1016/j.cell.2014.03.042.

[121] C. R. Harris *et al.*, "Array programming with numpy", *Nature*, vol. 585, pp. 357–362, 7825 Sep. 2020, ISSN: 0028-0836. DOI: 10.1038/s41586-020-2649-2.

[122] P. A. Yushkevich, J. Piven, H. Cody Hazlett, R. Gimpel Smith, S. Ho, J. C. Gee, and G. Gerig, "User-guided 3D active contour segmentation of anatomical structures: Significantly improved efficiency and reliability", *Neuroimage*, vol. 31, no. 3, pp. 1116–1128, 2006. DOI: 10.1016/j.neuroimage.2006.01.015.

[123] V. Caselles, R. Kimmel, and G. Sapiro, "Geodesic active contours", *International journal of computer vision*, vol. 22, no. 1, pp. 61–79, 1997. DOI: 10.1023/A:1007979827043.

[124] S. C. Zhu and A. Yuille, "Region competition: Unifying snakes, region growing, and bayes/mdl for multiband image segmentation", *IEEE transactions on pattern analysis and machine intelligence*, vol. 18, no. 9, pp. 884–900, 1996. DOI: 10.1109/34.537343.

[125] S. Tani, U. il Chung, S. Ohba, and H. Hojo, "Understanding paraxial mesoderm development and sclerotome specification for skeletal repair", *Experimental and Molecular Medicine*, vol. 52, pp. 1166–1177, 8 2020, Define muy bien el origen del mesoderm, y a lo que origina el lado somático y esplácnico del lateral plate., ISSN: 20926413. DOI: 10.1038/s12276-020-0482-1.

[126] K. He, G. Gkioxari, P. Dollár, and R. Girshick, "Mask r-cnn", 2017. DOI: 10.48550/ARXIV.1703.06870.

[127] M. Brett *et al.*, "Nipy/nibabel: 3.1.1", 2020. DOI: 10.5281/zenodo.3924343.

[128] P. Virtanen *et al.*, "SciPy 1.0: Fundamental Algorithms for Scientific Computing in Python", *Nature Methods*, vol. 17, pp. 261–272, 2020. DOI: 10.1038/s41592-019-0686-2.

[129] W. E. Lorensen and H. E. Cline, "Marching cubes: A high resolution 3d surface construction algorithm", *ACM siggraph computer graphics*, vol. 21, no. 4, pp. 163–169, 1987. DOI: 10.1145/37402.37422.

[130] G. Taubin, "Curve and surface smoothing without shrinkage", in *Proceedings of IEEE International Conference on Computer Vision*, 1995, pp. 852–857. DOI: 10.1109/ICCV.1995.466848.

[131] M. Garland and P. S. Heckbert, "Surface simplification using quadric error metrics", in *Proceedings of the 24th Annual Conference on Computer Graphics and Interactive Techniques*, ser. SIGGRAPH '97, USA: ACM Press/Addison-Wesley Publishing Co., 1997, 209–216, ISBN: 0897918967. DOI: 10.1145/258734.258849.

[132] Q.-Y. Zhou, J. Park, and V. Koltun, "Open3D: A modern library for 3D data processing", *arXiv:1801.09847*, 2018. [Online]. Available: http://www.open3d.org/.

[133] P. Cignoni, M. Callieri, M. Corsini, M. Dellepiane, F. Ganovelli, and G. Ranzuglia, "MeshLab: an Open-Source Mesh Processing Tool", in *Eurographics Italian Chapter Conference*, V. Scarano, R. D. Chiara, and U. Erra, Eds., The Eurographics Association, 2008, ISBN: 978-3-905673-68-5. DOI: 10.2312/LocalChapterEvents/ItalChap/ItalianChapConf2008/129-136.

[134] S. Yoshizawa, A. G. Belyaev, and H.-P. Seidel, "Free-form skeleton-driven mesh deformations", in *SM '03: Proceedings of the eighth ACM symposium on Solid modeling and applications*, Seattle, Washington, USA: ACM, 2003, pp. 247–253, ISBN: 1-58113-706-0. DOI: 10.1145/781606.781643.

[135] L.-Y. Wei, "Parallel poisson disk sampling", *ACM Trans. Graph.*, vol. 27, no. 3, 1–9, 2008, ISSN: 0730-0301. DOI: 10.1145/1360612.1360619.

[136] F. Bernardini, J. Mittleman, H. Rushmeier, C. Silva, and G. Taubin, "The ball-pivoting algorithm for surface reconstruction", *IEEE Transactions on Visualization and Computer Graphics*, vol. 5, no. 4, pp. 349–359, 1999. DOI: 10.1109/2945.817351.

[137] J. Digne, "An analysis and implementation of a parallel ball pivoting algorithm", *Image Processing On Line*, vol. 4, pp. 149–168, 2014. DOI: 10.5201/ipol.2014.81.

[138] A. A. Hagberg, D. A. Schult, and P. J. Swart, "Exploring network structure, dynamics, and function using networkx", in *Proceedings of the 7th Python in Science Conference*, G. Varoquaux, T. Vaught, and J. Millman, Eds., Pasadena, CA USA, 2008, pp. 11 –15. [Online]. Available: http://conference.scipy.org/proceedings/SciPy2008/paper_2/.

[139] J. Born, P. Schmidt, and L. Kobbelt, "Layout embedding via combinatorial optimization", *Computer Graphics Forum*, vol. 40, pp. 277–290, 2 May 2021, ISSN: 0167-7055. DOI: 10.1111/cgf.142632.

[140] J. Schreiner, A. Asirvatham, E. Praun, and H. Hoppe, "Inter-surface mapping", *ACM Trans. Graph.*, vol. 23, no. 3, 870–877, 2004, ISSN: 0730-0301. DOI: 10.1145/1015706.1015812.

[141] M. Botsch and L. Kobbelt, "A remeshing approach to multiresolution modeling", in *Proceedings of the 2004 Eurographics/ACM SIGGRAPH Symposium on Geometry Processing*, ser. SGP '04, Nice, France: Association for Computing Machinery, 2004, 185–192, ISBN: 3905673134. DOI: 10.1145/1057432.1057457.

[142] M. Dunyach, D. Vanderhaeghe, L. Barthe, and M. Botsch, "Adaptive Remeshing for Real-Time Mesh Deformation", in *Eurographics 2013 - Short Papers*, M.-A. Otaduy and O. Sorkine, Eds., The Eurographics Association, 2013. DOI: 10.2312/conf/EG2013/short/029-032.

[143] Y. Yang, W.-X. Zhang, Y. Liu, L. Liu, and X.-M. Fu, "Error-bounded compatible remeshing", *ACM Trans. Graph.*, vol. 39, no. 4, 2020, ISSN: 0730-0301. DOI: 10.1145/3386569.3392434.

[144] J. Luo, K. Ying, and J. Bai, "Savitzky–golay smoothing and differentiation filter for even number data", *Signal Processing*, vol. 85, no. 7, pp. 1429–1434, 2005, ISSN: 0165-1684. DOI: 10.1016/j.sigpro.2005.02.002.

[145] P. J. Rousseeuw, "Silhouettes: A graphical aid to the interpretation and validation of cluster analysis", *Journal of Computational and Applied Mathematics*, vol. 20, pp. 53–65, 1987, ISSN: 0377-0427. DOI: 10.1016/0377-0427(87)90125-7.

[146] R. C. V. Tyser *et al.*, "Characterization of a common progenitor pool of the epicardium and myocardium", *Science*, vol. 2986, eabb2986, January 2021, ISSN: 0036-8075. DOI: 10.1126/science.abb2986.

[147] F. Pedregosa *et al.*, "Scikit-learn: Machine learning in python", *J. Mach. Learn. Res.*, vol. 12, no. null, 2825–2830, 2011, ISSN: 1532-4435. [Online]. Available: https://dl.acm.org/doi/10.5555/1953048.2078195.

[148] L. Lowe, S. Yamada, and M. Kuehn, "Genetic dissection of nodal function in patterning the mouse embryo", *Development*, vol. 128, pp. 1831–1843, 10 May 2001, ISSN: 1477-9129. DOI: 10.1242/dev.128.10.1831.

[149] J.-F. L. Garrec, J. N. Domínguez, A. Desgrange, K. D. Ivanovitch, E. Raphaël, J. A. Bangham, M. Torres, E. Coen, T. J. Mohun, and S. M. Meilhac, "A predictive model of asymmetric morphogenesis from 3d reconstructions of mouse heart looping dynamics", *eLife*, vol. 6, Nov. 2017, ISSN: 2050-084X. DOI: 10.7554/eLife.28951.

[150] C.-P. Heisenberg and Y. Bellaïche, "Forces in tissue morphogenesis and patterning", *Cell*, vol. 153, no. 5, pp. 948–962, 2013, ISSN: 0092-8674. DOI: https://doi.org/10.1016/j.cell.2013.05.008.

[151] H. Skibbe, Q. Wang, O. Ronneberger, H. Burkhardt, and M. Reisert, "Fast computation of 3d spherical fourier harmonic descriptors-a complete orthonormal basis for a rotational invariant representation of three-dimensional objects", in *2009 IEEE 12th International Conference on Computer Vision Workshops, ICCV Workshops*, IEEE, 2009, pp. 1863–1869. DOI: 10.1109/ICCVW.2009.5457509.

[152] G. Dalmasso, M. Musy, M. Niksic, A. Robert-Moreno, C. Badía-Careaga, J. J. Sanz-Ezquerro, and J. Sharpe, "4d reconstruction of developmental trajectories using spherical harmonics", *bioRxiv*, 2021. DOI: 10.1101/2021.12.16.472948.

[153] A. C. G. de Groot, M. M. Bartelings, M. C. Deruiter, and R. E. Poelmann, "Basics of cardiac development for the understanding of congenital heart malformations", *Pediatric Research*, vol. 57, pp. 169–176, 2 Feb. 2005, ISSN: 0031-3998. DOI: 10.1203/01.PDR.0000148710.69159.61.

[154] V. M. Christoffels *et al.*, "Chamber formation and morphogenesis in the developing mammalian heart", *Developmental Biology*, vol. 223, pp. 266–278, 2 Jul. 2000, ISSN: 00121606. DOI: 10.1006/dbio.2000.9753.

[155] O. H. Ocaña, H. Coskun, C. Minguillón, P. Murawala, E. M. Tanaka, J. Galcerán, R. Muñoz-Chápuli, and M. A. Nieto, "A right-handed signalling pathway drives heart looping in vertebrates", *Nature*, vol. 549, no. 7670, pp. 86–90, 2017. DOI: 10.1038/nature23454.

[156] H. Kidokoro, M. Okabe, and K. Tamura, "Time-lapse analysis reveals local asymmetrical changes in c-looping heart tube", *Developmental dynamics: an official publication of the American Association of Anatomists*, vol. 237, no. 12, pp. 3545–3556, 2008. DOI: 10.1002/dvdy.21662.

[157] D. A. Voronov, P. W. Alford, G. Xu, and L. A. Taber, "The role of mechanical forces in dextral rotation during cardiac looping in the chick embryo", *Developmental biology*, vol. 272, no. 2, pp. 339–350, 2004. DOI: 10.1016/j.ydbio.2004.04.033.

[158] J. Sharpe, "Computer modeling in developmental biology: Growing today, essential tomorrow", *Development*, vol. 144, pp. 4214–4225, 23 Dec. 2017, ISSN: 1477-9129. DOI: 10.1242/dev.151274.

[159] J. Schindelin *et al.*, "Fiji: An open-source platform for biological-image analysis", *Nature Methods*, vol. 9, pp. 676–682, 7 Jul. 2012, ISSN: 1548-7091. DOI: 10.1038/nmeth.2019.

[160] O. Sorkine, "Laplacian Mesh Processing", in *Eurographics 2005 - State of the Art Reports*, Y. Chrysanthou and M. Magnor, Eds., The Eurographics Association, 2005. DOI: 10.2312/egst.20051044.

APPENDIX A: SUPPLEMENTARY FIGURES

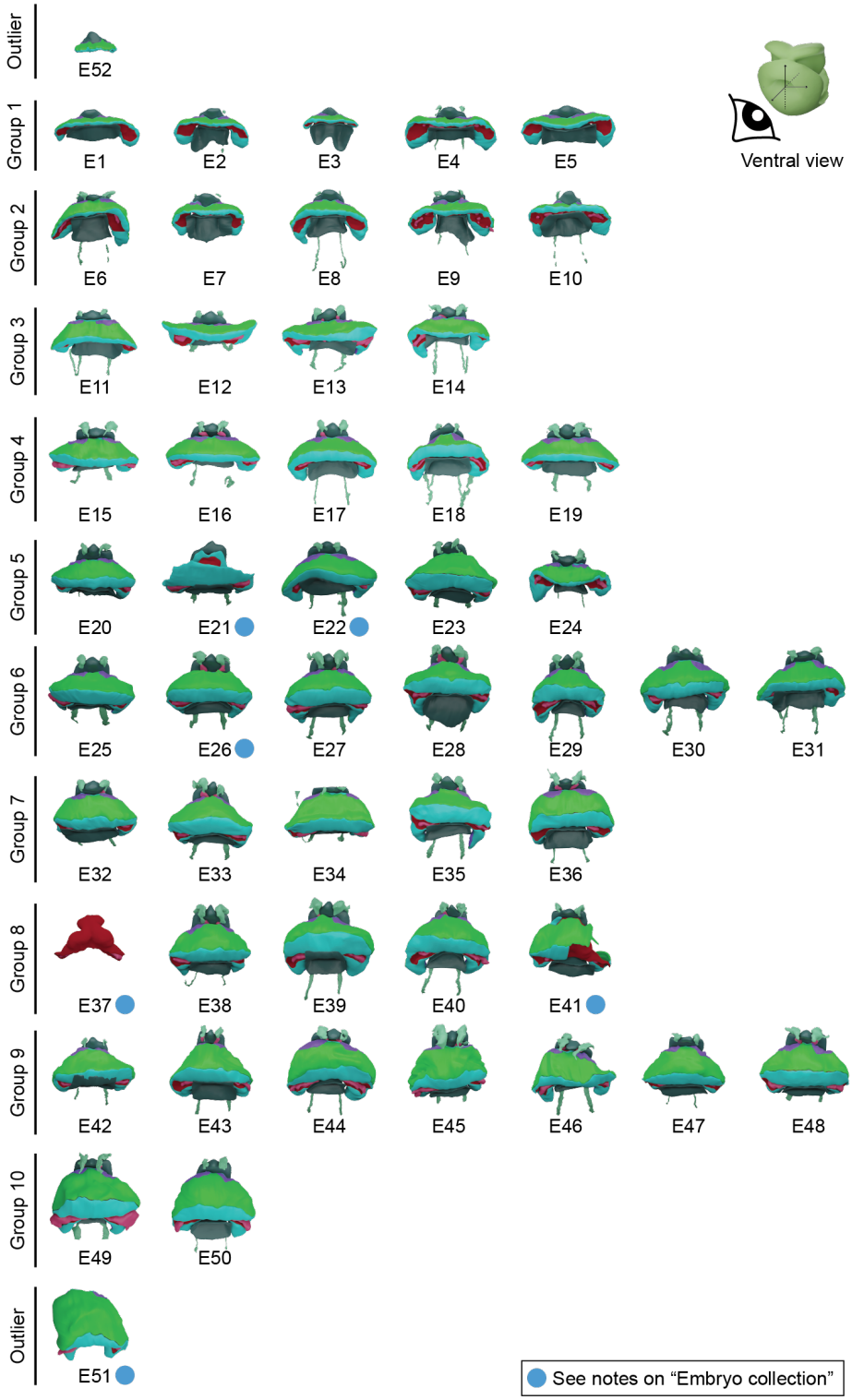

Figure A.1 | **Embryo collection classified by staging groups, showing a ventral view of all tissues.** Ventral view of all the specimens in the collection representing the tissues and shapes described in Figure 4.5. Specimens E51 and E52 are outliers, left out of the stage classification.

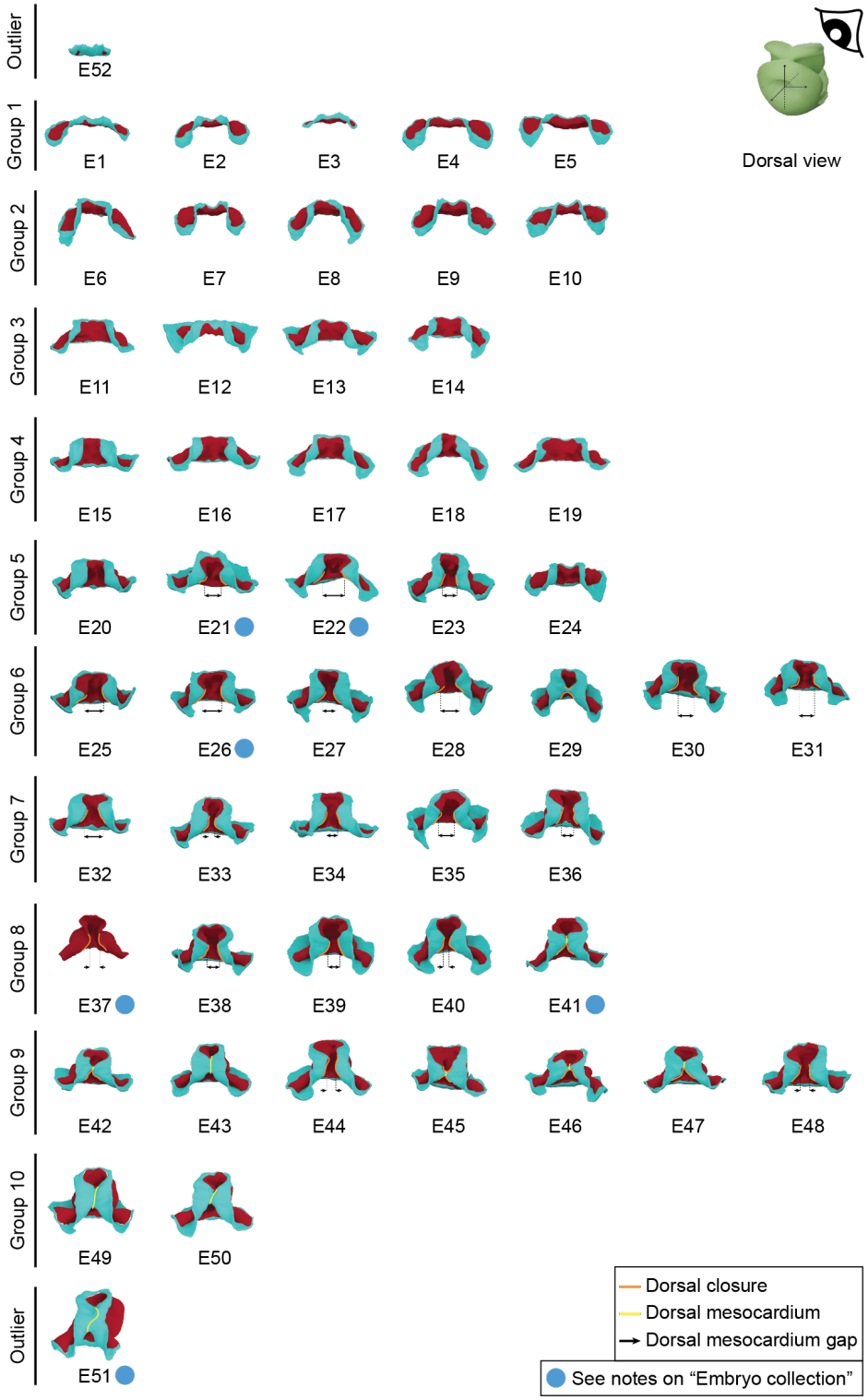

Figure A.2 | **Embryo collection classified by staging groups, showing a dorsal view of SPL and MYO.** Dorsal view of all the specimens in the collection representing the surfaces of the SPL and MYO. Specimens E51 and E52 are outliers, left out of the stage classification.

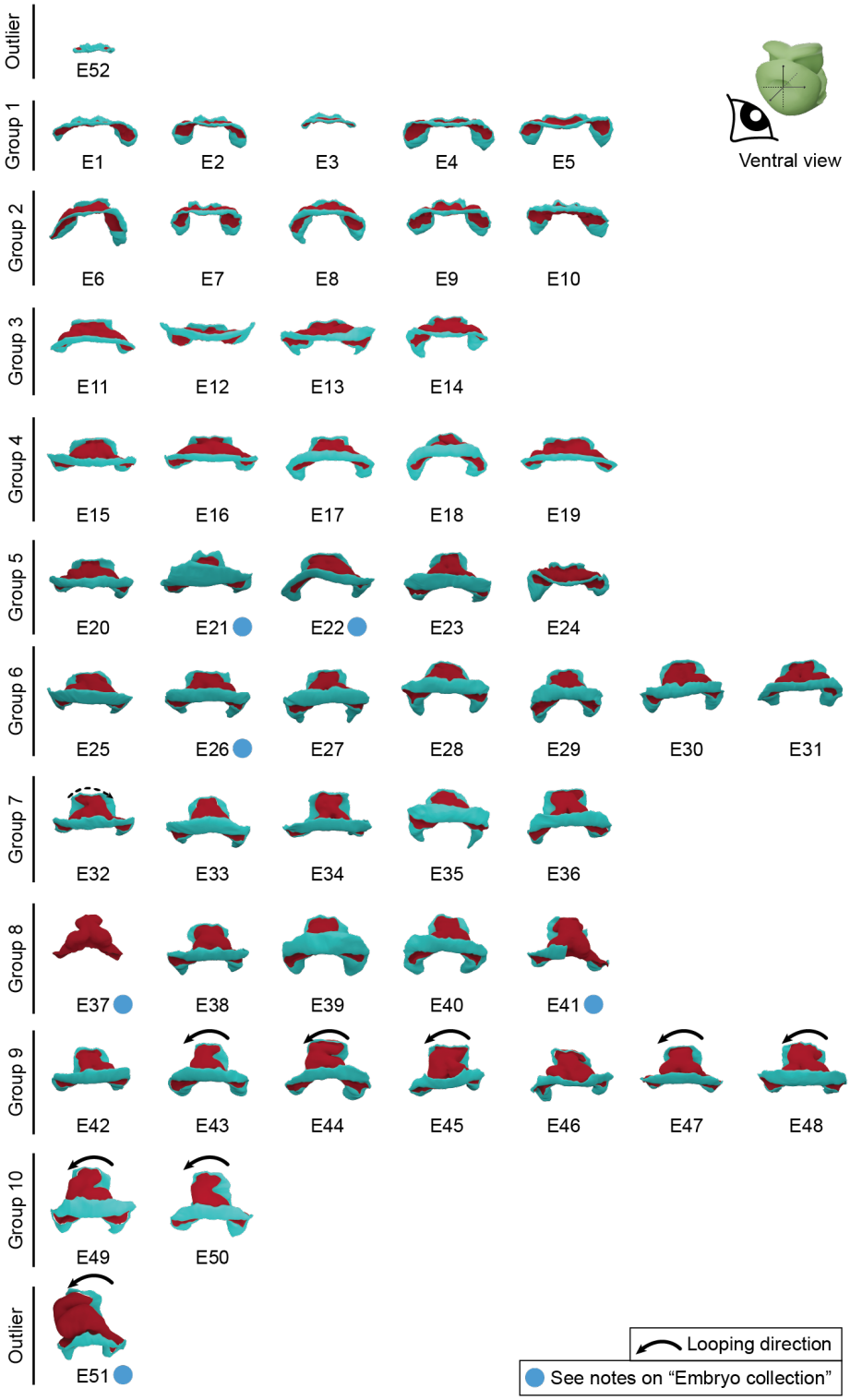

Figure A.3 | **Embryo collection classified by staging groups, showing a ventral view of SPL and MYO.** Ventral view of all the specimens in the collection representing the surfaces of the SPL and MYO. Specimens E51 and E52 are outliers, left out of the 48 stage classification.

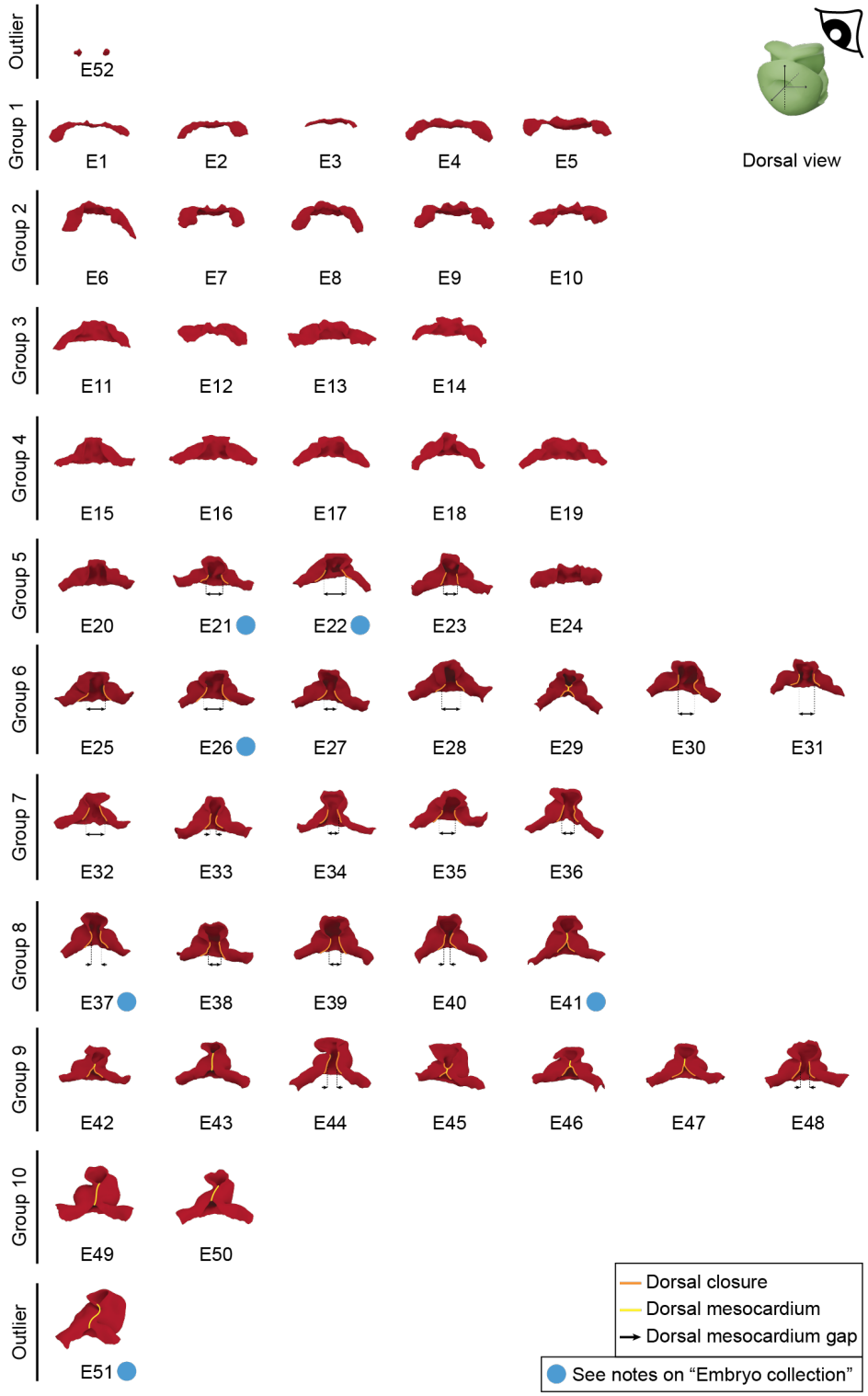

Figure A.4 | **Embryo collection classified by staging groups, showing a dorsal view of the MYO.** Dorsal view of all the specimens in the collection representing the surfaces of the differentiated MYO. Specimens E51 and E52 are outliers, left out of the stage classification.

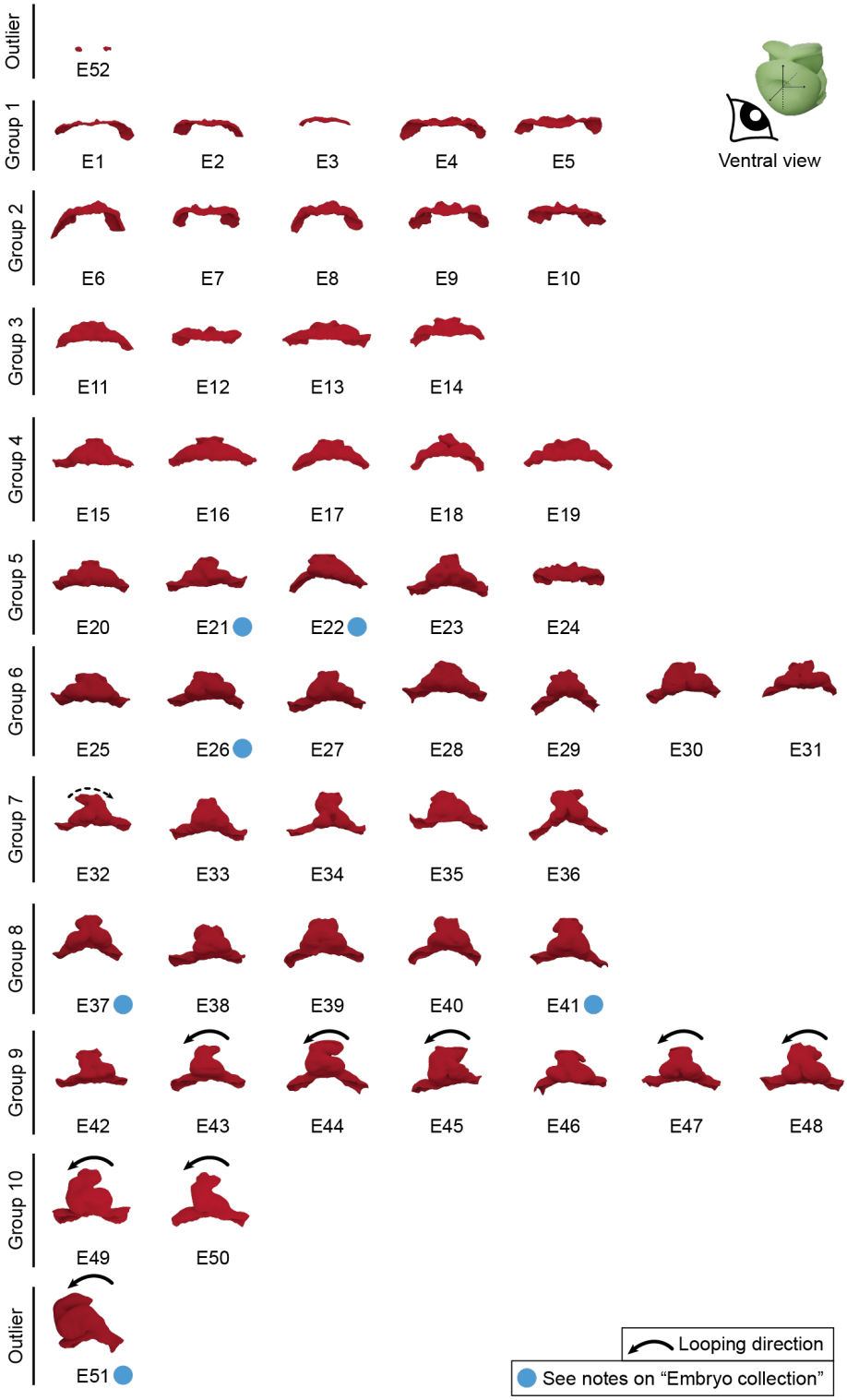

Figure A.5 | **Embryo collection classified by staging groups, showing a ventral view of the MYO.** Ventral view of all the specimens in the collection representing the surfaces of the differentiated MYO. Specimens E51 and E52 are outliers, left out of the stage classification.

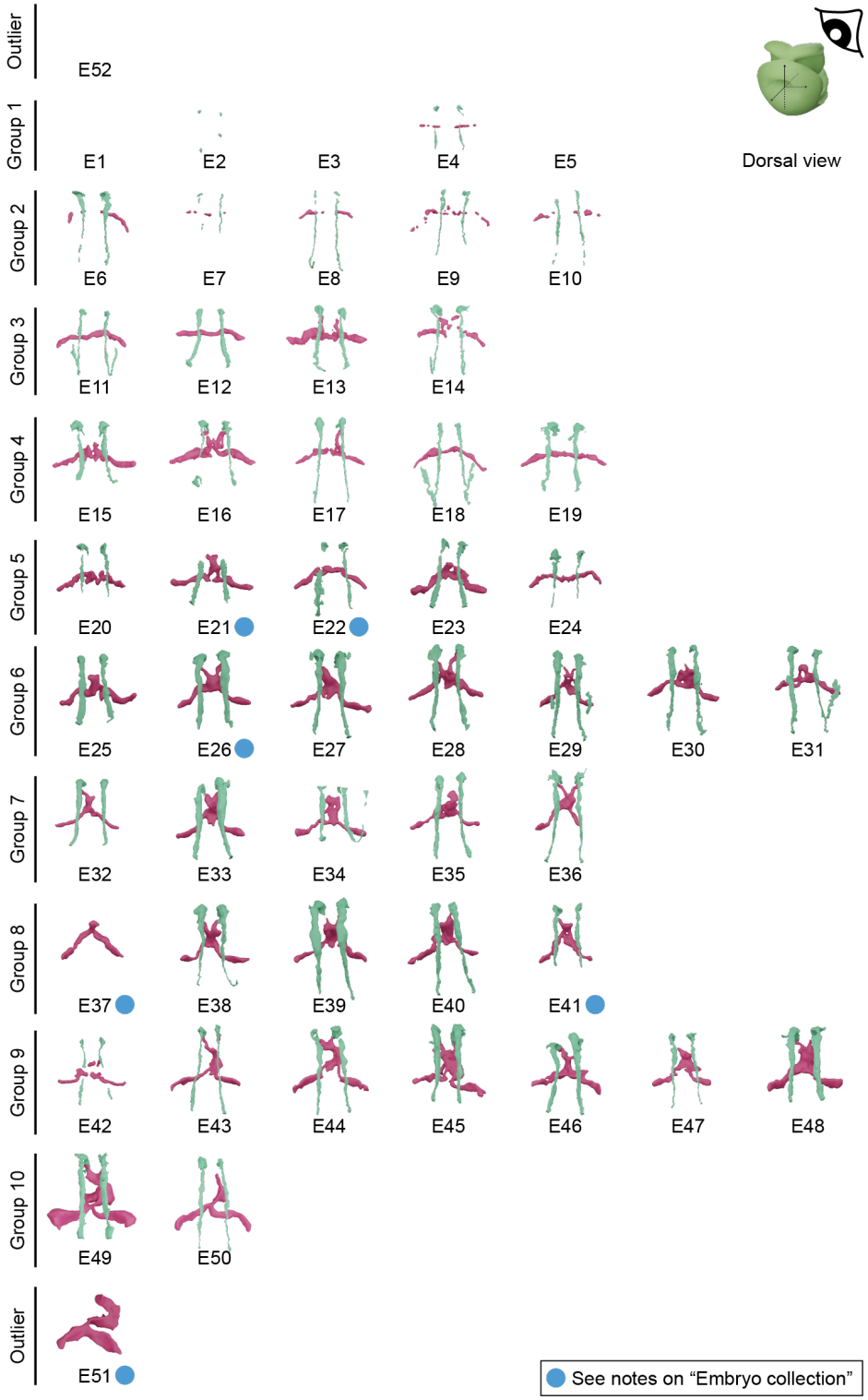

Figure A.6 | **Embryo collection classified by staging groups, showing a dorsal view of the circulatory system.** Dorsal view of all the specimens in the collection representing the surfaces of the circulatory system, split in two parts: endocardial lumen and aortic lumen. Specimens E51 and E52 are outliers, left out of the stage classification.

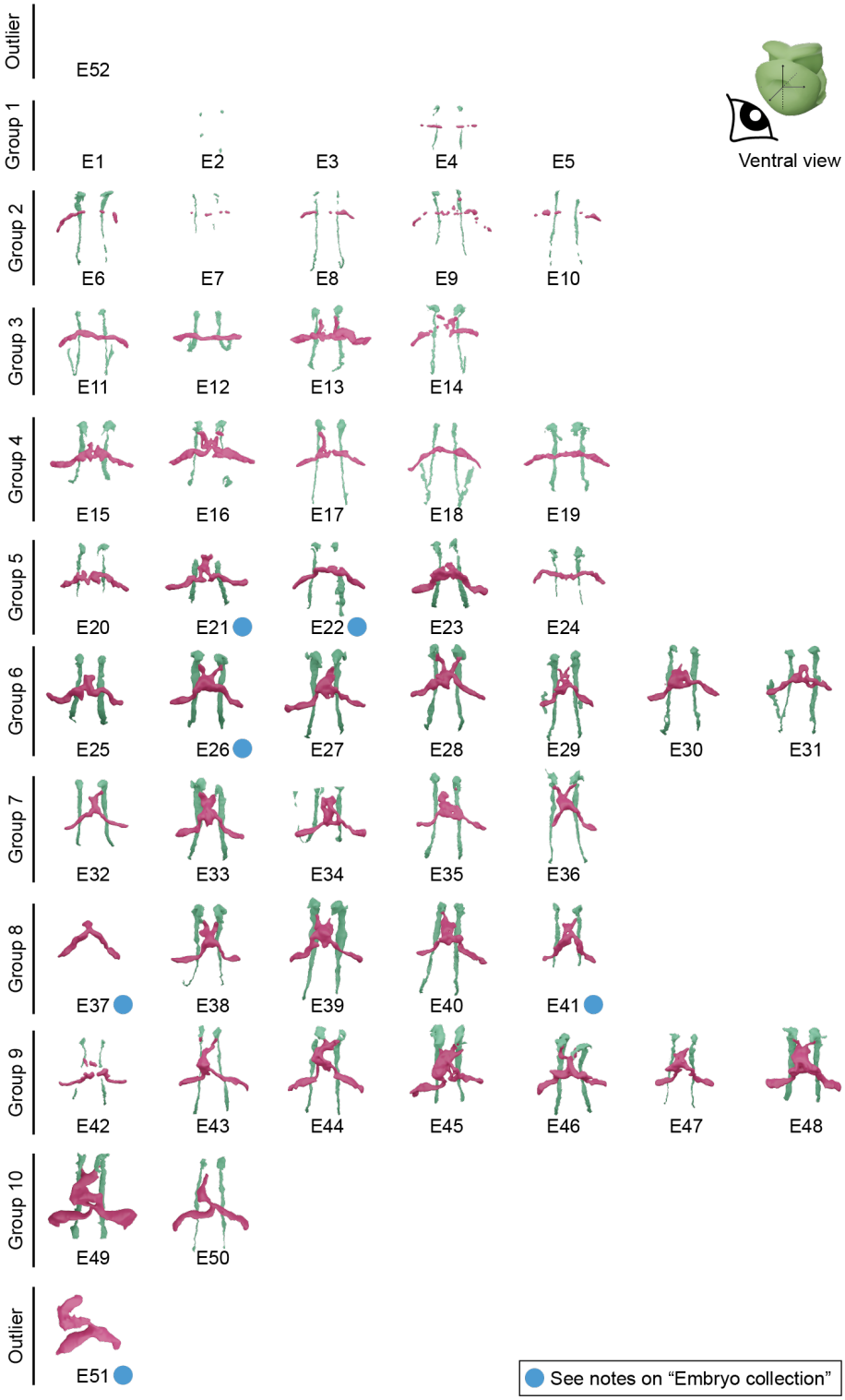

Figure A.7 | **Embryo collection classified by staging groups, showing a ventral view of the circulatory system.** Ventral view of all the specimens in the collection representing the surfaces of the circulatory system, split in two parts: endocardial lumen and aortic lumen. Specimens E51 and E52 are outliers, left out of the stage classification.

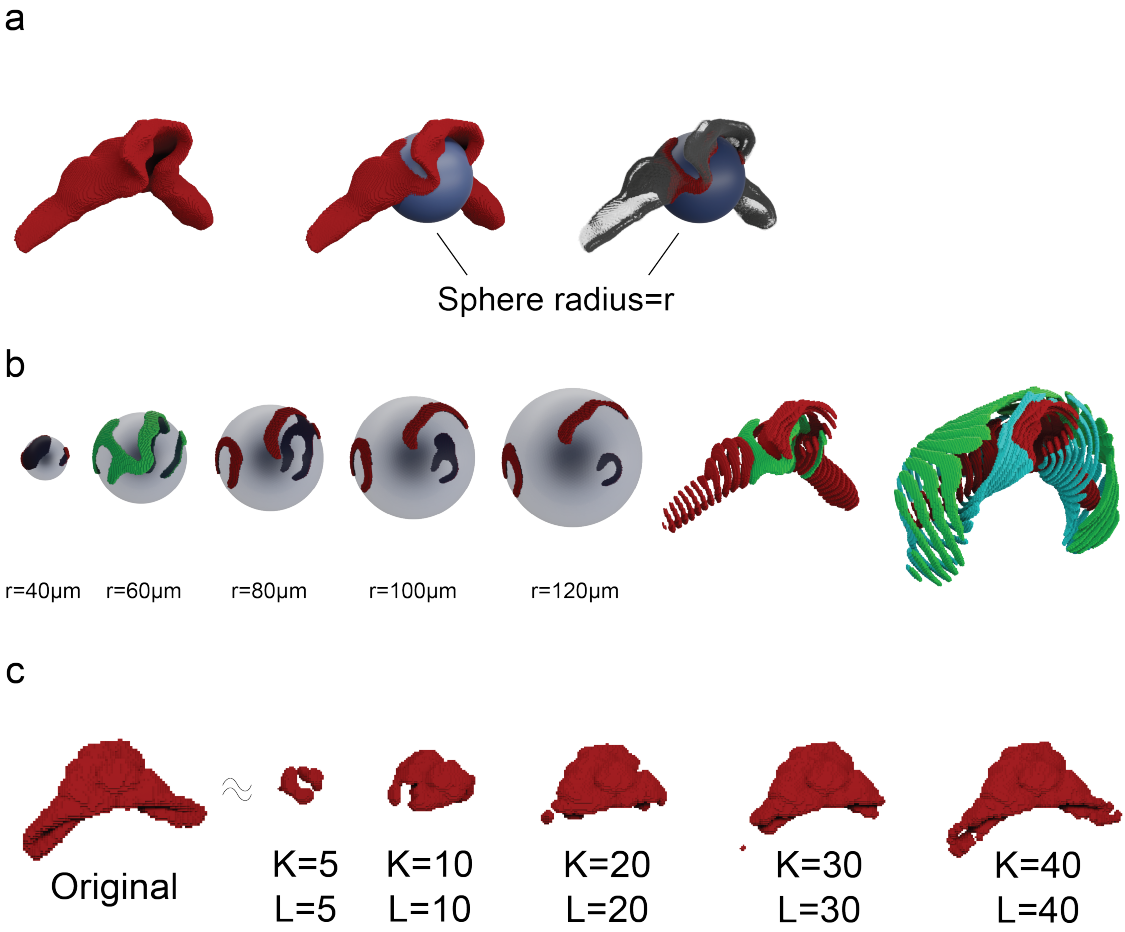

Figure A.8 | **Solid spherical approximation for shape parametric description. a**, Shapes are parametrized using SSH by first defining spheres of varying radius, from $r = 0$ to r equal to the minimum value that contians the shape within the sphere. **b**, Then, the intersection between the spheres of different radius and the shape is calculated. Shapes at the right show a superposition of the sampling of the original shape(s) at different radius. **c**, The shapes, as sampled in **b**, are approaximated by using SSH expansions up to different degree of definition.

APPENDIX B: SOFTWARE AND LIBRARIES

Hereafter, we enumerate and define the usage of every software and/or library that has been utilized in the present thesis.

SURFACEMAPCOMPUTATION This software[1] was used to compute surface maps [103] (section 3.14)

VIEWMAP This software (available in the link as *SurfaceMapComputation*) was used to visualize the surface mapping performed between two shapes, that allows a fine adjustment of the landmarks used (section 3.14)

LEICA LAS X We have used Leica LAS X 3.5.2.18963 to stitch the tile-scans of the images we have acquired in the confocal (subsection 3.3.1)

HUYGENS Huygens Professional version 19.10[2] has been used for image deconvolution (section 3.5)

ITK-SNAP This software [122] has been used to segment all the tissues forming the ACC (subsection 3.6.1) and the EL (subsection 3.6.2), as well as for manual segmentation

IMAGEJ We have used this software [159] for basic image processing operations such as rotations, median filters and image format conversions (section 3.5, section 3.6, subsection 3.6.3)

MASK R-CNN We have used this library [126] to automatically segment the AOL and the FP lumen (subsection 3.6.3)

SCIPY Within this library (version 1.5.3) [128], we have used the package *ndimage* to perform median filter operations on the SIs (subsection 3.6.5). We have also used SciPY to dilate images, as we have done for FGE segmentation (subsection 3.6.4) and for the SIs obtained (subsection 3.6.5)

NIBABEL This library (version 3.1.1) [127] was used to save in NIFTI format (.nii) the detection of the AOL and FGE, thus creating their corresponding SIs (subsection 3.6.3)

PYMCUBES This library[3] (version 0.1.2) has been used to access its implementation of the marching cube algorithm [129], that we have used to generate the meshes of all the SIs (section 3.7)

TRIMESH We have used this library[4] (version 3.9.19) for handling the meshes generated from the segmentation images. More specifically, we used this library to apply mesh smoothing filters (Taubin [130] and Laplace [160]) (section 3.7), and other functionalities to check whether a mesh is defined by a closed surface and to know its topology (section 3.7). We have also this library to perform registration of the point clouds, by using a *Procrustes'* shape analysis (section 3.15

1 https://zenodo.org/record/6390818
2 https://svi.nl/HomePage
3 https://github.com/pmneila/PyMCubes
4 https://github.com/mikedh/trimesh

OPEN3D We have used this library (version 0.7.0) [132] to access its implementation of the *Quadric Error Metric Decimation*, that we have used to set the number of faces of all the meshes to 10.000 (section 3.7)

MESHLAB This software (version 2020.12) [133] was used to visualize the meshes we have generated. It was also used for different step of the mid-surface extraction (section 3.10)

MANIFOLD APPROXIMATION OF 3D MEDIAL AXIS This software[5] has been used to extract the skeleton of the meshes, which is one of the steps needed to compute the mid-surfaces (section 3.10)

POINT-CLOUD-UTILS This library[6] was used because it contains an implementation of the Poisson disc sampling algorithm, needed for the mid-surface computations (section 3.10)

BALL PIVOTING ALGORITHM We used this algorithm [137] for point cloud reconstruction purposes, as a part of the mid-surface calculation workflow (section 3.10)

5 http://www2.riken.jp/brict/Yoshizawa/Research/Skeleton.html
6 https://github.com/fwilliams/point-cloud-utils

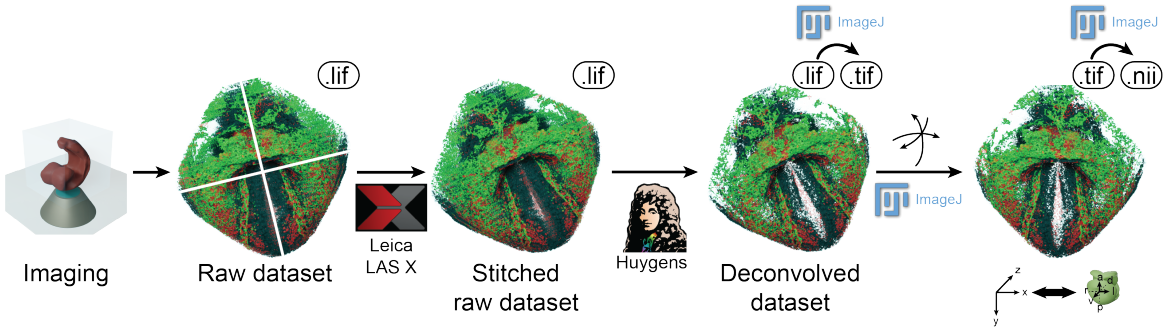

Figure B.1 | **Image processing steps.** The figure shows all the steps taken to prepare the embryo datasets for segmentation and further analysis. The format of every file is specified within each of ronded-corner black box. The software used for every step is speficied under every directional arrow.

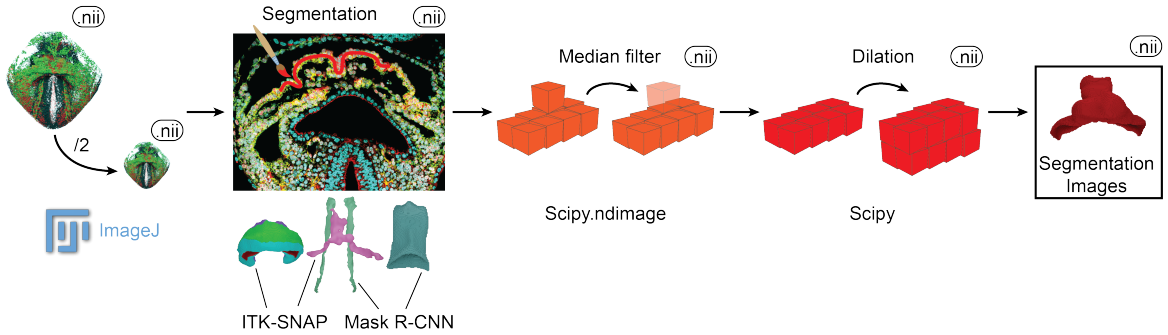

Figure B.2 | **Processing steps before and after segmentation.** The figure shows all the steps taken to process the embryo's dataset before and after segmentation. The format of every file is specified within each of ronded-corner black box. The software used for every step is speficied.

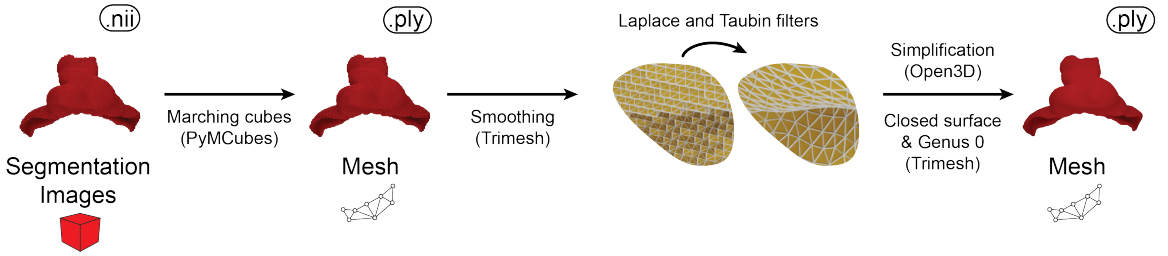

Figure B.3 | **Processing steps for the mesh representation of the segmented tissues and structures.** The figure shows all the steps taken to transform the segmentation images in meshes, the smoothing process and final preparation steps. The format of every file is specified within each of ronded-corner black box. The software used for every step is speficied for every step under the directional arrows, within parenthesis.

PUBLICATIONS

The list of publication in which, as author of this thesis, I have contributed so far up to the day of thesis defense are:

- **I. Esteban**, P. Schmidt, A. Desgrange, M. Raiola, S. Temiño, S. M. Meilhac, L. Kobbelt, and M. Torres, "Pseudodynamic analysis of heart tube formation in the mouse reveals strong regional variability and early left–right asymmetry", Nature Cardiovascular Research, vol. 1, pp. 504–517, 5 May 2022, ISSN: 2731-0590. DOI: 10.1038/s44161-022-00065-1.
- **I. Esteban** and M. Torres, "A quantitative and temporal 3d atlas of embryonic mouse heart formation", Nature Cardiovascular Research, May 2022, ISSN: 2731-0590. DOI: 10.1038/s44161-022-00078-w.
- K. Ivanovitch, **I. Esteban**, and M. Torres, "Growth and morphogenesis during early heart development in amniotes", Journal of Cardiovascular Development and Disease, vol. 4, p. 20, 4 2017, ISSN: 2308-3425. DOI: 10.3390/jcdd4040020.

ACKNOWLEDGMENTS

En primer lugar, quiero agradecer especialmente a Miguel Torres la oportunidad que me ha dado en su grupo y en la ciencia, por todo su esfuerzo en sacar este proyecto adelante, por su paciencia, y por estar siempre ahí. Quiero incluir en este agradecimiento a Andrés Santos, por haberme mostrado su apoyo desde el principio y haberme ayudado en tantos momentos durante la tesis.

Mis agradecimientos van también dedicados al personal de la Unidad de Microscopía del CNIC. Especialmente a Valeria, Verónica, Elvira, Moreno y Helio. Vuestra ayuda y apoyo han sido fundamentales para mí. Al personal del Animalario también, gracias.

Muchas gracias también a todas las personas del grupo MT (los que están y los que ya no) y demás personas del CNIC. Me habéis enseñado, apoyado, hecho reír y acompañado durante mucho tiempo. Quiero mencionar especialmente a Patrick Schmidt, por todas las horas que hemos trabajando juntos, por todo su esfuerzo incansable y extraordinario, y sobre todo por su confianza en esta colaboración. Danke sehr.

Aunque sea en último lugar, pero sin duda representa mi sustento principal, quiero agradecer a todas las personas que, desde fuera de la ciencia, me han mostrado su apoyo incondicional y compañía durante estos años.